

Journal Pre-proofs

1 + 1 > 2: A critical review of MOF/bismuth-based semiconductor composites for boosted photocatalysis

Chen Zhao, Xi Pan, Zhihua Wang, Chong-Chen Wang

PII: S1385-8947(20)34140-1
DOI: <https://doi.org/10.1016/j.cej.2020.128022>
Reference: CEJ 128022

To appear in: *Chemical Engineering Journal*

Received Date: 19 August 2020
Revised Date: 27 November 2020
Accepted Date: 3 December 2020



Please cite this article as: C. Zhao, X. Pan, Z. Wang, C-C. Wang, 1 + 1 > 2: A critical review of MOF/bismuth-based semiconductor composites for boosted photocatalysis, *Chemical Engineering Journal* (2020), doi: <https://doi.org/10.1016/j.cej.2020.128022>

This is a PDF file of an article that has undergone enhancements after acceptance, such as the addition of a cover page and metadata, and formatting for readability, but it is not yet the definitive version of record. This version will undergo additional copyediting, typesetting and review before it is published in its final form, but we are providing this version to give early visibility of the article. Please note that, during the production process, errors may be discovered which could affect the content, and all legal disclaimers that apply to the journal pertain.

1 + 1 > 2: A critical review of MOF/bismuth-based semiconductor composites for boosted photocatalysis

Chen Zhao^{1,2}, Xi Pan¹, Zhihua Wang^{2*}, Chong-Chen Wang^{1*}

¹ Beijing Key Laboratory of Functional Materials for Building Structure and Environment Remediation, Beijing University of Civil Engineering and Architecture, Beijing, 100044, China

² State Key Laboratory of Chemical Resource Engineering, Beijing University of Chemical Technology, Beijing 100029, China

Abstract: Photocatalysis is an effective procedure for environmental remediation and energy production. Considering that both the bismuth-based semiconductors and metal-organic frameworks (MOFs) are star photocatalysts, the combination of bismuth-based semiconductors with MOFs is beneficial to overcome their shortcomings like narrow sunlight absorption range, deficient active sites and rapid charges recombination rate. Recently, these composites displayed outstanding photocatalytic performances toward nitric oxide (NO) oxidation, Cr(VI) reduction, oxygen production, nitrogen (N₂) fixation and organic pollutants degradation. In this review, we focused to discuss the fabrication and synthesis methods, characterizations, photocatalytic applications as well as the corresponding mechanisms of some representative MOF/bismuth-based semiconductor composites (abbreviated as MBCs). Finally, new insights are proposed to meet the future challenges and development of the composites, which can provide better knowledge for the advancement of the related research areas.

Keywords: photocatalysis, metal-organic frameworks, bismuth-based semiconductors, composite, environmental remediation.

1. Introduction

*Corresponding author:

E-mail address: zhwang@mail.buct.edu.cn (Zhihua Wang), chongchenwang@126.com/wangchongchen@bucea.edu.cn (Chong-Chen Wang).

Heterogeneous photocatalysis is a well-known type of green technology, which has been depicted as a broad spectrum of applications in selective organic transformation, environmental remediation and water splitting at ambient conditions [1-5]. The role of photocatalysis is becoming more important with the growing concerns on environmental problems and reliable energy production. Fujishima and co-workers [6] have conducted innovative and extensive investigations on the process of producing chemical energy from light energy with the aid of photocatalysts. Since then, some typical inorganic photocatalysts with multi-functional aptitudes have been reported by scientific researchers, such as TiO_2 [7, 8], ZnO [9, 10], CdS [11-13] and $\alpha\text{-Fe}_2\text{O}_3$ [14, 15]. However, the actual applications of the above photocatalysts were severely limited because of the rapid recombination of electron-hole pairs and poor chemical functionality.

Metal-organic frameworks (MOFs), porous crystalline hybrid materials consisting of metal ions as templates and organic ligands as linkers, have become hotspots in various fields in the last two decades [16-18]. MOFs take the advantages of the useful characteristics of both organic ligands and metal ions, which often offer exceptional properties that surpass the expectations for a mixture made from different constituents [19, 20]. Owing to the well-ordered highly porous structures, large surface areas and tunable organic ligands or metal ions, MOFs have drawn great interest in gas storage and separation [21-23], molecular adsorption [24, 25], drug delivery [26, 27], chemical sensors [28, 29] and catalysis [30-32]. Amongst catalysis, it is considered that using MOFs for photocatalysis demonstrates a very promise future in the coming time, which is primarily based on the facts: (1) As a type of porous materials, MOFs possess many chemical advantages besides the above-mentioned physical merits, including the presence of unsaturated metal centers, open metal sites and even typical functionalized organic ligands that are catalytically active [33, 34]; (2) Some MOFs like UiO-66 (UiO is the abbreviation of University of Oslo), NTU-9 (NTU is the abbreviation of Nanyang Technological University) and MOF-5 (MOF is the abbreviation of metal-organic framework) have the properties like semiconductors, which could be employed as charge carrier systems via the photoexcitation of metal clusters or organic ligands [35]; (3) Contrary to the conventional semiconductors, it is amazing that the functionalities and structures of the MOFs can easily be adapted to the desired ones via the modification of their metal centers or organic ligands. These unique properties of MOFs provide the exciting possibility to control both the physical and

chemical properties of MOFs at the molecular level [36, 37]; (4) MOFs with distinct crystalline structures can be used for the characterization and estimation of their structure-property relationships [31, 38]. However, generally, MOFs as photocatalysts with wide bandgaps are inclined to be excited by UV light, which hinder their applications under sunlight or visible light (Figure 1(a)). Also, some problems such as rapid recombination of electron-hole pairs, inadequate stability and poor conductivity lead to poor practicality and low photocatalytic efficiency. Considering that the abundance of MOFs structures and band-edge positions, constructing MOFs-based composites with narrow gap semiconductors should be an ideal strategy for overcoming the above drawbacks and inheriting the advantages of the individual component. For instance, our research group has fabricated several types of MOFs-based composites like $\text{NH}_2\text{-UiO-66/S-TiO}_2$ [39], $\text{MIL-53(Fe)/Bi}_{12}\text{O}_{17}\text{Cl}_2$ (MIL is the abbreviation of Material of Institute Lavoisier) [40], $\text{MIL-88A(Fe)/polyaniline (PANI)}$ [41], $\text{BUC-21/Cd}_{0.5}\text{Zn}_{0.5}\text{S}$ (BUC is the abbreviation of Beijing University of Civil Engineering and Architecture) [42], $\text{BUC-21/N-K}_2\text{Ti}_4\text{O}_9$ [43], $\text{BUC-21/Bi}_{24}\text{O}_{31}\text{Br}_{10}$ [44], $\text{BUC-21/titanate nanotube}$ [45], $\text{BUC-21/g-C}_3\text{N}_4$ [46], $\text{Ag/Ag}_3\text{PO}_4/\text{NH}_2\text{-MIL-125}$ [47], MIL-100(Fe)/PANI [48], $\text{NH}_2\text{-UiO-66/Ag}_2\text{CO}_3$ [49], $\text{UiO-66/g-C}_3\text{N}_4$ [50], $\text{MIL-100(Fe)/g-C}_3\text{N}_4$ [51], MIL-100(Fe)/WO_3 [52], etc. These composites exhibited superior photocatalytic activities to those of pristine MOFs and another photocatalysts.

Recently, several reviews focusing on MOFs-based composites as photocatalysts were reported. For example, our research group summarized the fabrication and synthesis methods, characterizations, photocatalytic applications as well as the corresponding mechanisms of MOFs/ $\text{g-C}_3\text{N}_4$ [37] and MOFs/ TiO_2 composites [53]. Zeng's group [19, 54] provided two reviews in 2019 and 2020, respectively, which demonstrated metal or metal-containing nanoparticle@MOF composites (M/MC NP@MOF) and quantum dots (QDs)-MOFs composites can be applied in various photocatalytic reactions, including hydrogen generation, Cr(VI) reduction, NO oxidation, organic dye degradation and production of methane (CH_4) from CO_2 reduction. According to our literature search, however, review outlining for the heterogenous photocatalysis of the MOF/bismuth-based semiconductor composites (MBCs) and their corresponding mechanisms has not been reported.

At present, bismuth-based semiconductors have received much attention due to their visible-

light-responsive properties, chemical inertness, non-toxicity and excessive availability [55, 56]. The valence bands of bismuth-based semiconductors comprise of hybrid orbitals of Bi 6s and O 2p. The well-dispersed Bi 6s orbital results in shrinking the bandgap and enhanced the transport of photo-generated charge carriers [57-59]. It is observed that bismuth-based semiconductors generally possess bandgaps around 3.0 eV. Therefore, almost all of bismuth-based semiconductors have been synthesized and used as visible-light-responsive photocatalysts like Bi_2O_3 [60, 61], Bi_2S_3 [62, 63], Bi_2MO_6 (M = W or Mo) [64, 65], BiVO_4 [66], BiOX (X = Halogens) [67, 68], $\text{Bi}_x\text{O}_y\text{X}_z$ (X = Halogens) [69], BiPO_4 [70, 71], $(\text{BiO})_2\text{CO}_3$ [72], BiFeO_3 [73] and other Bi^{5+} -containing compounds [74, 75]. As shown in Figure 1(b), it can be found that the band positions of most bismuth-based semiconductors are suitable for photocatalytic applications, including removal of toxins from air and water as well as the fuel production. However, one of the most demanding challenges is the rapid recombination of photo-generated electron-hole pairs during the photocatalytic process. This issue could be improved through component adjustment [76, 77], morphology control [78, 79] and heterojunction construction [80, 81]. Up to now, many functional materials have been used to combine with bismuth-based semiconductors for fabricating binary heterojunction photocatalysts, such as Au nanoparticles [82-84], TiO_2 [85-87], g- C_3N_4 [88, 89], graphene oxide (GO) [90, 91]. Although the above composites exhibit improved photocatalytic performances than the pristine photocatalyst due to the synergistic effect of materials, their applications are limited by various aspects. For example, the Au nanoparticles can act as a photo-generated electrons' reservoir to accelerate the migration of charge carriers and broaden the light absorption range via surface plasmon resonance (SPR) effect [82-84]. However, the introduction of heteroatoms may change the space lattice and induce additional stress of bismuth-based photocatalysts. As to TiO_2 , the existing bismuth-based semiconductors mainly play roles in strengthening the visible light utilization of TiO_2 and suppressing the phase transformation between anatase and rutile. This means that TiO_2 usually acts as the primary photocatalyst, bismuth-based semiconductors play the role of co-catalysts. Lamellar exfoliation g- C_3N_4 have proved to be expected to enhance the photocatalytic performances of bismuth-based semiconductors via surface modifications [55, 92]. But its low surface area and poor hydrophilicity seriously affect the adsorption-photocatalytic process for target pollutant removal in aquatic environment. With respect to GO, it typically plays the electron trapping role in the

corresponding bismuth-based composites [90, 91]. Therein, MOFs with large surface area and porous structure will offer a platform for dispersing and immobilizing bismuth-based semiconductors. Moreover, combining MOFs and bismuth-based photocatalysts for composites construction can significantly boost the corresponding photocatalytic performance by increasing the active sites, broadening the light spectrum to visible light or UV-visible light regions and inhibiting the recombination of photo-generated charge carriers.

Herein, this review mainly focuses on the high-level advancement of the MBCs applying in the field of photocatalysis, covering some representative MOFs, including HKUST-1 (HKUST is the abbreviation of Hong Kong University of Science and Technology), MIL-100(Fe), MIL-88(Fe), MIL-53(Fe), MIL-125, NH₂-MIL-125, UiO-66, NH₂-UiO-66, ZIF-8 (ZIF is the abbreviation of zeolitic imidazolate framework) and some bismuth-based materials, such as Bi₂O₃, Bi₂S₃, Bi₂WO₆, Bi₂MoO₆, BiVO₄, BiOX. Furthermore, their fabrication approaches, applications and the corresponding mechanism were analyzed detailly. Finally, the current challenges and problems concerning to the present MBCs are highlighted and the perspectives are suggested.

Figure 1. Band positions of some common (a) MOFs and (b) bismuth-based photocatalysts and the relevant reaction potentials at pH = 7 [44, 50, 51, 93-124].

2. The current status of MBCs

Recently, MBCs are regarded as a sort of potential photocatalysts and have attracted rapidly increasing attention. As shown in Figure 2(a), various studies on applications of MBCs in the field of photocatalysis were reported during the past seven years. Furthermore, the number of publications is increasing yearly, indicating that the combination of MOFs and bismuth-based semiconductors has successfully achieved the goal of enhancing photocatalytic performance. As for application areas of MBCs, 91.5% of published papers verified the applicability of MBCs for photocatalytic degradation of organic pollutants and Cr(VI) reduction. Table 1 summarized the existing binary, ternary and even quaternary MBCs. More importantly, some representative MBCs were selected in this section to highlight their preparation methods, characterizations, applications and mechanisms.

Figure 2. (a) Number of publications of MBC photocatalysts during the past six years and (b) doughnut chart of photocatalytic applications of MBCs (source: web of science, date: 6th November 2020, key words: MOFs, bismuth and photocatalysis).

Table 1. Summary of the preparation methods and photocatalytic applications of MBCs.

No.	Composite photocatalysts	Preparation method	Applications	Ref.
1	ZIF-8/Bi ₄ O ₅ Br ₂	Prepared ZIF-8 was incorporated with Bi ₄ O ₅ Br ₂ from its precursors via in-situ deposition.	Conversion of nitrogen (N ₂) to ammonia (NH ₃)	[125]
2	ZIF-8/Bi ₂ S ₃	Prepared Bi ₂ S ₃ was incorporated with ZIF-8 from its precursors via in-situ deposition.	Rhodamine B (RhB) degradation	[126]
3	ZIF-8/BiVO ₄	Prepared BiVO ₄ was incorporated with ZIF-8 from its precursors via in-situ deposition.	Methylene blue (MB) degradation	[127]
4	ZIF-8/Bi ₂ MoO ₆	Prepared Bi ₂ MoO ₆ was incorporated with ZIF-8 from its precursors via in-situ deposition.	MB degradation	[128]
5	UiO-66/BiVO ₄	Incorporation of BiVO ₄ from its precursors on the surface of as-prepared UiO-66 via hydrothermal synthesis.	RhB degradation	[129]
6	UiO-66/Bi ₂ MoO ₆	Incorporation of Bi ₂ MoO ₆ from its precursors on the surface of as-prepared UiO-66 via hydrothermal synthesis.	RhB degradation	[130]
7	UiO-66/Bi ₂ WO ₆	Solvothermal treatment of the mixture containing the as-prepared UiO-66 and the precursors of Bi ₂ WO ₆ .	RhB degradation	[131]

8	UiO-66/BiOBr	Mixing the solutions of prepared UiO-66 and the precursors of BiOBr and vigorous stirring at room temperature.	Atrazine degradation	[132]
9	UiO-66/BiOBr	Mixing the solutions of prepared UiO-66 and the precursors of BiOBr and vigorous stirring at room temperature.	RhB degradation	[133]
10	UiO-66/BiOI	Incorporation of BiOI from its precursors on the surface of as-prepared UiO-66 via hydrothermal treatment.	Salicylic acid	[134]
11	UiO-66/BiOCl	Incorporation of BiOCl from its precursors on the surface of as-prepared UiO-66 via hydrothermal treatment.	RhB degradation	[135]
12	NH ₂ -UiO-66/BiOBr	Incorporation of BiOBr from its precursors on the prepared NH ₂ -UiO-66 via solvothermal deposition.	Norfloxacin (NOR) degradation	[136]
13	NH ₂ -UiO-66/BiOBr	Incorporation of BiOBr from its precursors on the prepared NH ₂ -UiO-66 via solvothermal deposition.	Tetracycline (TC) degradation and Cr(VI) reduction	[137]
14	NH ₂ -UiO-66/BiOBr	Incorporation of BiOBr from its precursors on the surface of as-prepared NH ₂ -UiO-66 via hydrothermal treatment.	RhB degradation	[138]
15	NH ₂ -UiO-66/Bi ₂ WO ₆	Incorporation of Bi ₂ WO ₆ from its precursors on the prepared NH ₂ -UiO-66 via solvothermal deposition.	NO oxidation	[139]

16	NH ₂ -UiO-66/Bi ₂ WO ₆	Incorporation of Bi ₂ WO ₆ from its precursors on the prepared NH ₂ -UiO-66 via hydrothermal treatment.	RhB and TC degradation	[140]
17	BiOI/NH ₂ -UiO-66/g-C ₃ N ₄	Preparation of NH ₂ -UiO-66/g-C ₃ N ₄ from NH ₂ -UiO-66 and g-C ₃ N ₄ deposition, followed by incorporation of BiOI from its precursors on the surface of as-prepared NH ₂ -UiO-66/g-C ₃ N ₄ via in-situ deposition.	TC and RhB degradation	[119]
18	MIL-125/BiVO ₄	Prepared MIL-125 was incorporated with BiVO ₄ from its precursors via hydrothermal deposition.	RhB degradation	[141]
19	MIL-125/BiVO ₄	Prepared MIL-125 was incorporated with BiVO ₄ from its precursors via hydrothermal treatment.	Comparison of interfacial charge transfer rate among the as-prepared composites	[142]
20	MIL-125/BiOI	The as-prepared MIL-125 and BiOI were sonicated for 30 min, then the obtained solution was treated by the hydrothermal process.	TC degradation	[143]
21	NH ₂ -MIL-125/Bi ₂ MoO ₆	Prepared NH ₂ -MIL-125 was incorporated with Bi ₂ MoO ₆ from its precursors via solvothermal treatment.	Dichlorophen/trichlorophenol degradation and O ₂ production	[144]
22	NH ₂ -MIL-125/Bi ₂ WO ₆	Prepared NH ₂ -MIL-125 was incorporated with Bi ₂ WO ₆ from its precursors via hydrothermal deposition.	TC and RhB degradation	[145]

23	NH ₂ -MIL-125/Bi ₂ WO ₆	Prepared NH ₂ -MIL-125 was incorporated with Bi ₂ WO ₆ from its precursors via hydrothermal deposition.	TC degradation	[146]
24	NH ₂ -MIL-125/Bi ₂ S ₃	Prepared Bi ₂ S ₃ was incorporated with NH ₂ -MIL-125 from its precursors via solvothermal treatment.	RhB degradation and Cr(VI) reduction	[147]
25	NH ₂ -MIL-125/BiOBr	Prepared NH ₂ -MIL-125 was incorporated with BiOBr from its precursors via hydrothermal treatment.	RhB degradation	[148]
26	NH ₂ -MIL-125/BiOCl	Prepared NH ₂ -MIL-125 was incorporated with BiOCl from its precursors via solvothermal deposition.	Bisphenol A (BPA) and TC degradation	[149]
27	NH ₂ -MIL-125/BiOI	Prepared NH ₂ -MIL-125 was incorporated with BiOI from its precursors via hydrothermal treatment.	Methyl orange (MO) degradation	[150]
28	MIL-53(Fe)/Bi ₁₂ O ₁₇ Cl ₂	Ball-milling treatment of the as-prepared MIL-53(Fe) and Bi ₁₂ O ₁₇ Cl ₂ mixture.	Cr(VI) reduction	[40]
29	MIL-53(Fe)/BiOBr	Prepared MIL-53(Fe) was incorporated with BiOBr from its precursors via hydrothermal treatment.	Carbamazepine (CBZ) and RhB degradation	[151]
30	MIL-53(Fe)/BiOCl	Prepared MIL-53(Fe) was incorporated with BiOCl from its precursors via hydrothermal deposition.	Photodegradation of RhB assisted by persulfate (PS)	[152]

31	MIL-53(Fe)/Bi ₅ O ₇ I	Prepared MIL-53(Fe) was incorporated with Bi ₅ O ₇ I from its precursors via hydrothermal treatment.	RhB degradation	[153]
32	MIL-53(Fe)/Bi _{3.43} Fe _{0.57} O ₆	Prepared MIL-53(Fe) was incorporated with Bi _{3.43} Fe _{0.57} O ₆ from its precursors via etching and re-growth method.	Selective oxidation of aromatic alcohols	[154]
33	MIL-53(Fe)/Bi ₂ WO ₆	Prepared MIL-53(Fe) was incorporated with Bi ₂ WO ₆ from its precursors via hydrothermal deposition.	RhB and phenol degradation	[155]
34	MIL-53(Fe)/ α -Bi ₂ O ₃ /g-C ₃ N ₄	The α -Bi ₂ O ₃ /g-C ₃ N ₄ binary composite was firstly prepared, then the suspension containing the prepared α -Bi ₂ O ₃ /g-C ₃ N ₄ and MIL-53(Fe) was stirred constantly under 60 °C.	Amino black 10B degradation	[156]
35	MIL-88A(Fe)/BiOI	Prepared MIL-88A(Fe) was incorporated with BiOI from its precursors via solvothermal deposition.	Acid blue 92 (AB92) and MB degradation	[157]
36	BiOI/MIL-88A(Fe)/g-C ₃ N ₄	Preparation of MIL-88A(Fe)/g-C ₃ N ₄ from MIL-88A(Fe) and g-C ₃ N ₄ deposition, followed by incorporation of BiOI from its precursors on the surface of as-prepared MIL-88A(Fe)/g-C ₃ N ₄ via in-situ deposition.	AB92, RhB and phenol degradation	[158]
37	MIL-88B(Fe)/Bi ₂ MoO ₆ with oxygen vacancies (OVs)	Solvothermal synthesis of Bi ₂ MoO ₆ with OV from its precursors by adding tetramethylethylenediamine	BPA and TC degradation	[123]

		(TMEDA), followed by the incorporation of Bi_2MoO_6 with OV's on the MIL-88B(Fe) from its precursors.		
38	MIL-88B(Fe)/BiOI	Prepared MIL-88B(Fe) was incorporated with BiOI from its precursors via solvothermal deposition.	Ciprofloxacin (CIP), phenol and RhB degradation	[159]
39	BiOI/ ZnFe_2O_4 /MIL-88B(Fe)	Preparation of ZnFe_2O_4 /MIL-88B(Fe) from MIL-88B(Fe) and ZnFe_2O_4 deposition, followed by incorporation of BiOI from its precursors on the surface of as-prepared ZnFe_2O_4 /MIL-88B(Fe) via in-situ deposition.	AB92, MB and phenol degradation	[160]
40	Ag_3PO_4 / BiPO_4 /MIL-88B(Fe)/g- C_3N_4	Preparation of MIL-88B(Fe)/g- C_3N_4 from MIL-88B(Fe) and g- C_3N_4 deposition, followed by incorporation of Ag_3PO_4 / BiPO_4 from its precursors on the surface of as-prepared MIL-88B(Fe)/g- C_3N_4 via in-situ deposition.	AB92 degradation	[161]
41	MIL-100(Fe)/ BiVO_4	Prepared BiVO_4 was incorporated with MIL-100(Fe) from its precursors via hydrothermal synthesis.	O_2 production	[162]
42	MIL-100(Fe)/ Bi_2S_3	Prepared MIL-100(Fe) was incorporated with Bi_2S_3 from its precursors via hydrothermal synthesis.	RhB degradation	[163]

43	MIL-100(Fe)/Bi ₂ WO ₆	Incorporation of Bi ₂ WO ₆ from its precursors on the surface of as-prepared MIL-100(Fe) via solvothermal synthesis.	Salicylic acid	[164]
44	MIL-100(Fe)/Bi ₂ MoO ₆	Incorporation of Bi ₂ WO ₆ from its precursors on the surface of as-prepared MIL-100(Fe) via solvothermal synthesis.	RhB degradation	[165]
45	MIL-100(Fe)/Bi ₁₂ O ₁₇ Cl ₂	Ball-milling treatment of the as-prepared MIL-100(Fe) and Bi ₁₂ O ₁₇ Cl ₂ mixture.	Cr(VI) reduction and photocatalytic activation of persulfate for BPA degradation	[166]
46	HKUST-1/Bi ₂ O ₃	Firstly, HKUST-1 was prepared using the liquid phase epitaxy (LPE) method. Subsequently, triphenylbismuth (BiPh ₃) was injected quickly into the solution containing the as-prepared HKUST-1 and heated at 65°C for 36 h. Finally, the BiPh ₃ /HKUST-1 sample was irradiated with 255 nm UV light for obtaining HKUST-1/Bi ₂ O ₃ composite.	Nuclear fast red (NFR) degradation	[167]
47	HKUST-1/BiVO ₄	Prepared HKUST-1 was incorporated with BiVO ₄ from its precursors via hydrothermal deposition.	Disulfine blue (DB) and rose bengal (RB) degradation	[168]

48	Bi ₃ PO ₄ /Bi ₂ S ₃ /HKUST-1	The HUST-1 and the precursors of Bi ₃ PO ₄ and Bi ₂ S ₃ were sonicated for 40 min, then the obtained solution was treated by the hydrothermal method.	Toluidine blue (TB) and auramine-O (AO) degradation	[169]
49	Ag ₃ PO ₄ /Bi ₂ S ₃ /HKUST-1	The HUST-1 and the precursors of Ag ₃ PO ₄ and Bi ₂ S ₃ were sonicated for 40 min, then the obtained solution was treated by the hydrothermal method.	Trypan blue (TB) and vesuvine (VS) degradation	[170]
50	MOF-5/BiOBr	Ultrasonic treatment and magnetic stirring of the as-prepared MOF-5 and BiOBr mixture.	MO degradation	[171]
51	MIL-101(Cr)/BiVO ₄	Prepared BiVO ₄ was incorporated with MIL-101(Cr) from its precursors via hydrothermal deposition.	RhB degradation	[172]
52	BUC-21/Bi ₂₄ O ₃₁ Br ₁₀	Ball-milling treatment of the as-prepared BUC-21 and Bi ₂₄ O ₃₁ Br ₁₀ mixture.	Cr(VI) reduction	[44]
53	Co/Ni-mixed-MOF/BiFeO ₃	Hydrothermal treatment of the mixture containing the as-prepared BiFeO ₃ and the precursors of Co/Ni-mixed-MOF.	4-nitrophenol (4-NP) degradation	[173]

54	$\text{Bi}_{25}\text{FeO}_{40}/\text{MIL-101}(\text{Cr})/\text{polythiophene (PTH)}$	<p>Ultrasonication of CHCl_3 solution containing the as-prepared $\text{MIL-101}(\text{Cr})$, $\text{Bi}_{25}\text{FeO}_{40}$ and thiophene. Subsequently, anhydrous ferric chloride was added into the suspension and stirred for 4 h in an ice bath.</p>	RhB degradation	[103]
55	$\text{CuWO}_4/\text{Bi}_2\text{S}_3/\text{ZIF-67}$	<p>Preparation of $\text{CuWO}_4/\text{Bi}_2\text{S}_3$ from CuWO_4 and Bi_2S_3 deposition, followed by incorporation of ZIF-67 from its precursors on the surface of as-prepared $\text{CuWO}_4/\text{Bi}_2\text{S}_3$ via in-situ deposition.</p>	Metronidazole (MTZ) and cephalexin (CFX) degradation	[121]

2.1 ZIF-8/bismuth-based semiconductor composites

Zeolitic imidazolate framework-8 (ZIF-8), a typical and unique member of the MOFs family, is a highly porous structure constituted up from 2-methylimidazole linkers and zinc ions [174, 175]. It exhibits ultrahigh specific surface area up to $1600 \text{ m}^2\text{g}^{-1}$ with zeotype topology and a pore aperture of six-ring of 3.4 \AA [176]. Being compared with the other MOFs, ZIF-8 not only has a good chemical/thermal stability but also possesses an easy synthesis method to obtain uniform structures with good crystallinity. In recent years, the applications of ZIF-8 were extended in many fields like gas storage/separation [177-179], drug delivery [180, 181] and chemical sensing [182, 183]. In 2014, our research group firstly reported the photocatalytic activity of ZIF-8 against the MB degradation under UV light [184]. However, the large bandgap energy (5.1 eV) highly restrict its potential applications under visible light illumination. Hence, new strategies and approaches are required to develop for improving the use of solar energy. The coupling of bismuth-based semiconductors to prepare composites with ZIF-8 is also attractive because changing interfacial interactions results in new properties. For example, enhancing interfacial charge transfer, prolonged carrier lifetime and wider solar utilization spectrum can be obtained from ZIF-8/bismuth-based semiconductor composites. Up to now, some composites constructed from ZIF-8 and bismuth-based semiconductors were reported [125, 126, 128, 185]. In this section, two representative cases were highlighted as the following.

Photocatalytic fixation of N_2 to NH_3 can be performed at ambient conditions, so it is a sustainable, clean and safe NH_3 synthetic approach [186-188]. Nowadays, a number of researchers have focused on developing new photocatalysts for the reduction of N_2 to NH_3 . Among them, there are many reports about the establishment of an experimental system based on MOFs [189, 190] or bismuth-based photocatalysts [191-194]. However, the traditional photocatalytic system such as a solid-liquid bi-phase reaction system where the reaction fluid enveloped the whole surface of the catalyst. In such a condition, the photocatalytic system can only fixate the N_2 dissolved in water, resulting in lower activity due to the slow diffusion rate and poor solubility of N_2 [195, 196]. In other words, the key to the mentioned challenge is the deficiency of direct contact between the photocatalyst surface and gas phase N_2 .

In order to solve this problem, Liu and co-workers [125] synthesized a hydrophobic-

hydrophilic photocatalyst with a gas-liquid-solid triphasic reaction interface, where the surface of hydrophobic ZIF-8 was incorporated with the hydrophilic $\text{Bi}_4\text{O}_5\text{Br}_2$ to prepare a novel photocatalyst $\text{Bi}_4\text{O}_5\text{Br}_2/\text{ZIF-8}$ composite. In their study, the successful fabrication of $\text{Bi}_4\text{O}_5\text{Br}_2/\text{ZIF-8}$ composites was confirmed by UV-visible diffuse reflectance spectrum (UV-vis DRS), Fourier transforms infrared spectra (FTIR), and powder X-ray diffraction (PXRD) results. It was observed from the transmission electron microscopy (TEM) micrographs of the ZIF-8 specimen, the pure ZIF-8 consisted of 100-300 nm-sized nanosheet structures (Figure 3(a)). After the combination of $\text{Bi}_4\text{O}_5\text{Br}_2$ and ZIF-8, it was clear that the $\text{Bi}_4\text{O}_5\text{Br}_2$ nanoparticles were doped on the ZIF-8 surface, the lattice spacing of 0.302 nm indexed to the exposed crystalline surface of $\text{Bi}_4\text{O}_5\text{Br}_2$ (Figure 3(b)). Being compared with the slight agglomeration of $\text{Bi}_4\text{O}_5\text{Br}_2$ (Figure 3(c)), the agglomeration of $\text{Bi}_4\text{O}_5\text{Br}_2$ was effectively avoided with the presence of ZIF-8 (Figure 3(d)), which might be beneficial to the follow-up photocatalytic efficiency. Figure 3(e) demonstrated the activities of photocatalytic N_2 fixation on the as-prepared materials. The large bandgap of ZIF-8 made it inactive and unsuitable for photocatalytic N_2 fixation. The rate of NH_3 generation over the $\text{Bi}_4\text{O}_5\text{Br}_2$ photocatalyst was $90.586 \mu\text{mol} \cdot \text{h}^{-1} \cdot \text{g}^{-1}$. However, the rate of NH_3 generation over the $\text{Bi}_4\text{O}_5\text{Br}_2/\text{ZIF-8}$ composites was firstly increased and then decreased with the increase in the contents of ZIF-8. The optimal photocatalyst ($\text{Bi}_4\text{O}_5\text{Br}_2/\text{ZIF-8}$ (30%)) showed the most productive activity of $327.338 \mu\text{mol} \cdot \text{h}^{-1} \cdot \text{g}^{-1}$, which was 3.6 times higher than the $\text{Bi}_4\text{O}_5\text{Br}_2$ photocatalyst. Nevertheless, the UV-vis DRS spectra and Mott-Schottky plots of $\text{Bi}_4\text{O}_5\text{Br}_2$ and ZIF-8 suggested that ZIF-8 should not participate in the photocatalytic reaction, which can be ascribed to the mismatch of energy levels between $\text{Bi}_4\text{O}_5\text{Br}_2$ and ZIF-8, thereby the photo-generated electrons cannot be effectively utilized during the photocatalytic process (Figure 3(f)). To investigate the active role of ZIF-8 in $\text{Bi}_4\text{O}_5\text{Br}_2/\text{ZIF-8}$ (30%), the water contact angle (CA) of ZIF-8 and $\text{Bi}_4\text{O}_5\text{Br}_2/\text{ZIF-8}$ (30%) was measured. The CA of ZIF-8 was observed $147 \pm 2^\circ$, demonstrating the super-hydrophobic nature of ZIF-8 (Figure 3(g)). But after the $\text{Bi}_4\text{O}_5\text{Br}_2$ deposition, the CA was found $17 \pm 2^\circ$, demonstrating that the surface of photocatalyst became hydrophilic (Figure 3(h)). The above results indicated that hydrophobic ZIF-8 was inclined to capture atmosphere-connected bubbles, resulting in the formation of micro/nanoscale level tri-phase mixed air, liquid and solid phases. Thus, the triphasic interface offered a direct supply of N_2 to the photocatalytic interface from the air. For the traditional

bi-phase photocatalytic system where the reaction fluid (liquid phase) enveloped the whole surface of the catalyst (solid surface). In such a condition, the photocatalytic system can only fixate the N_2 dissolved in the bi-phase system results in lower activity due to insufficient N_2 supply. Just by comparison, N_2 can be directly supplied from the air phase in the tri-phase system. In order to verify this inference, the rate of N_2 fixation in different light intensities over $Bi_4O_5Br_2$ and $Bi_4O_5Br_2/ZIF-8$ (30%) was investigated (Figure 3(i)). It was obvious that with increasing light intensities, the photocatalytic activity of $Bi_4O_5Br_2$ was no further increase. This can be explained that the N_2 consumption rate was more rapid than the supply rate due to its slow diffusion rate and poor solubility in water. It was concluded from these results that the N_2 mass transfer mainly controlled the photocatalytic process. In contrast, the reaction rates over $Bi_4O_5Br_2/ZIF-8$ (30%) were linearly increased with light intensities, revealing that the photocatalytic efficiency of triphasic system increased with the N_2 supply. In that way, the photocatalytic activity of the photocatalyst can be significantly enhanced by the tri-phase system (Figure 3(j)). In this study, hydrophobic ZIF-8 could not directly participate in the photocatalytic process due to its large bandgap. However, the construction of $Bi_4O_5Br_2/ZIF-8$ composites was beneficial to set up an effective tri-phase contact interface for rapid delivery of N_2 , thereby enhancing the photocatalytic performance. More importantly, as shown in Table 2, being compared with some traditional TiO_2 -based materials, metal sulfides, carbonaceous materials, hydrous oxides, bismuth-based semiconductors and MOFs, the photocatalytic N_2 fixation activity of the as-prepared $Bi_4O_5Br_2/ZIF-8$ composite was relatively competitive, suggesting it could effectively convert atmospheric N_2 to NH_3 under UV or UV-visible light illumination.

Table 2. Comparison of the $Bi_4O_5Br_2/ZIF-8$ composite with other representative photocatalysts for N_2 fixation.

Photocatalyst	Light source	Scavenger	NH_3 ($\mu mol \cdot h^{-1} \cdot g^{-1}$)	Ref.
MoS_2	500 W Xe lamp ($\lambda > 420$ nm)	None	325	[197]
Fe-doped TiO_2	360 W Mercury lamp ($\lambda =$ 254 nm)	None	10	[198]

Ru-loaded TiO ₂	150 W Xe lamp	Ethanol	22.7	[199]
Cd _{0.5} Zn _{0.5} S	300 W Xe lamp ($\lambda > 400$ nm)	None	2.84	[200]
BiOBr with oxygen vacancies	300 W Xe lamp ($\lambda > 420$ nm)	None	104.2	[201]
Carbon-tungstic acid hybrids	500 W Xe lamp	None	205	[202]
g-C ₃ N ₄	250 W Sodium lamp	Ethanol	7.2	[69]
Ru@n-GaN nanowires	290-380 nm UV irradiation	None	120	[203]
NH ₂ -MIL-125(Ti)	300 W Xe lamp ($\lambda > 400$ nm)	None	12.3	[189]
Bi ₄ O ₅ Br ₂ /ZIF-8	300 W Xe lamp	None	327.338	[125]

Figure 3. TEM micrographs of (a) ZIF-8, (b) and (d) Bi₄O₅Br₂/ZIF-8 (30%), (c) Bi₄O₅Br₂ nanoparticles, (e) photocatalytic N₂ fixation activities of as-prepared materials, (f) band potentials of ZIF-8 and Bi₄O₅Br₂, (g)-(h) contact angles of ZIF-8 and Bi₄O₅Br₂/ZIF-8 (30%), (i) photocatalytic efficiencies of Bi₄O₅Br₂ and Bi₄O₅Br₂/ZIF-8 (30%) versus light intensities and (j) photocatalytic mechanism of Bi₄O₅Br₂/ZIF-8 (30%) [125], copyright (2019) Elsevier.

Bi₂S₃ is a prominent lamellar-structured semiconductor, which possesses a small bandgap of 1.3-1.7 eV and has drawn much consideration among researchers due to its good photoconductivity and photosensitivity toward visible and near-IR light [204-206]. But the aggregation during reactions, the rapid recombination of photo-generated charges, photo-corrosion property and low adsorption capacity for target pollutants severely restrict the utilization of pure Bi₂S₃. Because of the advantages of ZIF-8 (high surface area and stability) and Bi₂S₃ (high optical absorbance), they can be good partners to overcome the rapid recombination of photo-generated charges. For instance, Ding and co-workers [126] successfully made-up Bi₂S₃/ZIF-8 composites (denoted as B@Z) through the in-situ self-assembly approach (Figure 4(a)). The scanning electron microscopy (SEM) micrographs (Figure 4(b)-(e)) demonstrated that Bi₂S₃ displayed a regular nanorod structure with a smooth surface, while ZIF-8 was composed of hexahedrons with 200 nm average-sized particle. It was observed in the B@Z composites, the Bi₂S₃ surface turned out to be rough and was completely

covered by the ZIF-8 nanocrystals, suggesting that the development of excellent core-shell heterostructures. However, it was remarkable to find that the ZIF-8 size implanted in or dropped from the Bi_2S_3 nanorods was smaller (approximately 100 nm) than the pure ZIF-8 nanocrystals, signifying the confinement effect of the Bi_2S_3 nanorods [207]. Moreover, the TEM micrographs (Figure 4(f)) demonstrated that the ZIF-8 nanocrystals were closely distributed on the surface of the Bi_2S_3 nanorods. The attachment of ZIF-8 crystals on Bi_2S_3 nanorods surface was solid that even strong ultrasonication for 1 h did not detach them from the Bi_2S_3 nanorods (Figure 4(g)). This stable attachment of ZIF-8 was due to the covalent bonding of Bi-S-Zn. Additionally, it was necessary to be indicated that all the peaks in Zn 2p, Bi 4f and S 2p XPS spectra shifted to higher binding energies, which provided further evidence of the formation of Bi-S-Zn bonds. With respect to photocatalytic activities, all the B@Z composites showed increased activities towards RhB degradation than pure Bi_2S_3 and Degussa P25 photocatalysts under visible light irradiation. There were two main reasons for the above experimental phenomenon: (i) the light adsorption ranging from 700 to 400 nm in the visible light region was remarkable for the B@Z composites; (ii) the B@Z assembly can devastate the recombination of charge carriers. Active-species-capture studies suggested that holes (h^+) and superoxide radicals ($\cdot\text{O}_2^-$) played dominating roles in this photocatalytic system. Usually, the diffusion of $\cdot\text{O}_2^-$ into the bulk solution is difficult [208], and only the adsorbed pollutant molecules can be photodegraded. Hence, the porous ZIF-8 was in favor of transporting RhB molecules, which can promote $\cdot\text{O}_2^-$ to act more significantly in the degradation process. In such a way, the photo-generated charges will separate more efficiently (Figure 4(h)). In this study, the presence of ZIF-8 made the B@Z composites possess more active sites and penetrable paths for accelerating the transfer of active radicals ($\cdot\text{O}_2^-$ and h^+) and the target pollutants to the inner structure. In such a way, the photo-generated charge pairs were sufficiently separated and can be fully utilized for the degradation of organic pollutants.

Figure 4. (a) The fabrication of the Bi_2S_3 /ZIF-8 core-shell composites, (b)-(e) SEM micrographs of pure Bi_2S_3 , ZIF-8, B@Z-7, and B@Z-10, (f)-(g) TEM micrographs of B@Z-10 and the material after treatment with ultrasonication for 1 h, and (h) the photocatalytic mechanism for the RhB decomposition over B@Z-10 [126], copyright (2018) Royal Society of Chemistry.

2.2 (NH₂)-UiO-66/bismuth-based semiconductor composites

UiO-66 belongs to the UiO family, which was firstly reported by Cavka and co-workers at Oslo University [209]. The chemical composition of UiO-66 is $\text{Zr}_6\text{O}_4(\text{OH})_4(\text{BDC})_6$ (BDC = terephthalic acid). UiO-66 exhibits mechanical, chemical and extremely high thermal stabilities because of the high affinity and strong bonding between carboxylate O atom and Zr(IV). Therefore, it can be treated in organic solvents as well as in water environments, and even found it is stable and tolerable to the acid solution [210-212]. Such exceptional properties make UiO-66 more useful in many fields such as photocatalysis [213-215] and gas adsorption/separation [216, 217]. However, UiO-66 is unable to absorb the visible light because the redox potential of Zr₆ secondary-building units (SBUs) in UiO-66 possesses a higher energy level than the BDC linkers' LUMO. Therefore, it is extremely necessary to modify the UiO-66 and make it responsive as a visible light photocatalyst [218]. As a facile and feasible method, the modification of organic ligand can alter the energy bandgap of MOFs to some degree, which expands the absorption ability of MOFs to visible light [219]. Silva et al. [220] reported the synthesized NH₂-UiO-66 via substituting H₂BDC by 2-amino benzene dicarboxylic acid (H₂BDC-NH₂). Contrary to the UiO-66, NH₂-UiO-66 exhibits absorption in UV light as well as in visible regions ranging from 300 to 440 nm. The shifting of absorption into the visible region can be attributed to the amino substituent is responsible for bathochromic and auxochromic properties in the atomic framework. Furthermore, the pure NH₂-UiO-66 has been employed for the photocatalytic degradation of organic pollutants [214], As(III) oxidation [221], Cr(VI)/CO₂ reduction [222-224] and H₂ evolution [220]. To further improve the photocatalytic efficiencies of UiO-66 or NH₂-UiO-66, a relatively ideal solution is to construct heterogeneous photocatalysts with narrow bandgap semiconductors [33, 49, 50]. Up to now, large amounts of (NH₂)-UiO-66/bismuth-based semiconductor composites have been constructed and proven to enhance the photocatalytic reactions due to the mutual interactions and synergistic effect of both coupled components [119, 129-139].

BiOX (X = Br, Cl, I) are economic and effective photocatalysts. They possess exceptional layered structure and indirect transition mode that help in the effective transfer and separation of charge carriers [57, 58]. Among different BiOX photocatalysts, BiOBr has a 2D lamellar structure and a narrow bandgap, which makes it the most suitable photocatalyst in visible light irradiation

[225-227]. However, 2D BiOBr nanoplates are tending to agglomerate, which leads to low surface area, limited active sites and weak affinity for target pollutants. Furthermore, the pure BiOBr does not show enough wide range of light absorption and its recombination of photo-generated electron-hole pairs is comparatively rapid [107, 228]. Thus, incorporating the BiOBr with $\text{NH}_2\text{-UiO-66}$ or UiO-66 is not only expected to avoid the aggregation of pure BiOBr, but also possible to improve the photo-absorption ability and enhance charge separation and migration.

In 2015, Sha et al. [133] firstly synthesized UiO-66/BiOBr composites with different proportions of BiOBr via a convenient solution method. All the UiO-66/BiOBr composites exhibited excellent photocatalytic activities against the RhB degradation in visible light. The higher efficiencies offered by the UiO-66/BiOBr composites should be attributed to the large available surface area of BiOBr in the composites and good contact between BiOBr and UiO-66. In order to expand the applications of UiO-66/BiOBr composite, Xue et al. [132] subsequently synthesized visible-light-responsive UiO-66/BiOBr photocatalyst through a simple solution process to efficiently photodegrade atrazine, which is a typical herbicide and has been posing a serious threat to the ecological environment. As shown in Figure 5(a)-(b), the BiOBr specimen was comprised of the plane and sporadic flakes with sizes from 200 to 600 nm and the nanoflakes of BiOBr in composites were thinner than pure BiOBr. Furthermore, the PXRD pattern of BU-3 (the as-prepared composites were defined as BU- x , x was the molar ratio of Bi to Zn) demonstrated all the diffraction peaks belonged to pure BiOBr and UiO-66 (Figure 5(c)). It was worth noting that the pure BU-3 and BiOBr had similar adsorption edge of 440 nm, the corresponding E_g values were estimated as 2.82 and 2.80 eV, indicating the UiO-66/BiOBr composites possessed visible light absorption properties (Figure 5(d)). For the removal of atrazine, as demonstrated in Figure 5(e), the adsorption capacities of atrazine were 1.8%, 2.1%, 1.6%, and 2.5% for physical mixture sample, UiO-66, BiOBr, and BU-3, respectively. This phenomenon may be attributed to the possible interactions between BiOBr and UiO-66 resulted in the arbitrary growth of BiOBr, which can increase the available interspace in the BU-3. Thus, the increased surface of the composite provided a large space for more atrazine molecules and enhanced the degradation of atrazine molecules.

As expected, the optimal BU-3 could degrade almost 88% of the atrazine, while the physical mixed sample could degrade only 74% of the atrazine. The reasons for superior photocatalytic

activities of BU-3 were summarized as follow: (i) UiO-66 nanocrystals regularly distributed on the surface of BiOBr, which was beneficial to avoid overlay of BiOBr nanoflakes on each other. (ii) the fabrication of UiO-66/BiOBr composites enhanced the separation efficiency of photo-generated charges. Furthermore, the effects of typical environmental aspects (i.e., water matrix, common anions, pH) were extensively studied to find out their impact on the atrazine degradation. In the strong acidic condition of $\text{pH} = 3.1$, the rate of degradation of atrazine was found the fastest one, which was mainly attributed to the surface of the composite was positively charged under acidic conditions. Considering that the chlorine atoms on the atrazine molecules possessed electron-withdrawing effect, thus the composite demonstrated stronger electrostatic attraction to the atrazine. The photocatalytic efficiency was apparently inhibited by HCO_3^- and SO_4^{2-} due to that they are very strong scavengers toward hydroxyl radical ($\cdot\text{OH}$) and h^+ [229]. Moreover, the atrazine removal efficiencies in river water, tap water, and mineral water were obviously lower than those in pure water. It may be due to the presence of organic matters in the above water matrices will consume the produced active radicals. As to the UiO-66/BiOBr composite, the photo-generated charges can be excited under visible light, the presence of UiO-66 can facilitate the charges transfer. Therefore, more h^+ , $\cdot\text{OH}$, and $\cdot\text{O}_2^-$ radicals can be formed, which played significant roles in the degradation of atrazine (Figure 5(f)). Among the most MBCs, the bismuth-based semiconductors were usually fastened or even glued to the MOFs particles. However, this study indicated that BiOBr flakes can be interspersed with UiO-66, which can effectively inhibit the BiOBr agglomeration, thereby significantly improving the photolytic activity. Moreover, the authors firstly applied the UiO-66/BiOBr composite for atrazine photodegradation, rather than the common organic dyes. Nevertheless, it should be admitted that the photodegradation efficiency of atrazine over the UiO-66/BiOBr composite should be further enhanced. In 2019, Alkayal and Hussein [230] adopted deposition process to synthesize x wt% $\text{Ag@Mg}_4\text{Ta}_2\text{O}_9$ nanoparticles (x was the Ag content in the composite) for photocatalytic degradation of atrazine. Under the same light source irradiation (300 W xenon lamp with 420 nm cut-off filter), 100 $\text{mg}\cdot\text{L}^{-1}$ of atrazine can be completely removed with 40 min over the optimal 2.0 wt% $\text{Ag@Mg}_4\text{Ta}_2\text{O}_9$ (photocatalyst dosage was 2.0 $\text{g}\cdot\text{L}^{-1}$). Previous studies [55, 231, 232] had demonstrated that the bandgap of bismuth-based semiconductor could be narrowed by adjusting its morphology to 3D structure. Considering that the BiOBr in this study

possessed flake-like structure and the E_g value of BU-3 was only 2.82 eV. Therefore, the morphology of BiOBr is of interest to regulate into flower-like, sponge-like or cubic-like 3D structures to fasten UiO-66 nanoparticles, which might improve its visible-light-driven photocatalytic activities.

Figure 5. (a)-(b) SEM images of pure BiOBr and BU-3 composite, (c)-(d) PXRD patterns and UV-vis DRS spectra of BiOBr, UiO-66 and BU-3 composite, (e) the degradation of atrazine in visible light radiation by different photocatalysts, insert: adsorption curves of atrazine by the samples, (f) a possible reaction mechanism of atrazine degradation over UiO-66/BiOBr composite [132], copyright (2019) Elsevier.

After that, various $\text{NH}_2\text{-UiO-66/BiOBr}$ were reported by three research groups [136-138]. For instance, Hu and co-workers adopted solvothermal method to grow BiOBr nanosheets on the $\text{NH}_2\text{-UiO-66}$ surface for preparing the $\text{NH}_2\text{-UiO-66/BiOBr}$ composites (as illustrated in Figure 6(a)) [137]. In detail, a prescribed amount of the as-prepared $\text{NH}_2\text{-UiO-66}$ and $\text{Bi(NO}_3)_3 \cdot 5\text{H}_2\text{O}$ were dispersed into mannitol using sonicator, then the mannitol solution containing the ionic liquid $[\text{C}_{16}\text{mim}]\text{Br}$ was added dropwise. The reaction mixture was further magnetically mixed for a preset time and subsequently heated for 24 h at 140°C . Then the precipitates were finally collected through cleanout and vacuum drying processes. Figure 6(b)-(c) displayed the SEM and TEM images of $\text{NH}_2\text{-UiO-66/BiOBr}$ composites (named as NU/BOB-15). It can be found that the BiOBr nanosheets distributed homogeneously on the surface of $\text{NH}_2\text{-UiO-66}$, indicating the two components coupled together tightly. As a consequence, the NU/BOB-15 exhibited enhanced photocatalytic activities for Cr(VI) reduction and TC degradation under simulated solar light than pure BiOBr and $\text{NH}_2\text{-UiO-66}$. This result should be ascribed to the unique features of the as-prepared composite, such as intimate interface contacts for the separation of photo-generated charge carriers and enlarged surface area for pollutant adsorption.

Unlike the previous study, Yang and co-workers [136] adopted an alternative route for the synthesis of $\text{NH}_2\text{-UiO-66/BiOBr}$ in the same year. Briefly, the as-prepared $\text{NH}_2\text{-UiO-66}$ powders were dispersed in KBr solution with the aid of ultrasonic oscillation, then the obtained suspension was dropwise added to the glycerol solution containing $\text{Bi(NO}_3)_3 \cdot 5\text{H}_2\text{O}$ powders. After strong

magnetic stirring for 3 h, the final products (light yellow precipitate) were gathered by washing and vacuum drying at 353 K for 20 h. As revealed in Figure 6(d)-(e), the NH₂-UiO-66/BiOBr composite (denoted as BUN-20) consisted of nanosheets that were settled in a specific way to adapt flower-shaped morphologies. The plausible formation process of BUN-20 composite can be concluded as follows: (i) the Bi³⁺ ions in Bi(NO₃)₃·5H₂O were transformed into alkoxides (Bi(C₃H₇O₃)²⁺) after reacting with glycerol, which inhibited the hydrolysis of Bi³⁺ ions and a molecular level homogeneity was attained for the better interactions with the other component [233]. (ii) The rate of diffusion of Bi(C₃H₇O₃)²⁺ became slow due to the high viscosity of the solution containing NH₂-UiO-66 particles surrounding by Br⁻ ions [234]. (iii) Upon the dropwise addition of the suspension, the Br⁻ ions around NH₂-UiO-66 particles rapidly reacted with Bi(C₃H₇O₃)²⁺ to produce BiOBr nanoplates. The BiOBr nanoplates were accumulated on the surface of NH₂-UiO-66 and stuck on by intimate interaction, thereby adapting the flower-like structures. With respect to photocatalytic activity, BUN-20 exhibited good structural stability and the best performance on the removal of NOR. The removal efficiency of NOR (10 mg·L⁻¹) over BUN-20 (0.3 g·L⁻¹) was up to 93.60% after simulated sunlight irradiation for 180 min (Figure 6(f)). The BUN-20 photocatalytic rate was observed 0.01340 min⁻¹, which was almost 2.4 and 31.9 times of the pure BiOBr and NH₂-UiO-66, respectively. Furthermore, BUN-20 showed improved mineralization property compared with the physical mixture sample (denoted as Mix-20), namely 60.58% of TOC can be removed within prolonged 270 min under identical conditions (Figure 6(g)). In general, the NH₂-UiO-66/BiOBr composites constructed in this study should be classified as Type II heterojunctions, as illustrated in Figure 6(h), in which NH₂-UiO-66 played a significant role in conducting charges in the composites. The photo-generated electrons on the lowest unoccupied molecular orbital (LUMO) of NH₂-UiO-66 were used in the reduction of O₂ into ·O₂⁻. Meanwhile, the light-excited holes on the valence band (VB) of BiOBr were involved in the oxidation of H₂O to form ·OH. Ultimately, h⁺, ·O₂⁻, and ·OH involved in degrading the NOR molecules, and the degradation of NOR molecules might be depicted by the given below reaction equations. Summarily, the major innovation of this research was the synthesis method of NH₂-UiO-66/BiOBr composites. The strategy overcame the disadvantages of typical synthetic route, such as the need of high pressure and temperature, template agents, etc. Additionally, this study exhibited the MBC's great potential in eliminating antibiotics in

water environments. For the ease of comparison of the selected study, Table 3 summarized some recently reported photocatalysts for NOR photocatalytic degradation. Taking the dosage, NOR initial concentration, light source, reaction time, photocatalytic efficiency and mineralization degree into consideration, the $\text{NH}_2\text{-UiO-66/BiOBr}$ should be a good candidate for NOR removal in wastewaters.

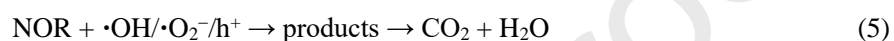
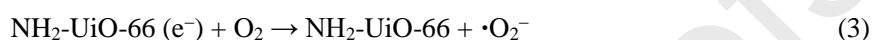
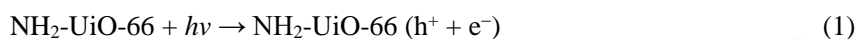


Table 3. Comparison of the $\text{NH}_2\text{-UiO-66/BiOBr}$ with other photocatalysts for NOR degradation.

Photocatalyst	Dosage ($\text{g}\cdot\text{L}^{-1}$)	NOR concentration ($\text{mg}\cdot\text{L}^{-1}$)	Light source	Time (min)	Efficiency (%)	TOC removal (%)	Ref.
$\text{FeTiO}_3/\text{BiFeO}_3$	1.0	5.0	500 W Xenon lamp ($\lambda > 420 \text{ nm}$)	150	61.6	No data	[235]
$\text{NH}_2\text{-UiO-66/CoTiO}_3$	1.0	20.0	300 W Xenon lamp ($\lambda > 420 \text{ nm}$)	60	90.13	No data	[236]
$\text{BiFeO}_3/\text{CuBi}_2\text{O}_4/\text{BaTiO}_3$	1.0	10.0	500 W Xenon lamp	60	63.5	60.3	[237]
BiOCl with oxygen vacancies	0.5	5.0	300 W Xenon lamp ($\lambda > 420 \text{ nm}$)	120	about 60.0	No data	[238]
$\text{BiOBr}/\beta\text{-Bi}_2\text{O}_3$	0.5	20.0	500 W Xenon lamp with AM 1.5G filter	60	70.0	35.0	[239]
$\text{BiVO}_4/\text{BiOCl}$	0.5	5.0	150 W Xenon lamp ($\lambda > 420 \text{ nm}$)	60	80.0	No data	[240]
ZnS/RGO	1.0	20.0	300 W Hg vapor lamp	240	92.0	No data	[241]
$\text{CeO}_2/\text{g-C}_3\text{N}_4$	1.0	10.0	150 W Xenon lamp	60	46.1	No data	[242]

$(\lambda > 420 \text{ nm})$							
Ag/AgCl-CeO ₂	0.6	10.0	300 W Xenon lamp $(\lambda > 420 \text{ nm})$	90	91.0	59.61	[243]
WO ₃ /Ag@Ag ₂ O	0.6	10.0	300 W Xenon lamp $(\lambda > 420 \text{ nm})$	120	81.5	25.72	[244]
NH ₂ -UiO-66/BiOBr	0.3	10.0	500 W Xenon lamp	180	93.6	60.58	[136]

Figure 6. (a) The procedure for the preparation of NH₂-UiO-66/BiOBr in Hu and co-workers' study, (b)-(c) SEM and TEM images of the NU/BOB-15 composite, (d)-(e) SEM images of the BUN-20 composite in Yang and co-workers' study, (f) removal performances of NOR in the existence of diverse samples (pH = 7), (g) TOC removal efficiency of BUN-20 and Mix-20, (h) the possible reaction mechanism of NOR over the BUN-20 in simulated sunlight [136, 137], copyright (2019) Elsevier.

BiOI, a typical p-type semiconductor, can be deemed as a promising BiOX photocatalyst owing to its anisotropic layered structure and narrow bandgap (1.7-1.8 eV), which makes it powerfully responsive towards visible light [245, 246]. However, two fundamental challenges strictly limit its photocatalytic activity: the first one is poor conductivity and the second one is the rapid recombination of photo-generated charge carriers. Such issues were addressed by the fabrication of BiOI with TiO₂ [247], ZnO [248], BiOCl [249], MnNb₂O₆ [250] and g-C₃N₄ [251, 252] to prepare binary composites with improved photocatalytic activities. Considering that MOFs as a class of highly porous materials can offer more channels for the transfer of photo-generated charges and photodegradation products, which can effectively inhibit the photocatalyst deactivation. Thus, the construction of a ternary photocatalytic system containing BiOI and MOFs can be an effective approach to advance photocatalytic activities. As illustrated in Figure 7(a), Liang and co-workers [119] synthesized a ternary BiOI/NH₂-UiO-66/g-C₃N₄ composite (denoted as BiOI@UNCN-*x*, *x* referred to the nominal weight ratios of NH₂-UiO-66/g-C₃N₄ (UNCN) to BiOI) by in-situ solvothermal-hydrothermal method to achieve broadening visible light absorption range, enlarging the surface area, and accelerating the photo-generated charges migration. The SEM and TEM images (Figure 7(b)-(c)) revealed that the BiOI@UNCN possessed sandwich-like structures, which

was beneficial to increase its contact area with the target pollutants. The surface areas of the BiOI@UNCN-40 and BiOI@UNCN-60 composites were increased to 123 and 152 $\text{m}^2\cdot\text{g}^{-1}$, respectively. Comparing the surface areas of $\text{NH}_2\text{-UiO-66}$ ($842 \text{ m}^2\cdot\text{g}^{-1}$) [253] and UNCN ($265 \text{ m}^2\cdot\text{g}^{-1}$), the surface areas of BiOI@UNCN-*x* were much lower, but the surface areas were much higher than the pure $\text{g-C}_3\text{N}_4$ ($35 \text{ m}^2\cdot\text{g}^{-1}$) and BiOI ($63 \text{ m}^2\cdot\text{g}^{-1}$) nanosheet [254]. The photocatalytic activities of the as-prepared composites were assessed by RhB and TC degradation in visible light. As illustrated in Figure 7(d)-(e), the activities of BiOI@UNCN composites were outstanding to that of the specific component such as UNCN, BiOI, and $\text{NH}_2\text{-UiO-66}$. This should be attributed to the ternary BiOI@UNCN composites can effectively separate the photo-generated charges. It was agreed with the electrochemical impedance spectra (EIS) Nyquist analysis and PL spectra analysis. More importantly, there was no apparent reduction in RhB degradation efficiency after the cycling experiment. After four cycling runs approximately 87.7% of RhB could be removed (Figure 7(f)), indicating that BiOI@UNCN composites can effectively inhibit the photo-corrosion and maintain good stability. Based on the electrochemical and active-specie-trapping experiment results, the excellent photocatalytic activity and good reliability of BiOI@UNCN were allocated to the establishment of n-p-n junction in ternary composites. And the Z-scheme photocatalytic mechanism could account for the photo-generated charges migration (Figure 7(g)). In detail, the electrons in conduction band (CB) of BiOI will be combined with the holes generated from the highest occupied molecular orbital (HOMO) of $\text{NH}_2\text{-UiO-66}$ and VB of $\text{g-C}_3\text{N}_4$. Then, the CB of $\text{g-C}_3\text{N}_4$ (-1.08 eV vs. NHE) and LUMO of $\text{NH}_2\text{-UiO-66}$ (-0.51 eV vs. NHE) were more negative than the redox potential of $\text{O}_2/\cdot\text{O}_2^-$ (-0.33 eV vs. NHE), the photo-generated electrons remained in the CB of $\text{g-C}_3\text{N}_4$ and LUMO of $\text{NH}_2\text{-UiO-66}$ can react with O_2 to produce $\cdot\text{O}_2^-$ radicals, which played a significant role in degrading RhB and TC. In the interim, the holes generated in VB of BiOI were inclined to decompose the organic pollutants. Additionally, the accumulated holes in the VB of BiOI (2.37 eV vs. NHE) could oxidize OH^- to produce $\cdot\text{OH}$ (1.99 eV vs. NHE), which was also responsible for the RhB and TC removal. In this study, the dominating roles of $\text{NH}_2\text{-UiO-66}$ were to increase the specific surface areas of the BiOI@UNCN composites and to make BiOI more dispersive in the ternary photocatalysts. BiOI, as a p-type semiconductor, was the crucial factor for accelerating the separation of the photo-generated charge carriers in the n-p-n type heterojunction

by Z-scheme mechanism. Although this type of migration of photo-generated electrons and holes retained the redox capacity of the photocatalyst, the photocatalytic activities for decomposition of organic pollutants should be further enhanced. For example, the degradation efficiency of RhB achieved by the optimal BiOI@UNCN-40 was lower than that of hexagonal boron nitride (h-BN)/g-C₃N₄ [255] and BiOCl/Bi₂O₂CO₃ [256] binary composites. Considering that the adsorption capacity of a photocatalyst has great influence on the subsequent photocatalytic process, thereby future work needs to focus on increasing the specific surface areas of the BiOI@UNCN-*x* composites to further enrich their active sites. Combining with the above merits, the implication of this research is that more ternary photocatalysts based on MOFs and bismuth-based semiconductors should be developed for environmental remediation.

Figure 7. (a) Schematic representation for BiOI@UNCN composites fabrication, (b)-(c) SEM and TEM images of BiOI@UNCN-40, (d)-(e) the degradation of TC and RhB over as-prepared materials in visible light, (f) the cyclic degradation of RhB over BiOI and BiOI@UNCN-40, (g) the proposed photocatalytic mechanism over the BiOI@UNCN-40 under visible light [119], copyright (2019) Elsevier.

As Bi-based ternary metal oxide photocatalysts, Bi₂MoO₆ ($E_g = 2.6$ eV) [257] and Bi₂WO₆ ($E_g = 2.75$ eV) [258] usually exhibit good photocatalytic activities under visible light. However, the Bi₂MoO₆ or Bi₂WO₆ shows low quantum yield, thus it was found to be unsuitable for the photocatalytic activities in practical applications. The coupling of MOFs to fabricate binary composites can enhance the photocatalytic activities of Bi₂MoO₆ and Bi₂WO₆. Ding and co-workers [130] fabricated UiO-66/Bi₂MoO₆ composites through a simple hydrothermal method. The UiO-66/Bi₂MoO₆ composites exhibited improved photocatalytic efficiencies against RhB degradation. More importantly, they also revealed that MOFs may be utilized as an admirable substrate for the photocatalysis in wastewater treatment applications. In 2020, Liu and co-workers [139] constructed a direct Z-scheme photocatalytic system by coupling Bi₂WO₆ with NH₂-UiO-66 via a hydrothermal process. The incorporation of NH₂-UiO-66 into Bi₂WO₆ can not only enhance its activity against the oxidation of NO, but also improve its selectivity to convert NO into NO₃⁻ or NO₂⁻. The incorporation of NH₂-UiO-66 supplied abundant active sites to enhance the photocatalytic reaction

and to improve the adsorption capacities of $\text{NH}_2\text{-UiO-66/Bi}_2\text{WO}_6$ composites. Furthermore, the direct Z-scheme system not only promoted the charge carriers transfer and migration, but also preserved the strong redox abilities of coupling components. This work indicated that MBCs had strong potential for handling low-concentration (approximately 500 ppb) air pollutants.

2.3 $(\text{NH}_2)\text{-MIL-125/bismuth-based semiconductor composites}$

Titanium (Ti) is a very potential element for the development of photocatalysts due to its low toxicity and redox activity. MIL-125 is composed of H_2BDC linkers and titanium-oxo-hydroxo ($\text{Ti}_8\text{O}_8(\text{OH})_4$) clusters and was firstly reported in 2009 [259]. MIL-125 exhibits thermal stability up to 360°C , which is an ultimate property for the development of photocatalysts at high temperatures. However, the energy bandgap of MIL-125 is wide (3.6 eV) like UiO-66, indicating that only UV light could be used to excite MIL-125 [260]. The structure of $\text{NH}_2\text{-MIL-125}$ is isostructural to MIL-125 and can be synthesized by just substituting $\text{H}_2\text{BDC-NH}_2$ instead of H_2BDC in the substrates. The $\text{NH}_2\text{-MIL-125}$ bandgap is about 2.6 eV [260], enabling it to possess semiconducting applications under visible light. This effect originates from the redshift in the valence band of MIL-125 by the donation of aromatic electrons from N-containing ligand [261]. However, intrinsic defects of $\text{NH}_2\text{-MIL-125}$ or MIL-125, such as poor conductivity, low stability, and rapid recombination of charge carriers result in relatively low photocatalytic activities [33, 262]. For $\text{NH}_2\text{-MIL-125}$ or MIL-125, the approach by combining with semiconductors for photocatalysis is frequently used. Very recently, $\text{NH}_2\text{-MIL-125}$ or MIL-125-based composites were constructed by different bismuth-based materials like Bi_2MoO_6 [144], Bi_2WO_6 [145, 146], BiOBr [148], BiOI [150], BiOCl [149], BiVO_4 [141, 142] and Bi_2S_3 [147]. In this section, some representative $(\text{NH}_2)\text{-MIL-125/bismuth-based semiconductor composites}$ for various practices were highlighted.

In 2019, Zhang et al. [144] adopted a facile approach to fabricate mesoporous $\text{NH}_2\text{-MIL-125/Bi}_2\text{MoO}_6$ core-shell composites via the solvothermal method with surface defects. As illustrated in Figure 8(a), a certain amount of prepared $\text{NH}_2\text{-MIL-125}$ (denoted as TiM) was suspended in absolute ethanol using probe sonicator. Then the ethylene glycol solution containing $\text{Bi}(\text{NO}_3)_3 \cdot 5\text{H}_2\text{O}$ and $\text{Na}_2\text{MoO}_4 \cdot 2\text{H}_2\text{O}$ (molar ration of Bi to Na = 1:1) was added dropwise. The reaction mixture was moved into the autoclave and was autoclaved at 160°C for 12 h. Finally, the $\text{NH}_2\text{-MIL-125/Bi}_2\text{MoO}_6$ composites (symbolized as $x\text{-TiM@BiMO}$, x was the molar ratio of $\text{NH}_2\text{-MIL-125}$

MIL-125 to Bi_2MoO_6) were obtained after washing and drying process. The successful construction of $x\text{-TiM@BiMO}$ composites can be proved by X-ray photoelectron spectra (XPS), PXRD, and FTIR results. As shown in Figure 8(b)-(e), the SEM images indicated that TiM had a homogeneous decahedron morphology and the BiMO grew as a thin layer on the surface of TiM. For the cases of 0.65-TiM@BiMO and 0.32-TiM@BiMO composites, the morphology of TiM can be clearly realized. But as the content of BiMO further increased, the decahedron morphology of TiM disappeared. This phenomenon suggested that higher amount of BiMO could cover the surfaces of TiM and overspread its pores, which could block the channels of photon and mass transfer. The UV-vis DRS spectra (Figure 8(f)) showed that the photo-response absorption edges of the TiM@BiMO composites were wider than that of pure TiM and BiMO, respectively. The broadening of absorption ranges from UV to visible light were beneficial to enhance the corresponding photocatalytic performances. Moreover, the 0.32-TiM@BiMO displayed the broadest expansion to visible light, indicating the excess of BiMO might accumulate on the surface of TiM, thus shielding the light absorption of TiM in the composites. Meanwhile, the transient photocurrent responses and EIS Nyquist spectra demonstrated that the separation of photo-generated charges was enhanced via the incorporation of BiMO. Furthermore, the work functions of as-prepared material were measured using scanning Kelvin probe (SKP) procedure, because the lowest energy of the work function can be interpreted as the capacity for charge transfer from the inner to the external of the samples. The TiM, BiMO, and TiM@BiMO were presented as a specimen a, b, and c, respectively in the SKP charts (Figure 8(g)). The work function of TiM@BiMO was observed 4.73 eV, which was lower than pure BiMO (4.95 eV) and TiM (5.10 eV). This result suggested the electron transformation capacities of different photocatalysts followed the order of $\text{TiM@BiMO} > \text{BiMO} > \text{TiM}$. As expected, the photocatalytic degradation efficiencies of extremely toxic trichlorophenol and dichlorophenol over the optimal 0.32-TiM@BiMO were 92.19% and 93.28%, respectively (Figure 8(h)-(i)). And the respective rate constants were almost 17 and 8 times greater than the rates achieved by pure $\text{NH}_2\text{-MIL-125}$. Moreover, the efficiency of oxygen production by 0.32-TiM@BiMO raised to $171.3 \mu\text{mol}\cdot\text{g}^{-1}$, which was 5.1 and 27.1 times greater than that of pure BiMO and TiM (Figure 8(j)). The photocatalytic mechanism of this experimental system was illustrated in Figure 8(k). In summary, since the intimate contact between TiM and BiMO, the mesoporous core-

shell structures of the TiM@BiMO composites favored the charge separation and mass transfer. The transformation between Ti^{3+} and Ti^{4+} , and the generation of h^+ resulted in efficient O_2 production. About chlorophenol degradation, the Ti^{3+} defects, $\cdot\text{OH}$, and h^+ radicals jointly played key roles in opening the chlorophenols benzene rings. This study revealed that the as-prepared $\text{NH}_2\text{-MIL-125/Bi}_2\text{MoO}_6$ core-shell composites exhibited bi-functional photocatalytic property for degradation of organic pollutants and generation of O_2 owing to the presence of Ti-oxo clusters in $\text{NH}_2\text{-MIL-125}$. More importantly, considering that bismuth-based materials are highly likely to block the pores of MOFs, thereby reducing the mass transfer efficiency and accelerating the electron-hole pairs recombination of the composites. Therefore, optimization of pore utilization in MOFs is the key factor to improve the photocatalytic performance of MBCs.

Figure 8. (a) The procedure for the preparation of $\text{NH}_2\text{-MIL-125/Bi}_2\text{MoO}_6$ composites, (b)-(e) SEM images of 0.32-TiM@BiMO, 0.65-TiM@BiMO, 0.97-TiM@BiMO, 1.3-TiM@BiMO, (f) UV-vis DRS spectra of the as-prepared materials, (g) SKP maps of TiM, BiMO, and TiM@BiMO, (h)-(j) the photocatalytic activities for dichlorophen and trichlorophenol degradation and O_2 production over the different samples in visible light, (k) illustration of the photocatalytic mechanism of $\text{NH}_2\text{-MIL-125/Bi}_2\text{MoO}_6$ core-shell composites [144], copyright (2019) Elsevier.

As mentioned above, Bi_2WO_6 is the other Aurivillius-structural bismuth-based compound that has been widely applied in the fields of photocatalysis due to its unique structure and physicochemical property [263, 264]. However, it is desirable to acquire effective charge separation efficiency, extend light absorption range, improve recyclability as well as high surface area for Bi_2WO_6 nanoparticles. In 2020, Li and co-workers [145, 146] fabricated $\text{NH}_2\text{-MIL-125/Bi}_2\text{WO}_6$ composites via the hydrothermal method. These composites demonstrated higher activities for the elimination of RhB and TC. The electron spin resonance (ESR) and radicals quenching experiment analysis exhibited that the $\cdot\text{O}_2^-$ and h^+ were the major active species. The effective transfer of photo-generated charges, intrinsic porous structure and enlarged light absorption range endowed the $\text{NH}_2\text{-MIL-125/Bi}_2\text{WO}_6$ composites with superior photocatalytic performance.

Similar to $\text{NH}_2\text{-UiO-66}$ photocatalysts, fabrication of $\text{NH}_2\text{-MIL-125}$ composites with BiOX ($\text{X} = \text{Cl, Br, I}$) semiconductors has been frequently reported in recent years [148-150]. For instance,

Hu et al. [149] adopted a hydrothermal approach for the development of $\text{NH}_2\text{-MIL-125/BiOCl}$ composites with the different loading amounts of BiOCl (Figure 9(a)). Characterization techniques including PXRD, FTIR, XPS, Raman confirmed the successful formation of $\text{NH}_2\text{-MIL-125/BiOCl}$ composites (denoted as $\text{NM/BOC-}x$, x was the content of $\text{NH}_2\text{-MIL-125}$). The materials' morphologies were examined by TEM and high-resolution TEM (HRTEM). As shown in Figure 9(b), the NM/BOC-10 TEM images demonstrated that nanosheets of BiOCl were firmly stuck on the $\text{NH}_2\text{-MIL-125}$ surface. The NM/BOC-10 HRTEM image depicted in Figure 9(c) presented lattice spacing at 0.275 and 0.344 nm, which can be indexed to the tetragonal phase BiOCl (110) and (001) planes [265]. As displayed in Figure 9(d), it was excellent that the absorption edge of BiOCl was about 380 nm, related to the bandgap of 3.31 eV. Following the deposition of $\text{NH}_2\text{-MIL-125}$, the composites possessed more intense absorption in visible region. The higher absorption allowed $\text{NM/BOC-}x$ composites to take in more visible light and produce more charges participating in the photocatalysis procedure, which might give a higher photocatalytic performance. Furthermore, the EIS Nyquist plots and transient photocurrent responses (Figure 9(e)-(f)) indicated that the introduction of $\text{NH}_2\text{-MIL-125}$ improved the charge separation efficiency in $\text{NM/BOC-}x$ composites. For the photodegradation of organic contaminants, the optimal NM/BOC-10 displayed a higher activity towards TC and BPA than pure BiOCl and $\text{NH}_2\text{-MIL-125}$. Furthermore, the degradation of TC was measured by conducting the TOC analysis (Figure 9(g)). Under irradiation for 2 h, almost 45% of TC was mineralized, implying that TC can be photodegraded by the as-prepared composites under visible light. To find out the accurate photocatalysis mechanism, the radical trapping experiments and ESR techniques were introduced in this study. As shown in Figure 9(h), it can be assumed that $\cdot\text{O}_2^-$ acted as the major active specie in the reaction. Concluding all the findings described above, a prospective photocatalytic mechanism was presented in Figure 9(i). Since the band alignment between $\text{NH}_2\text{-MIL-125}$ and BiOCl was well-matched, therefore, the photo-generated h^+ could be traveled to that of BiOCl from the HOMO of $\text{NH}_2\text{-MIL-125}$. Contrary to this, the photo-generated electrons could be transferred to the Ti^{4+} in the Ti-O cluster of $\text{NH}_2\text{-MIL-125}$ from the CB of BiOCl . Subsequently, the Ti^{4+} was inclined to form Ti^{3+} with the existence of photo-generated electrons. Owing to the strong reducing ability of Ti^{3+} (-1.37 V vs. SHE), the O_2 was reduced to $\cdot\text{O}_2^-$ through the intervalence electron transfer in the Ti-O clusters. Correspondingly, the

Ti³⁺ ions were inclined to oxidize to Ti⁴⁺, leading to the reactions as expressed in Equations (6)-(8). The main finding of this work was to uncover the improved photocatalytic activity was ascribed to the Ti³⁺-Ti⁴⁺ intervalence electron transfer in NH₂-MIL-125 and synergistic effect between BiOCl and NH₂-MIL-125. Moreover, the favorable mineralization capacity of NH₂-MIL-125/BiOCl composite made it a promising photocatalyst in organic pollutants' degradation.

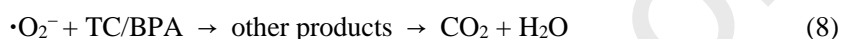
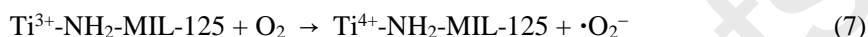
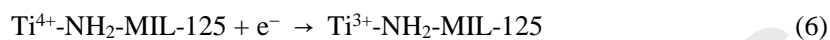


Figure 9. (a) Schematic representation of the synthesis of NH₂-MIL-125/BiOCl composites, (b)-(c) TEM and HRTEM images of NM/BOC-10, (d) UV-vis DRS spectra of the as-prepared materials, (e)-(f) transient photocurrent responses and EIS Nyquist plots of NM/BOC-10, BiOCl, and NH₂-MIL-125, (g) the reduction in TOC during the photodegradation of TC over NM/BOC-10, (h) DMPO- $\cdot\text{O}_2^-$ ESR signals recorded with NM/BOC-10 and BiOCl and, (i) the possible mechanism for the transport of charges in NH₂-MIL-125/BiOCl composite [149], copyright (2018) Elsevier.

Besides Bi₂MoO₆ and BiOX photocatalysts, BiVO₄ is a typical n-type semiconductor, which possesses a small bandgap and has drawn much consideration among researchers due to its good photoconductivity and photosensitivity toward visible light. Therefore, it has been considered as an exceptional photocatalyst to be used in the water splitting and decomposition of the organic pollutants [266-268]. The crystalline structure of BiVO₄ has a significant responsibility in its activity during photocatalysis [266]. The three most prominent crystalline phases of BiVO₄ are tetragonal scheelite (s-t), tetragonal zircon (z-t), and monoclinic scheelite (s-m) structures. The monoclinic scheelite (m-BiVO₄) has a relatively small bandgap (2.34 eV) compared to other phases, so it exhibits enhanced activity than the tetragonal phases [266]. More importantly, m-BiVO₄ has suitable band edges ($E_{\text{CB}} = 0.34$ eV, $E_{\text{VB}} = 2.75$ eV), which can match well with MIL-125 ($E_{\text{HOMO}} = 3.29$ eV, $E_{\text{LUMO}} = 0.88$ eV) to form a binary composite [142]. Recently, Yang et al. [141] firstly reported the MIL-125/BiVO₄ composites with significantly increased photocatalytic activity for RhB degradation and good stability after 5 irradiation cycles. In addition to the MIL-125/BiVO₄

composites, Wang and the co-workers [147] reported various $\text{NH}_2\text{-MIL-125/Bi}_2\text{S}_3$ composites prepared through the solvothermal treatment approach and employed as a bifunctional photocatalyst for the RhB degradation and Cr(VI) reduction under visible light. As a photosensitizer, Bi_2S_3 improved the visible light absorption and narrowed the band gap of $\text{NH}_2\text{-MIL-125/Bi}_2\text{S}_3$ composite to be 2.59 eV. The detailed reaction mechanism analysis suggested that the photo-generated electrons transferred from $\text{NH}_2\text{-MIL-125}$ to Bi_2S_3 through $\text{NH}_2\text{-MIL-125/Bi}_2\text{S}_3$ composite with well-matched band energies, which efficiently suppressed charge recombination and enhanced the final photocatalytic performance.

2.4 MIL-53(Fe)/bismuth-based semiconductor composites

Fe-based MOFs are extremely attractive as iron is an earth-abundant element and the Fe-containing hybrids are frequently used in heterogeneous catalysis [35, 269, 270]. Among them, MIL-53(Fe) is an environment-friendly Fe-based MOF that is composed of the $\text{FeO}_4(\text{OH})_2$ and terephthalic acid linkers. The $\text{Fe}_3\text{-}\mu_3\text{-oxo}$ clusters present in this MOF are responsive to the visible light regions and can harvest the photons more effectively [271]. Moreover, MIL-53(Fe) possesses stronger visible light absorption capacity in the range of 300-500 nm than $\text{NH}_2\text{-MIL-125}$ and UiO-66 [33, 37, 53]. Meanwhile, the valence alternation of the metal sites endows this MOF with the catalytic activities like activation of persulfate (PS) or hydrogen peroxide (H_2O_2) for $\text{SO}_4^{\bullet-}$ and $\cdot\text{OH}$ production [272-274], which significantly improve the catalytic activities. The MIL-53(Fe) generally requires fabricating with other efficient materials for enhancing its photocatalytic activity because of its instability in water and rapid recombination of photo-generated charge carriers. In this section, some composites constructed from MIL-53(Fe) and bismuth-based photocatalysts will be discussed [40, 151-153, 156].

Tang and co-workers [151] proposed a coprecipitation approach to construct MIL-53(Fe)/BiOBr hybrid photocatalysts (BM- x , x represented the MIL-53(Fe) contents (wt%) in the composites) to strengthen the photocatalytic capability against the degradation of CBZ and RhB. As demonstrated in Figure 10(a)-(b), MIL-53(Fe) possessed an irregular rod-like morphology and BiOBr exhibited a smooth surface with the 2D lamellar structure. The TEM image of BM-20 (Figure 10(c)) showed that the ultra-tiny particles of MIL-53(Fe) were uniformly emerged on the surface of BiOBr nanosheets. As displayed in Figure 10(d), the pure BiOBr was mainly responsive to UV light.

While the MIL-53(Fe) was responsive to much wider regions ranging from 200 to 600 nm, mainly concentrated on the visible region. Moreover, the E_g of BM-20, BiOBr, and MIL-53(Fe) was measured to be 2.64, 2.75, and 1.92 eV, respectively. The narrow bandgap of BM-20 indicated it was reliable to harvest the visible light and to show enhanced photocatalytic performance. As expected, all of BM-*x* composites exhibited better photocatalytic activities towards RhB and CBZ degradation under visible light irradiation than the pure BiOBr and MIL-53(Fe), and the photocatalytic activity of BM-20 was the most efficient. To assess the higher activity of BM-20, the Nyquist impedance plots, transient photocurrent curves and PL spectra were measured (Figure 10(e)-(g)). The results indicated that it was useful to employ BM-20 as the photocatalyst for effective separation of photo-generated charge carriers. By analyzing the electrochemical data, the CB potential (E_{CB}) of BM-20 was 0.11 eV vs. NHE. And using the equation ($E_{VB} = E_g + E_{CB}$), the VB potential (E_{VB}) of BM-20 was calculated 2.75 eV vs. NHE, which was much positive than the redox potential of $\cdot\text{OH}/\text{OH}^-$ (+2.38 eV vs. NHE) [275]. Therefore, the BM-20 can convert OH^- into $\cdot\text{OH}$, but $\cdot\text{O}_2^-$ cannot be generated during the photocatalytic process because of the potentials of $\text{O}_2/\cdot\text{O}_2^-$ (-0.33 eV vs. NHE) was more negative than the E_{CB} of BM-20 [275]. The active-specie-trapping experiments showed that the CBZ degradation was inhibited remarkably as the triethanolamine (TEOA) and isopropanol (IPA) were introduced. This phenomenon confirmed the main active species were $\cdot\text{OH}$ and h^+ . Furthermore, the addition of $\text{K}_2\text{Cr}_2\text{O}_7$ suppressed the decomposition of CBZ to some extent, indicating that electrons in the conduction band of BM-20 had a key role in the process of photocatalysis (Figure 10(h)). This study revealed that the incorporation of MIL-53(Fe) can not only accelerate the separation of photo-generated charge carriers, but also effectually boost the light absorption of the MBCs.

Figure 10. SEM and TEM images of (a) MIL-53(Fe), (b) BiOBr, (c) HRTEM images of the BM-20, (d) UV-vis DRS spectra of MIL-53(Fe), BiOBr and BM-*x* composites, (e)-(g) Nyquist impedance plots, transient photocurrent responses, PL spectra of the as-prepared materials and (h) schematic representation of the CBZ degradation over the BM-20 [151], copyright (2019) Elsevier.

When MOFs and bismuth-based semiconductors possess suitable band energy levels, an ideal composite might be fabricated due to an intimate contact interface can be formed after both

components were combined. For most of Type I or Type II heterojunctions, owing to their potential difference, the photo-generated charges are inclined to migrate into CB or VB of the attached component. Nevertheless, both the oxidizability of holes and reducibility of electrons are weaker after charges migration [276-278]. In order to prevent the photo-generated charges from recombination and to maintain the effective redox ability of remaining holes and electrons, a Z-scheme MIL-53(Fe)/ α -Bi₂O₃/g-C₃N₄ composite was synthesized by Cui and co-workers [156]. Among these three components, g-C₃N₄ has drawn greater scientific attention in the area of photocatalysis due to a metal-free visible-light-driven (VLD) semiconductor [279]. However, the pure g-C₃N₄ generally shows low activity due to the fast recombination of photo-generated charges. α -Bi₂O₃ has also been often studied owing to its environmental-friendly and thermal stability features [280]. The α -Bi₂O₃ possesses less positive CB and almost similar to the VB of g-C₃N₄, so α -Bi₂O₃ can be used to couple with g-C₃N₄ to develop a Z-scheme composite. Moreover, MIL-53(Fe) as porous materials could provide more channels for the transfer of photo-generated charge carriers and degradation products, thus enhancing the photocatalytic performance.

For the preparation steps of the composites, the pure g-C₃N₄ powder was firstly synthesized by calcination with dicyandiamide as a precursor. Then the α -Bi₂O₃/g-C₃N₄ composite was prepared through the hydrothermal treatment approach. Thirdly, a specific amount of MIL-53(Fe) powders synthesized by a solvothermal treatment approach were added to the α -Bi₂O₃/g-C₃N₄ mixture for stirring vigorously under 60°C. After evaporating the organic solvent, the final orange powder was MIL-53(Fe)/ α -Bi₂O₃/g-C₃N₄ ternary composite. The mass fractions of MIL-53(Fe) in these composites were taken 10%, 25%, 32%, and 40%, and the respective composites were denoted as 10%-MBC, 25%-MBC, 32%-MBC, and 40%-MBC, respectively. The 32%-MBC TEM image in Figure 11(a) suggested that both g-C₃N₄ and the MIL-53(Fe) were closely attached to the α -Bi₂O₃, demonstrating the intimate interaction between MIL-53(Fe), g-C₃N₄, and α -Bi₂O₃. After the embedding of MIL-53(Fe), the pore volume and surface area of ternary composites were greater than binary composites (Figure 11(b)). Usually, the larger surface area not only can afford more active sites for adsorption of pollutants but also enhance the migration of photo-generated charges [37, 281]. Furthermore, as shown in Figure 11(c), the enhanced visible light absorption and redshift were observed among the ternary materials, which was ascribed to the incorporation of MIL-53(Fe)

and the strong interactions among the three components. The Mott-Schottky plots, EIS Nyquist curves, and photo-current response tests were conducted to measure the capability of the charge transfer of the MIL-53(Fe)/ α -Bi₂O₃/g-C₃N₄ composites. As illustrated in Figure 11(d)-(e), 32%-MBC material showed the most intense photocurrent response and the smallest circle on the EIS Nyquist plots. The obtained results revealed that the smallest charge transfer resistance existed in the 32%-MBC composite, concluding that it had the highest photo-generated charges separation efficiency. Previous studies had demonstrated that the charge density was inversely proportional to the slope of the Mott-Schottky plot [282, 283]. Obviously, 32%-MBC showed larger charge carrier density compared to MIL-53(Fe) and α -Bi₂O₃/g-C₃N₄ owing to its smaller slope (Figure 11(f)). Moreover, the positive shift of fermi level would be occurred with increasing charge carrier density, resulting in band bending at the surface of the composite, and this phenomenon would further promote the charges separation and migration [284]. This phenomenon was consistent with the results of transient photocurrent and EIS Nyquist measurement. In this work, amido black 10B dye was selected as the modeling pollutant. As displayed in Figure 11(g), MIL-53(Fe)/ α -Bi₂O₃/g-C₃N₄ composites showed much better photocatalytic performance than that of pure g-C₃N₄, α -Bi₂O₃, MIL-53(Fe) and binary composites under same experimental condition. Among them, 32%-MBC showed the optimal degradation efficiency, in which 100% of amido black 10B could be eliminated within 45 min. The reactive species trapping experiments suggested that both the h⁺ and •O₂⁻ were the main active species in the photocatalytic process, while •OH played a relatively small role. Combing with the above results and the band positions of the three components, the photocatalytic mechanism can be summarized as follows (Figure 11(h)). The photo-generated electrons in the CB of α -Bi₂O₃ would rapidly be captured by the h⁺ generated from the VB of g-C₃N₄ and MIL-53(Fe). Therefore, the remained h⁺ retained in the VB of α -Bi₂O₃ might participate in degrading the amido black 10B. Meanwhile, since the CB and LUMO of g-C₃N₄ (-1.13 eV vs. NHE) and MIL-53(Fe) (-0.47 eV vs. NHE) were more negative than O₂/•O₂⁻ reduction potential, thereby the photo-generated electrons gathered in CB of g-C₃N₄ and LUMO of MIL-53(Fe) could react with O₂ to produce •O₂⁻, which was beneficial to decompose the amido black 10B. In summary, this work was novel because the authors firstly reported that the dual Z-scheme MIL-53(Fe)/ α -Bi₂O₃/g-C₃N₄ ternary composites can be fabricated via a facile precipitation method, which provided a feasible strategy to prepare

ternary composites containing MOFs and bismuth-based semiconductors for photocatalytic applications.

Figure 11. (a) TEM image of 32%-MBC, (b) N_2 adsorption-desorption isotherms of MIL-53(Fe), α - Bi_2O_3 /g- C_3N_4 and x -MBC composites, (c) UV-vis DRS spectra of g- C_3N_4 , α - Bi_2O_3 , MIL-53(Fe) and x -MBC composites, (d)-(e) transient photocurrent curves and EIS plots of g- C_3N_4 , α - Bi_2O_3 , MIL-53(Fe), α - Bi_2O_3 /g- C_3N_4 and 32%-MBC, (f) Mott-Schottky plots of MIL-53(Fe), α - Bi_2O_3 /g- C_3N_4 , 32%-MBC composite, (g) degradation of amido black 10B over different materials and (h) photocatalytic activity of MIL-53(Fe)/ α - Bi_2O_3 /g- C_3N_4 in visible light [156], copyright (2020) Elsevier.

2.5 MIL-88(Fe)/bismuth-based semiconductor composites

The MIL-88(Fe) series are a type of economical, biodegradable, and biocompatible Fe(III)-dicarboxylate MOFs. They are composed of various types of organic dicarboxylate linkers and oxo-centered trimers of metal octahedra. The organic linkers in MIL-88A(Fe), MIL-88B(Fe), MIL-88C(Fe), and MIL-88D(Fe) refer to fumaric acid, terephthalic acid, 2,6-naphthalene dicarboxylic acid and 4,4'-biphenyl dicarboxylic acid, respectively [285, 286]. Among the above four materials, MIL-88A(Fe) and MIL-88B(Fe) possess narrow bandgaps of 2.60 and 2.39 eV as well as strong thermal stabilities, which make them very suitable for photocatalytic applications [287, 288]. However, the MIL-88(Fe) applications in photocatalysis limited severely due to its low conversion of solar energy and rapid recombination of the photo-generated charge carriers when compared to other inorganic semiconductors [37, 281, 289]. Up to now, a number of MIL-88(Fe)-based composites have been reported to advance the photocatalytic applications, such as MIL-88A(Fe)/graphene oxide [275], MIL-88A(Fe)/g- C_3N_4 [290], MIL-88A(Fe)/CdLa₂S₄ [291], MIL-88B(Fe)/Fe₃O₄ [292], MIL-88B(Fe)/Ti₃C₂ [293], MIL-88A/PANI [41], etc. Furthermore, some MIL-88(Fe)/bismuth-based semiconductor composites were made-up to accomplish prominent photocatalytic activities against the degradation of organic pollutants [123, 157-161].

Recently, it has been established by some researchers that developing surface oxygen vacancies (OVs) could lead to the suppression of the bulk charge carriers recombination [294-296]. Zhao and co-workers [123] introduced the Bi₂MoO₆ (BM) modified by surface OVs into MIL-88B(Fe)

through a facile two steps solvothermal method, which exhibited superior separation efficiency of the photo-generated charges at the interface and bulk simultaneously. For the preparation of the binary composites, the pure MIL-88B(Fe) and BM with OV_s (BMO) were firstly synthesized by solvothermal treatments according to the previous reports [294, 297]. Secondly, a certain amount of BMO (0.1, 0.2, 0.3, 0.4, 0.5 g) was used to prepare a mixture with the MIL-88B(Fe) precursors. After the solvothermal treatment of the above mixtures, the obtained powders were Bi₂MoO₆/MIL-88B(Fe) composites, which named X-BMO/M88 (X represented the weight in unit of 0.1 mg, X = 1, 2, 3, 4 and 5). As illustrated in Figure 12(a)-(b), pure BM looked like a flower-shaped microsphere with almost 2 μ m diameter, but the BMO sample showed small asymmetrical smooth-surfaced nanoparticles. This phenomenon indicated that the OV_s were produced on the surface of Bi₂MoO₆. It should be noted that the small-sized Bi₂MoO₆ particles are useful to decrease the distance for photo-generated charges from the crystal to surface, resulting in inhibition of charge recombination. After embedding the BMO, the 3-BMO/M88 surface was intimately deposited with 20 nm-sized BMO nanosheets (Figure 12(c)-(d)). ESR and XPS analysis were performed to deeply investigate the development of OV_s defects in BMO. As shown in Figure 12(e), the characteristic peak at 532.0 eV with a relative area (almost 31.69%) was ascribed to the OV_s in BMO. As to ESR analysis, a prominent signal was detected at the $g = 2.004$ for BMO (Figure 12(f)), which was attributed to the electrons captured by OV_s [298, 299]. It was noteworthy that the OV_s defects in BMO/M88 composites played an important role in the light-harvesting process. As displayed in Figure 12(g), after the development of OV_s on the surface of the BMO, an obvious enrichment was observed in absorption of visible light ranging from 420 to 800 nm. The E_g values of 3-BMO/M88, BMO, BM, and M88 were calculated to be 2.22, 2.71, 2.80, and 2.39 eV, respectively. This result should be attributed to the synergistic effect between the surface OV_s on Bi₂MoO₆ and MIL-88B(Fe). Moreover, the time-resolved fluorescence decay spectra were used to explore the dynamic behavior of charge migration in the various X-BMO/M88 materials (Figure 12(h)). The average fluorescence lifetime calculated for 3-BMO/M88 was found to be 4.60 ns. The prolonged lifetime demonstrated that several contact interfaces and abundant nanochannels were developed in the BMO/M88 composites for the rapid transfer of the charge carriers. The optimal 3-BMO/M88 demonstrated that 99.5% of RhB can be decomposed within 120 min upon irradiation with visible light and 100% of

BPA molecules were removed with the addition of 10 mM H_2O_2 . These results showed that the surface OV's and formed heterostructure were promising to increase the photo-Fenton-like reactions. Based on the energy band structures of MIL-88B(Fe) and BMO and trapping experiment results, the superior 3-BMO/M88 photocatalytic activity was assigned to the formed built-in electric field at the interface of type II heterojunction, which effectively separated the photo-generated charges. Moreover, the greater content of OV's was believed to be trapping sites to prevent electron-hole pairs recombination (Figure 12(i)). This study revealed the importance of introducing OV's in the MBCs. On the one hand, the presence of OV's could notably widen the light adsorption range. On the other hand, the large amounts of OV's are considered to be electron-trapping centers to inhibit the photo-generated electron-hole pairs recombination. In the future, fabrication of MBCs with abundant OV's was worth trying to enhance the separation and migration of charges in the bulk and interface phases.

Figure 12. SEM images of (a) BM and (b) BMO, TEM images (c)-(d) of the sample of as-prepared 3-BMO/M88, (e) XPS O 1s spectra and (f) ESR spectra of BMO and BM samples, (g) diffuse reflectance UV-vis spectra and (h) time-resolved fluorescence decay curves of M88, BM, 3-BMO/M88 and BMO samples and (i) the mechanism of 3-BMO/M88 for photocatalytic degradation in visible light [123], copyright (2020) Elsevier.

Recently, S.G. Khasevani and M.R. Gholami fabricated some binary, ternary and quaternary MIL-88(Fe)/bismuth-based semiconductor composites including MIL-88A(Fe)/BiOI [157], MIL-88A(Fe)/BiOI/g- C_3N_4 [158], MIL-88B(Fe)/BiOI/ ZnFe_2O_4 [160] and MIL-88B(Fe)/ $\text{Ag}_3\text{PO}_4/\text{BiPO}_4/\text{g-}\text{C}_3\text{N}_4$ composites [161]. All the above composites exhibited superior photocatalytic activities to accomplish efficient organic pollutants degradation upon the irradiation of visible light, such as MB, AB92, RhB, and colorless phenol. The greatly improved photocatalytic performances were attributed to the substantial harvesting of visible light and inhibition of charges recombination through introducing MIL-88(Fe) in the corresponding composites.

2.6 MIL-100(Fe)/bismuth-based semiconductor composites

MIL-100(Fe) was also known as a Fe-based MOF that is composed of benzene-1,3,5-tricarboxylic acid and Fe-O octahedra clusters. And it was firstly synthesized by Horcajada and co-workers in 2007 [300]. It possesses a definite zeotype crystal structure comprising of 2.9 and 2.5

nm mesoporous cages accessible through window sizes of approximately 0.86 and 0.55 nm, respectively [301, 302]. Owing to the high chemical, photo, thermal and water stability and especially narrow bandgap ($E_g = 1.82$ eV) [33], MIL-100(Fe) has been considered as a typical MOF for photocatalysis applications under visible light. As mentioned above, iron element has numerous advantages over other metals, such as environmental-friendly, low toxicity and economical in cost [303]. However, the poor conductivity of MIL-100(Fe) significantly limits its potential applications. Up to now, a number of MIL-100(Fe)-based composites have been fabricated with the semiconductor photocatalysts like TiO_2 [304], ZnO [305], Fe_3O_4 [306] and $\text{g-C}_3\text{N}_4$ [51] and even polymer conductor like PANI [48] to advance its photocatalytic applications. In this section, some MIL-100(Fe)/bismuth-based semiconductor composites were introduced in detail [162-165].

Han and co-workers [162] synthesized a series of MIL-100(Fe)/ BiVO_4 composites following a mild hydrothermal approach to decorate the surface of decahedron BiVO_4 with the MIL-100(Fe) nanoparticles. More importantly, the MIL-100(Cr)/ BiVO_4 composite was adopted as a referential photocatalyst in this study, as the chromium carboxylate MIL-100(Cr) was isomorphic with the MIL-100(Fe). Thus, the respective photocatalytic reaction can be examined by targeting a particular variable. As shown in Figure 13(a), no characteristic PXRD diffraction peaks for MIL-100(Fe) were observed in the as-prepared composite, which can be ascribed to the high dispersal of MIL-100(Fe) particles on the surface of BiVO_4 nanoparticles. Being compared with the UV-vis DRS spectrum of pristine BiVO_4 , the as-prepared composite (MIL-100(Fe)/ BiVO_4) demonstrated an extensive and broad absorption in the visible region from 500 to 800 nm [307, 308]. A redshift was observed in absorption after coating the BiVO_4 with MOFs, indicating that the visible light response was significantly enhanced (Figure 13(b)). From the SEM micrographs of the as-obtained materials (Figure 13(c)-(d)), the pristine BiVO_4 nanoparticles displayed decahedron structure with a smooth surface. Furthermore, the deposition of nanoparticles of MIL-100(Fe) on the BiVO_4 surface resulted in a rough surface of the MIL-100(Fe)/ BiVO_4 . The XPS analysis showed that with the deposition of ultra-tiny particles of MIL-100(Fe), a decline in binding energies of V 2p and Bi 4f occurred, which confirmed strong affinity between BiVO_4 and MIL-100(Fe). The photocatalytic O_2 production activities over the as-prepared materials were tested under a 420 nm LED lamp using NaIO_3 as an electron sacrificial agent. The optimal photocatalyst 8%-MIL-100(Fe)/ BiVO_4 exhibited

superior activity for O_2 production (almost $333.3 \mu\text{mol}\cdot\text{h}^{-1}\cdot\text{g}^{-1}$), which was 4.3 times higher than that of the pure BiVO_4 ($77.3 \mu\text{mol}\cdot\text{h}^{-1}\cdot\text{g}^{-1}$). While the $\text{MIL-100}(\text{Cr})/\text{BiVO}_4$ sample was almost inactive under the same experimental conditions. For the purpose of understanding the improved photocatalytic activity of $\text{MIL-100}(\text{Fe})/\text{BiVO}_4$, various photo-electrochemical characterizations were carried out. Figure 13(e) depicted that the PL intensity of as-prepared $\text{MIL-100}(\text{Fe})/\text{BiVO}_4$ was significantly dropped down compared with the pure BiVO_4 , while it remained almost the same PL intensity over the $\text{MIL-100}(\text{Cr})/\text{BiVO}_4$ composite, signifying that only $\text{MIL-100}(\text{Fe})$ deposition can effectively promote the separation and migration of photo-generated electron-hole pairs. EIS Nyquist plots exhibited that the resistance semicircle of $\text{MIL-100}(\text{Fe})/\text{BiVO}_4$ was quite smaller than $\text{MIL-100}(\text{Cr})/\text{BiVO}_4$ and BiVO_4 (Figure 13(f)), manifesting the intimate interface between $\text{MIL-100}(\text{Fe})$ and BiVO_4 resulted in drooping the charge-transfer resistance, which was beneficial to inhibit the recombination of charge carriers. Similarly, the transient photocurrent response spectra also suggested that the as-prepared $\text{MIL-100}(\text{Fe})/\text{BiVO}_4$ composites can successfully enhance the separation efficiency of photo-generated charges for the water oxidation (Figure 13(g)). However, the transient photocurrent response intensity of $\text{MIL-100}(\text{Cr})/\text{BiVO}_4$ was almost identical with BiVO_4 . Considering the mismatch of bandgaps between $\text{MIL-100}(\text{Cr})$ and BiVO_4 , the photo-generated charges in $\text{MIL-100}(\text{Cr})/\text{BiVO}_4$ cannot be transported effectually, leading to no significant change in the photocurrent densities (Figure 13(h)). This phenomenon indicated that embedding of different MOFs had a significant impact on the charge carriers transfer in the different composites. Based on the band edge positions of BiVO_4 , $\text{MIL-100}(\text{Fe})$ and $\text{MIL-100}(\text{Cr})$, the proposed photocatalytic mechanisms were illustrated in Figure 13(i)-(j). When irradiated with visible light, the electrons moved to the CB of BiVO_4 from the HOMO of $\text{MIL-100}(\text{Fe})$ by intimate interfaces, which were inclined to react with IO_3^- to produce I^- . Meanwhile, the holes would move to the LUMO of $\text{MIL-100}(\text{Fe})$ from the VB of BiVO_4 and reacted with H_2O molecules to produce O_2 . As to the $\text{MIL-100}(\text{Cr})/\text{BiVO}_4$ composite, water oxidation process cannot occur owing to the band positions' mismatch of $\text{MIL-100}(\text{Cr})$ and BiVO_4 . In general, this study provided an instructive strategy for the controllable fabrication of MBCs by loading MOFs on the bismuth-based semiconductors. Furthermore, it demonstrated that the energy band's matching degree of MOFs and bismuth-based semiconductors is crucial for the photocatalytic activity achieved by MBCs.

Figure 13. (a) PXRD patterns of BiVO₄ nanoparticles and composite based on MIL-100(Fe)/BiVO₄, (b) UV-vis DRS of MIL-100(Cr), MIL-100(Fe), MIL-100(Cr)/BiVO₄, BiVO₄ and MIL-100(Fe)/BiVO₄ composites, (c)-(d) SEM images for the morphological analysis of MIL-100(Fe)/BiVO₄ and BiVO₄, (e) PL spectra, (f) EIS measurements and (g)-(h) transient photocurrent response of BiVO₄, MIL-100(Fe)/BiVO₄ and MIL-100(Cr)/BiVO₄ composites, (i)-(j) the proposed mechanism for photocatalytic production of O₂ over MIL-100(Fe)/BiVO₄ and MIL-100(Cr)/BiVO₄ composites when irradiated with visible light [162], copyright (2020) American Chemical Society.

In addition to the above-stated case, Zheng et al. [164] and Yang et al. [165] synthesized Bi₂WO₆/MIL-100(Fe) and Bi₂MoO₆/MIL-100(Fe) composites via the simple hydrothermal-coprecipitation method. Briefly, MIL-100(Fe) was firstly prepared following a facile hydrothermal treatment approach. Subsequently, different content of MIL-100(Fe) was mixed with the solution containing Bi₂MoO₆ or Bi₂WO₆ precursors. Then the mixture was heated at pre-set temperature (100-160°C) for 12 h to get the final products. In the corresponding composites, the MIL-100(Fe) acted as a substrate, the Bi₂WO₆ or Bi₂MoO₆ nanoparticles uniformly covered on the surface of MIL-100(Fe). In these two studies, salicylic acid and RhB were chosen as the modeling pollutants, the as-prepared composites showed much higher activities against the photocatalytic degradation than pure Bi₂MO₆ (M = Mo and W) and MIL-100(Fe) under visible light. Moreover, the two kinds of composites displayed exceptional photostability in the recycling experiments, indicating their suitability for actual applications. The higher photocatalytic performances were mainly linked to the strong interfacial interaction amid MIL-100(Fe) and Bi₂MO₆, thus, in turn, enabling the separation and migration of photo-generated charge carriers.

2.7 HKUST-1/bismuth-based semiconductor composites

HKUST-1, also known as [Cu₃(BTC)₂(H₂O)₃]_n (BTC = benzene-1,3,5-tricarboxylic acid), is a representative MOF having the strong stability and large surface area (BET and Langmuir surface areas are 1154 and 1958 m²·g⁻¹ respectively) [309]. Such intrinsic merits make HKUST-1 a promising candidate to be used in the gas storage/separation [310-312], molecular adsorption [313, 314], drug delivery [315, 316] and catalysis [317, 318]. But the photocatalytic applications of HKUST-1 are severely limited by its large bandgap (greater than 3 eV), meaning that HKUST-1 can

merely harvest UV light [113]. Therefore, the photocatalytic activity of pristine HKUST-1 can be upgraded for visible light by assembling with narrow bandgap semiconductors. Up to now, different types of HKUST-1/bismuth-based semiconductor composites had been constructed and exhibited superior performances in their corresponding photocatalytic systems [167-170]. In this section, some typical HKUST-1/bismuth-based semiconductor composites prepared by different synthesis methods were highlighted.

Bi_2O_3 is a narrow bandgap semiconductor (approximately 2.6-2.8 eV) [319], which exhibits p-type behavior and good visible light photocatalytic properties [320-322]. However, its practical applications are hampered by the fabrication of monodisperse Bi_2O_3 nanoparticles (NPs) with specific defined-diameters. Ravelli and co-workers [323] suggested that charge carriers of semiconductors start to behave quantum mechanically and exhibited larger redox potential when its crystallite dimension falls below a critical radius about 10 nm. Hence the utilization of quantum-sized Bi_2O_3 NPs (especially 1-3 nm) might lead to enhance photocatalytic efficiency owing to the rate-limiting step should be deemed as the charge transfer rate. Considering that the size distributions of NPs prepared by conventional methods are rather broad [167], thus the development of a new synthesis method is urgently required, which might allow the production of Bi_2O_3 with smaller size distributions and better dispersion. During the last ten years, since the pore-wall of the MOFs can be utilized to control the NPs size and to provide larger encapsulation capacity for guest molecules, various research studies have been focused on the utilization of MOFs for the encapsulation of compounds with impressive catalytic activities, such as Pt [324], Pd [325], Au [326], Ag [327], etc.

In 2016, Guo and co-workers [167] fabricated a recyclable HKUST-1/ Bi_2O_3 composite thin film via liquid-phase epitaxy (LPE) method, considering that LPE method is more attractive towards layer-by-layer MOFs deposition in a controlled manner, and the highly oriented homogenous crystalline MOFs films can be manufactured with thickness ranging from the nanometer to micrometer levels [328, 329]. In this study, the preparation process of HKUST-1/ Bi_2O_3 composites was mainly divided into the following three steps (Figure 14(a)). Firstly, the self-assembled monolayer consisted of 16-mercaptohexadecanoic acid was deposited on the surface of the modified Au substrate, and the fabrication of HKUST-1 was performed with the help of spray system as

illustrated in Figure 14(b). Secondly, they injected the ethanolic solution of triphenyl bismuth (BiPh_3) (freshly prepared) into the reaction vessel containing HKUST-1, then the prepared suspension was allowed to heat at 65°C for 36 h. It was worthy to note that the BiPh_3 loading into the HKUST-1 was quantitatively examined via quartz crystal microbalance (QCM), which revealed that per HKUST-1 cell was capable to load 2-3 molecules of BiPh_3 . Thirdly, the HKUST-1/ BiPh_3 samples were irradiated with 255 nm for several hours to generate HKUST-1/ Bi_2O_3 composites, because of the photodecomposition of BiPh_3 in solution with the existence of O_2 is inclined to form Bi_2O_3 NPs [330]. Figure 14(c) exhibited the PXRD data, which suggested that loading the guest molecules (BiPh_3 and Bi_2O_3) did not influence the crystallinity of HKUST-1. But it was associated to change the ratio of peak intensities, for instance, the ratio of out-of-plane data (002)/(004) decreased from 2.13 for the pristine film to 0.79 for the BiPh_3 loaded film. Increase of immersion time did not change the relative PXRD peak intensities, confirming that guest molecules were loaded in every pore of HKUST-1. Furthermore, the precise position of HKUST-1 lattice occupied by BiPh_3 molecules was investigated using force-field based simulations. The good agreement between the simulated PXRD and experimental PXRD patterns further demonstrated that 3 BiPh_3 molecules per HKUST-1 cell, which was consistent with the QCM analysis (Figure 14(d)). The high-angle annular dark-field scanning transmission electron microscope (HAADF-STEM) micrograph shown in Figure 14(e) revealed the uniform distribution of small size (1-3 nm) Bi_2O_3 NPs into the HKUST-1. The selected area electron diffraction (SAED) micrograph (Figure 14(f)) indicated that the HKUST-1/ Bi_2O_3 composites were grown on quartz glass facing the (111) orientation. Except for the above characterization results, the BiO^+ , Bi_2O_2^+ , Bi_3O_4^+ , Bi_2O^+ species were detected by time of flight secondary ion mass spectrometry (ToF-SIMS), also indicating the successful fabrication of HKUST-1/ Bi_2O_3 composites. The dark adsorption experiments were conducted prior to the photocatalytic process. The results indicated that only 3.2%, 2.6%, and 0.7% of NFR dyes were adsorbed by HKUST-1, HKUST-1/ Bi_2O_3 , and Bi_2O_3 NPs, respectively, suggesting the diffusion of NFR into the HKUST-1 was significantly unaffected by the loading of Bi_2O_3 NPs. Moreover, the as-prepared HKUST-1/ Bi_2O_3 thin-film displayed remarkable photocatalytic activity towards NFR degradation under UV light (255 nm) irradiation, 100% of NFR molecules can be removed within 5 hours (Figure 14(g)). Additionally, as illustrated in Figure 14(h), the HKUST-1/ Bi_2O_3 thin film

was stable and recycled, the corresponding photocatalytic efficiencies maintained well after a four-runs cyclic experiment. This study reported a novel procedure to fabricate MBCs thin films, which can be easily separated and recycled without no significant loss. Such advantages exhibit an attractive prospect for water purification. Moreover, this work confirmed that MOFs can provide a platform for encapsulation of quantum-sized bismuth-based nanoparticles, which could prominently accelerate the transfer of photo-generated charge carriers.

Figure 14. (a) Synthesis scheme of the HKUST-1/Bi₂O₃ composite thin films, (b) schematic diagram for the automatic growth of thin films of HKUST-1 on Au substrates by LPE method, (c) experimental XRD patterns of the HKUST-1 thin film (black line), BiPh₃ loaded (red line) and after UV light irradiation (blue line), (d) simulation XRD patterns of HKUST-1 and 3 BiPh₃ loaded sample, (e)-(f) HAADF-STEM and SAED micrographs of the HKUST-1/Bi₂O₃ materials, (g) photocatalytic processes under different experimental conditions, (h) four repeated experiments of using the HKUST-1/Bi₂O₃ photocatalyst for degradation of NFR under UV light irradiation [167, 329], copyright (2016) Royal Society of Chemistry and (2011) American Chemical Society.

The coupling of different types of advanced oxidation technologies (AOTs) can effectively promote the degradation and mineralization capacities of organic contaminants [331-333]. Among them, a good choice to degrade organic compounds is to use a sonophoto-degradation method, which is a combination of sonolysis and photocatalysis [334]. In 2016, Mosleh's research group successfully fabricated HKUST-1/Ag₃PO₄/Bi₂S₃ [170], HKUST-1/BiVO₄ [168] and HKUST-1/BiPO₄/Bi₂S₃ [169] composites via ultrasound-assisted hydrothermal method. Photocatalytic degradation of binary dyes (such as binary mixture of TB/VS, DB/RB, and TB/AO) were intensified by applying the prepared photocatalyst in a continuous flow-loop reactor equipped with blue LED light. As illustrated in Figure 15(a), liquid circulation in the sonophotocatalytic reactor could strengthen the turbulence of the reaction system, which resulted in an increase in mass transfer by enhancing the contact between photocatalyst and target pollutants. Moreover, circulation enhanced the dispersion of dissolved oxygen (DO) in the aqueous solution, thus increasing the production of free radicals. Taking the HKUST-1/Ag₃PO₄/Bi₂S₃ reaction system as an example [170], the SEM micrographs of HKUST-1 (Figure 15(b)) and HKUST-1/Ag₃PO₄/Bi₂S₃ (Figure 15(c)) exhibited the

size of octahedral HKUST-1 was about 1.5 μm and indicated that the nanowires of $\text{Ag}_3\text{PO}_4/\text{Bi}_2\text{S}_3$ binary component uniformly covered on the surface of HKUST-1. Furthermore, it can be observed that HKUST-1/ $\text{Ag}_3\text{PO}_4/\text{Bi}_2\text{S}_3$ composite exhibited quite weak PL emission intensity as compared to pristine HKUST-1 (Figure 15(d)), suggesting that the combination of HKUST-1 and $\text{Ag}_3\text{PO}_4/\text{Bi}_2\text{S}_3$ was considerably useful for the separation of photo-generated charge carriers. More importantly, combination of central composite design (CCD) with desirability function (DF) were used for the optimization of operational parameters (i.e. flow rate, initial TB and VS concentration, sonication and irradiation time, initial pH and dosage of photocatalyst) (Figure 15(e)-(h)). The results revealed that 98.44% and 99.36% of TB and VS can be sonophotodegraded under the optimal experimental condition (dye = 25 $\text{mg}\cdot\text{L}^{-1}$, sonication, and irradiation time of 25 min, solution flow rate of 70 $\text{mL}\cdot\text{min}^{-1}$, 0.25 $\text{g}\cdot\text{L}^{-1}$ dosage of photocatalyst and pH = 6.0). Additionally, the synergetic index was obtained as 2.53, indicating that the coupling of ultrasound and photocatalysis can contribute to higher catalytic efficiency compared with the individual process.

Figure 15. (a) Schematic diagram of sonophotocatalytic reactor set-up, (b)-(c) SEM micrographs of HKUST-1 and HKUST-1/ $\text{Ag}_3\text{PO}_4/\text{Bi}_2\text{S}_3$ composite, (d) PL spectra of HKUST-1 and HKUST-1/ $\text{Ag}_3\text{PO}_4/\text{Bi}_2\text{S}_3$ composite, (e)-(g) 3D plots of response surface graphs of dye concentration, flow rate, pH and reaction time on the catalytic efficiency (h) profiles for desirability function and predicated values for sonophotocatalytic degradation, lines shown with red dashes represent optimal values [170], copyright (2016) Elsevier.

2.8 Other MBCs

In general, most of the studies focused on the preparation of binary or ternary composites based on the above-mentioned MOFs (UiO-66/ NH_2 -UiO-66, ZIF-8, MIL-125/ NH_2 -MIL-125, MIL-88(Fe), MIL-100(Fe), MIL-53(Fe) and HKUST-1) because of their good stability and recyclability. These MOFs-based photocatalysts are highly capable to maintain its catalytic activity and crystallinity for at least three cycles in the weakly acidic and basic environments. Except the above seven types of MOFs, some other stable MBCs for photocatalysis are also present, such as BUC-21/ $\text{Bi}_{24}\text{O}_{31}\text{Br}_{10}$ [44], $\text{CuWO}_4/\text{Bi}_2\text{S}_3/\text{ZIF-67}$ [121], MIL-101(Cr)/ BiVO_4 [172], MIL-101(Cr)/ $\text{Bi}_{25}\text{FeO}_{40}$ /polythiophene [103], MOF-5/ BiOBr [171] and Co/Ni-MOF/ BiFeO_3 [173].

BUC-21 is a newly synthesized Zn-based 2D MOFs, which was firstly reported by our research group in 2017 [335]. It has been proved to possess the good capability for reduction of Cr(VI) and decomposition of organic dyes. However, the E_g value of BUC-21 is approximately 3.4 eV, indicating that it can only utilize UV light source. Additionally, poor electronic conductivity of the pristine BUC-21 retards its photocatalytic application [262]. Hence, the combination of BUC-21 with such inorganic semiconductors, those having visible-light-harvesting ability and high conductivity should be an ideal method. For broadening the solar absorption range, $\text{Bi}_{24}\text{O}_{31}\text{Br}_{10}$ ($E_g \approx 2.70$ eV) considered as a competitive candidate [336]. Furthermore, the CB of $\text{Bi}_{24}\text{O}_{31}\text{Br}_{10}$ was found to be negative enough for realizing lots of photocatalytic reactions [337-339]. Therefore, Zhao and co-workers [44] fabricated BUC-21/ $\text{Bi}_{24}\text{O}_{31}\text{Br}_{10}$ composites (BB- x , x was the weight percentage of $\text{Bi}_{24}\text{O}_{31}\text{Br}_{10}$ with respect to the BUC-21) by ball-milling BUC-21 and $\text{Bi}_{24}\text{O}_{31}\text{Br}_{10}$ mixture (as illustrated in Figure 16(a)). The successful fabrication of BUC-21/ $\text{Bi}_{24}\text{O}_{31}\text{Br}_{10}$ composites was confirmed by PXRD, FTIR, UV-vis DRS, and XPS analysis. As shown in Figure 16(b), after the introduction of $\text{Bi}_{24}\text{O}_{31}\text{Br}_{10}$, BB- x composites exhibited the similar absorptions to pure $\text{Bi}_{24}\text{O}_{31}\text{Br}_{10}$ with long tails at the longer wavelengths, further showed that increasing $\text{Bi}_{24}\text{O}_{31}\text{Br}_{10}$ loading enhanced the optical absorption intensity in visible region. This phenomenon revealed that the forming BUC-21/ $\text{Bi}_{24}\text{O}_{31}\text{Br}_{10}$ composites were capable of improving the absorption of UV and visible lights and the composites could be considered as white-light-responsive photocatalysts. Being compared with the traditional solvothermal method, the SEM, TEM, and HRTEM images (Figure 16(c)-(e)) suggesting highly dispersed and uniformly distributed $\text{Bi}_{24}\text{O}_{31}\text{Br}_{10}$ nanosheets on the surface of BUC-21 polyhedron structures via the ball-milling process. As depicted in Figure 16(f), the best photocatalytic efficiency exhibited by BB-100, as it was capable to reduce 99.9% Cr(VI) into Cr(III) within 120 min upon irradiation of white light. Moreover, the photocatalytic activities of Cr(VI) reduction over different photocatalysts were shown in Table 4. The results indicated that BUC-21/ $\text{Bi}_{24}\text{O}_{31}\text{Br}_{10}$ composite was a superior white-light-responsive photocatalyst for reducing Cr(VI).

Table 4. Comparison of different photocatalysts for Cr(VI) reduction.

Photocatalyst	Dosage	pH	Concentration	Time	Light source	Efficiency	Ref.
---------------	--------	----	---------------	------	--------------	------------	------

	(g·L ⁻¹)		(mg·L ⁻¹)	(min)		(%)	
NH ₂ -MIL-68(In)	1.0	2.0	20.0	180	300 W Xe lamp ($\lambda > 420$ nm)	97.0	[340]
SrTiO ₃ microsphere	1.0	2.0	10.0	240	500 W Xe lamp	99.0	[341]
Bi ₂ S ₃ nanosphere	0.5	2.0	40.0	120	500 W Xe lamp ($\lambda > 420$ nm)	90.0	[342]
ZnIn ₂ S ₄	1.0	6.0	50.0	120	300 W Xe lamp ($\lambda > 420$ nm)	75.1	[343]
CuS/MIL-125(Ti)	0.5	2.1	48.0	70	500 W Xe lamp ($\lambda > 420$ nm)	52.0	[30]
g-C ₃ N ₄ /MIL-53(Fe)	0.4	2.0	10.0	180	500 W Xe lamp ($\lambda > 420$ nm)	99.0	[344]
CdS/TiO ₂	0.375	No data	10.0	60	300 W Xe lamp ($\lambda > 420$ nm)	90.0	[345]
SnS ₂ /SnO ₂	2.4	2.0	10.0	120	300 W Xe lamp ($\lambda > 400$ nm)	100	[346]
BiVO ₄ /MOS ₂	0.4	No data	15.0	90	500 W Xe lamp ($\lambda > 420$ nm)	76.5	[347]
g-BN/BiOCl	0.8	2.0	10.0	150	300 W Xe lamp ($\lambda > 420$ nm)	92.0	[348]
Co ₃ O ₄ /Ag/Bi ₂ WO ₆	1.0	3.0	40.0	60	300 W Xe lamp ($\lambda > 420$ nm)	58.0	[349]
ZnO/graphene	1.0	No data	10.0	250	500 W high pressure Hg lamp	98.0	[350]
Ni ₃ S ₂ /graphene	1.0	No data	20.0	180	300 W Xe lamp ($\lambda > 400$ nm)	91.0	[351]
CdS/RGO	1.0	No data	10.0	250	400 W metal halogen lamp ($\lambda > 400$ nm)	92.0	[352]
BUC-21/Bi ₂₄ O ₃₁ Br ₁₀	0.25	2.0	10.0	120	500 W Xe lamp	99.0	[44]

The improved reduction capability for Cr(VI) can be associated with enhanced solar absorption range and the rapid charge transfer at the interface of heterojunction. Furthermore, different small organic acids (SOAs), initial pH, water matrices and light intensities played significant roles in the photocatalytic process. Meanwhile, the methodology based on Box-Behnken experimental design authenticated that co-existence of inorganic ions and dissolved organic matter (DOM) significantly affect the photoreduction efficiency. More importantly, considering that the redox potential of Bi³⁺/Bi is 0.308 V vs. NHE [353], so the reduction of Bi³⁺ by photo-generated electrons is quite easy, which may also lead to reducing the photocatalytic performance for Cr(VI) removal. However, after

the combination of BUC-21 and $\text{Bi}_{24}\text{O}_{31}\text{Br}_{10}$, 4 cycling experiments were enough to remove 83.1% of Cr(VI), revealing the good recyclability of BB-100 during the adsorption-photocatalytic experiments (Figure 16(g)). Furthermore, the PL spectra, EIS Nyquist plots, time-resolved PL decay spectra and photocurrent response signals (Figure 16(h)) worked together to prove the formation of the composite between BUC-21 and $\text{Bi}_{24}\text{O}_{31}\text{Br}_{10}$ was capable to suppress the recombination of photo-generated charges. As illustrated in Figure 16(i), the photo-generated electrons present in the LUMO of BUC-21 were transferred to the CB of the $\text{Bi}_{24}\text{O}_{31}\text{Br}_{10}$. Additionally, the holes were consumed by H_2O to produce H_2O_2 [354]. Meanwhile, the generation of $\cdot\text{O}_2^-$ could induce a $\cdot\text{O}_2^-$ -mediated Cr(VI) reduction process, hence improving the separating potential of electron-hole pairs and promoted the Cr(VI) removal. The involved reactions were listed as Equations (9)-(13). Additionally, the density functional theory (DFT) simulations based on the difference of electron density and Hirshfeld charge analysis further suggested the photo-generated electrons transferred from BUC-21 to $\text{Bi}_{24}\text{O}_{31}\text{Br}_{10}$ (Figure 16(j)). Recently, ball-milling technology has been widely used for fabricating catalysts in the industrial fields [355-358]. It is easy to achieve large-scale synthesis of homogeneous catalysts with high reproducibility [357]. This study was attractive since the MBCs were constructed via facile ball-milling route. Moreover, this work revealed that coupling with bismuth-rich bismuth oxyhalides ($\text{Bi}_x\text{O}_y\text{X}_z$, X = Cl, Br and I) should be considered as an important way to reduce the recombination of charge carriers owing to they possessed more negative CB positions that could match the most of MOFs' band energies.

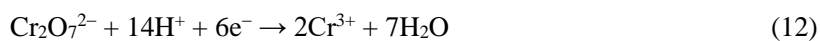
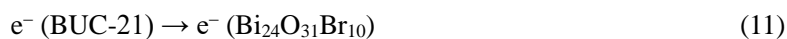
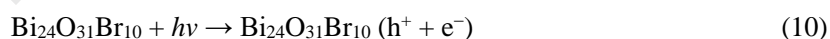
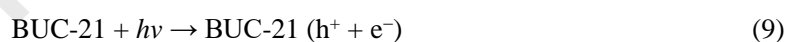


Figure 16. (a) The procedure for the preparation of BUC-21/ $\text{Bi}_{24}\text{O}_{31}\text{Br}_{10}$ composites, (b) UV-vis DRS spectra of BUC-21, $\text{Bi}_{24}\text{O}_{31}\text{Br}_{10}$ and the corresponding composites, (c)-(e) SEM, TEM and HRTEM images of BB-100, (f) Cr(VI) photoreduction at pH = 2 via numerous photocatalysts, (g) recycling experiments for the photoreduction of Cr(VI) over BB-100 and $\text{Bi}_{24}\text{O}_{31}\text{Br}_{10}$, (h) time-

resolved PL decay spectra of BUC-21, $\text{Bi}_{24}\text{O}_{31}\text{Br}_{10}$, and BB-*x* composites, (i) representation of the possible mechanism of photoreduction of Cr(VI) over BB-100 under white light and (j) difference of electron density on the surface of BUC-21 and $\text{Bi}_{24}\text{O}_{31}\text{Br}_{10}$ fragment [44], copyright (2020) Elsevier.

In addition to the BUC-21, ZIF-67 is also a subclass of microporous MOFs, consisting of imidazole-based ligands and cobalt ions in the form of zeolite topology [359-361]. Similar to ZIF-8, it possesses high surface area, high porosity as well as water stability. ZIF-67 is a favorable photocatalyst due to it possesses a narrow bandgap of 1.9 eV [362], however, it is worth mention that there are few studies on photocatalytic degradation of organic pollutants by pristine ZIF-67 or its composites. In 2020, Askari and co-workers [121] synthesized a novel double Z-scheme $\text{CuWO}_4/\text{Bi}_2\text{S}_3/\text{ZIF-67}$ ternary composite through the hydrothermal method. Furthermore, the photodegradation efficiencies of MTZ and CFX antibiotics by $\text{CuWO}_4/\text{Bi}_2\text{S}_3/\text{ZIF-67}$ were investigated in a batch and continuous slurry photoreactor under LED illumination (Figure 17(a)). The successful fabrication was testified by some common characterization techniques, such as PXRD, FTIR, PL, UV-vis DRS, TEM and SEM analysis. As shown in Figure 17(b) and (c), the TEM images exhibited that the $\text{CuWO}_4/\text{Bi}_2\text{S}_3$ composite was almost rod-shaped particles with size of 20-100 nm. And the $\text{CuWO}_4/\text{Bi}_2\text{S}_3/\text{ZIF-67}$ displayed the maintained flower-like morphology of the ZIF-67 even after the encapsulation of $\text{CuWO}_4/\text{Bi}_2\text{S}_3$. The ternary composite exhibited a remarkable improvement in photoactivity compared with $\text{CuWO}_4/\text{Bi}_2\text{S}_3$ and pristine ZIF-67. The apparent reaction rate of $\text{CuWO}_4/\text{Bi}_2\text{S}_3/\text{ZIF-67}$ composite was 9, 5.5, and 4 times higher than that obtained by Bi_2S_3 , ZIF-67, and the binary $\text{CuWO}_4/\text{Bi}_2\text{S}_3$, respectively. Indeed, higher surface area, narrower bandgap and better charge separation based on the dual Z-scheme structure caused the enhancement of photocatalytic activity. As shown in Figure 17(d)-(e), the maximum degradation efficiencies by the new ternary heterostructure were 95.6% and 90.1% for MTZ and CFX at optimum conditions in the continuous flow mode. Additionally, after 100 min illumination, the TOC removal rates by $\text{CuWO}_4/\text{Bi}_2\text{S}_3/\text{ZIF-67}$ reached 83.2% and 74% for MTZ and CFX, respectively (Figure 17(f)). This result suggested that the $\text{CuWO}_4/\text{Bi}_2\text{S}_3/\text{ZIF-67}$ composite had a good mineralization capacity for organic pollutants decomposition. Combining with the trapping tests ($\cdot\text{OH}$ was the most primary oxidant) and band positions of the heterostructural components, the

possible photocatalytic mechanism for the $\text{CuWO}_4/\text{Bi}_2\text{S}_3/\text{ZIF-67}$ composite should be proposed as followings. For the conventional $\text{CuWO}_4/\text{Bi}_2\text{S}_3/\text{ZIF-67}$ composite (Figure 17(g)), the photo-generated electrons on the LUMO of ZIF-67 and CB of Bi_2S_3 transferred to the CB of CuWO_4 , whereas the holes on the VB of Bi_2S_3 and CuWO_4 shifted to that of ZIF-67. Although the separation of the photo-generated charges would be efficient, ZIF-67 was not able to generate $\cdot\text{OH}$ via oxidization of the adsorbed H_2O molecules due to its E_{HOMO} was less positive redox potential than that of standard one $\text{H}_2\text{O}/\cdot\text{OH}$ (2.72 eV *vs.* NHE). Meanwhile, O_2 reduction into the $\cdot\text{O}_2^-$ cannot be possible by the CB electrons of CuWO_4 , as more negative redox potential was required for $\text{O}_2/\cdot\text{O}_2^-$ (-0.33 eV *vs.* NHE) than that of E_{CB} of CuWO_4 . Therefore, charge transfer via a double Z-scheme mechanism was offered to describe the elevated degradation efficiencies for MTZ and CFX by the ternary $\text{CuWO}_4/\text{Bi}_2\text{S}_3/\text{ZIF-67}$ composite. As illustrated in Figure 17(h), which was showing the recombination of photo-generated holes in the HOMO of ZIF-67 with the electrons in the CB of Bi_2S_3 and photo-generated electrons of CuWO_4 with the holes in the VB of Bi_2S_3 . Accordingly, the LUMO electrons of ZIF-67 with suitable redox potential (-0.65 eV *vs.* NHE) can easily reduce the O_2 to form $\cdot\text{O}_2^-$, subsequently capable to react with H_2O to form $\cdot\text{OH}$. At the same time, the accumulated holes in the VB of CuWO_4 were also capable to generate $\cdot\text{OH}$ by reacting with H_2O . This work was novel because a double Z-scheme $\text{CuWO}_4/\text{Bi}_2\text{S}_3/\text{ZIF-67}$ ternary composite was successfully fabricated, which not only accelerated the charge carriers transfer, but also retained the high redox ability in the as-prepared composite. Future researches could attempt to introduce a third semiconductor into a binary heterojunction for the construction of double Z-scheme ternary composite, which was expected to have superior photocatalytic activity.

Figure 17. (a) Schematic representation of the continuous flow reactor, (b)-(c) TEM images of $\text{CuWO}_4/\text{Bi}_2\text{S}_3$ and $\text{CuWO}_4/\text{Bi}_2\text{S}_3/\text{ZIF-67}$ composite, (d)-(e) the effect of adsorption, photolysis and photocatalysis processes on MTZ and CFX degradation at optimum conditions (pH = 7, photocatalyst dosage = $0.3 \text{ g}\cdot\text{L}^{-1}$, antibiotic concentration = $20 \text{ mg}\cdot\text{L}^{-1}$), (f) TOC removal of MTZ and CFX by the binary and ternary composites under LED irradiation at pH = 7 and photocatalyst dosage = $0.3 \text{ g}\cdot\text{L}^{-1}$, proposed photocatalytic mechanism for $\text{CuWO}_4/\text{Bi}_2\text{S}_3/\text{ZIF-67}$ composite under light irradiation: (g) conventional path and (h) double Z-scheme structure [121], copyright (2020)

Elsevier.

3. Conclusions and outlooks

This review article highlighted the fabrication methods and characterizations of MBCs, as well as their applications in heterogeneous photocatalysis, including organic pollutants degradation, NO oxidation, N₂ fixation, Cr(VI) reduction and O₂ production. Although the application of MBCs in the photocatalysis field is currently at the early stages, the above-described works represent their tremendous potential in the practical applications. Up to now, four synthetic strategies are mainly adopted to prepare binary MBCs: (i) ultrasonic treatment or ball-milling treatments towards the as-prepared MOF and bismuth-based semiconductor; (ii) in-situ formation of MOF from its metal template and organic ligand on the as-prepared bismuth-based semiconductor at room temperature; (iii) in-situ deposition of bismuth-based semiconductor from its precursors onto the as-prepared MOF; (iv) hydrothermal or solvothermal treatment of the mixture containing the as-prepared MOF (bismuth-based semiconductor) and the precursors of bismuth-based semiconductor (MOF). As to ternary and quaternary composites, the most common approach taken by researchers is in-situ MOF deposition from its precursors on another type of semiconductor prepared before, following by in-situ deposition of bismuth-based semiconductor or composites from its precursors on the as-prepared binary MOF-based composites. Alternatively, the ternary MBCs can be fabricated via hydrothermal treatment for the mixture containing the as-prepared MOF and precursors of bismuth-based material and the third compound after ultrasonic processing.

In general, MBCs combine the respective properties of bismuth-based semiconductors and MOFs, sometimes they also exhibited unexpected catalytic performances and merits: (i) enhancement of the light-harvesting ability; (ii) increasement of the number of active sites; (iii) stabilization and dispersion of the bismuth-based semiconductors by MOFs; (iv) reduction of the bismuth-based semiconductors photo-corrosion; (v) decrease in the recombination of photo-generated charges and facilitation of the interfacial charge transfer. Despite such remarkable advantages of MBCs in the photocatalysis field, more efforts should be required for the practical applications.

(1) It is imperative to further improve the sensitivity of the MBCs for the visible-light via modulating the energy band of the individual coupling component. With respect to MOFs, it is

difficult to immobilize -NH_2 group or the other modified groups at the desired sites or the coordination mode of the original ligand might be changed after introducing some new groups. Therefore, modification with a new organic ligand not always be feasible. As illustrated in Figure 1(b), only a few CBs of the bismuth-based materials having redox potential higher than that of H^+/H_2 , whereas all VBs are more positive redox potential than that of $\text{O}_2/\text{H}_2\text{O}$. Hence, it would be preferred to modulate the bismuth-based material's VB to narrow the bandgap. The most important approaches include doping with 3d-transition elements (Fe, Co, Ni, Cu, Mn, Cr, Zn), with cations having d^{10} or $d^{10}s^2$ configurations (Pd , Ag^+ , Cd^{2+} , Pb^{2+}) and with non-metal elements (N, B, F, S).

(2) The photocatalytic properties of MOFs and bismuth-based semiconductors are extremely dependent on their size and morphological characteristics. In most of the existing studies, bismuth-based semiconductors are mainly of layer structures. Accordingly, the activity of bismuth-based photocatalysts can be increase by developing ultrathin, hollow, hierarchical and 3D super-structures (flower-, sphere- and tyre-like structures). Additionally, the morphology of MOFs can be controlled through surfactants such as cetyltrimethylammonium bromide (CTAB) and polyvinylpyrrolidone (PVP). In conclusion, morphological adjustment of MOFs or bismuth-based photocatalysts can increase light absorption, accelerate the migration of carriers from bulk to surface, improve mass diffusion of reactants/intermediate products and reduce the dosage of photocatalysts.

(3) As for the preparation of MBCs, most of the researches are still at the lab-scale for synthesizing a small number of photocatalysts. More importantly, some of these fabrication processes are difficult to control as they are highly complex. Therefore, the development of more facile and kilogram level high-throughput methods (especially the one-step synthesis methods) is highly desirable.

(4) Reported studies on MBCs were mainly based on their photocatalytic degradation capability towards organic pollutants. The main obstacle is the less negative CB of bismuth-based materials, leading to the poor reducing abilities. However, in a variety of photoreduction reactions such as $\text{CO}_2/\text{Cr(VI)}$ reduction and H_2 evolution, MOFs have successfully been utilized. In the future, the construction of direct Z-scheme heterojunctions by coupling bismuth-based photocatalysts and MOFs with the LUMO of significant negativity is an effective method for exploring their reduction applications.

(5) Due to the presence of large amounts of unsaturated coordination metal centers, MOFs containing transition metal ions (Co^{2+} , Cu^{2+} , Fe^{2+} , etc.) can trigger $\cdot\text{OH}$ or $\text{SO}_4^{\cdot-}$ based advanced oxidation processes (AOPs). However, pristine MOFs might not efficiently activate hydrogen peroxide (H_2O_2), peroxymonosulfate (PMS), or persulfate (PS). So, under the specific light irradiation, combination of Co-, Cu-, Fe-MOFs and bismuth-based photocatalysts can not only accelerate the photo-generated charges transfer but also induce the formation of more free radicals with strong oxidizing capacities. Thus, the reaction system will show a remarkable synergistic effect in removing organic pollutants.

(6) As to the applications, more organic pollutants should be selected to examine the photocatalytic efficiencies of MBCs. These pollutants may be from perfluorinated organic compounds (PFCs) and pharmaceutical and personal care products (PPCPs). Moreover, proceeding application of MBCs towards the degradation of gaseous volatile organic compounds (VOCs) is also very meaningful. Importantly, for the application in pollutants degradation, the intermediate should be evaluated properly for their relative toxicities as the mineralization of pollutants sometimes remains incomplete during the photocatalytic degradation process. Furthermore, the environmental risk factors of fabricated MBCs should be completely assessed before the practical applications.

(7) Theoretical simulations like DFT should be conducted to deeply explore the structure-activity relationship. For instance, the roles of both MOFs and bismuth-based semiconductors should be properly recognized. Moreover, efforts should be made to collect the information required to achieve the distinguished photocatalytic activity, thus providing a guide for showing the mechanism of the photocatalytic process.

(8) As MBCs are mainly used in the field of environmental remediation, they inevitably get in touch with environment voluntarily or accidentally. Therefore, the ecological and environmental impacts of MBCs should be comprehensively investigated via life cycle assessment (LCA). Considering that organic solvents and high temperature treatments are usually applied during the MBCs fabrication processes, it is deemed necessary to estimate the environmental impacts of various MBCs fabrication methods and to confirm the most eco-friendly synthesis route. Moreover, some ecotoxicological effects of MBCs, such as fresh water aquatic ecotoxicity potential, human

toxicity potential and marine aquatic ecotoxicity potential should be analyzed in the future works.

(9) Last but not least, it is impossible to progress this field of without conducting research on MOFs. So, new cost-effective and highly stable MOFs with admirable photocatalytic activities and tailorable structures should be further developed, as it is highly required for the scientific design of MBCs.

Acknowledgments

This work was supported by the National Natural Science Foundation of China (21876008 and 51878023), Beijing Natural Science Foundation (No.8202016), Great Wall Scholars Training Program Project of Beijing Municipality Universities (CIT&TCD20180323), Beijing Talent Project (2019A22), The Fundamental Research Funds for Beijing University of Civil Engineering and Architecture (X20147/X20141/X20135/X20146).

References

- [1] L.V. Bora, R.K. Mewada, Visible/solar light active photocatalysts for organic effluent treatment: fundamentals, mechanisms and parametric review, *Renew. Sust. Energ. Rev.*, 76 (2017) 1393-1421.
- [2] Y. Nosaka, A.Y. Nosaka, Generation and detection of reactive oxygen species in photocatalysis, *Chem. Rev.*, 117 (2017) 11302-11336.
- [3] K.C. Christoforidis, P. Fornasiero, Photocatalysis for hydrogen production and CO₂ reduction: the case of copper-catalysts, *ChemCatChem.*, 11 (2019) 368-382.
- [4] H. Kisch, Semiconductor photocatalysis for chemoselective radical coupling reactions, *Accounts. Chem. Res.*, 50 (2017) 1002-1010.
- [5] U. Ulmer, T. Dingle, P.N. Duchesne, R.H. Morris, A. Tavasoli, T. Wood, G.A. Ozin, Fundamentals and applications of photocatalytic CO₂ methanation, *Nat. Commun.*, 10 (2019) 3169.
- [6] A. Fujishima, K. Honda, Electrochemical photolysis of water at a semiconductor electrode, *Nature.*, 238 (1972) 37-38.
- [7] A. Shayganpour, A. Reverberi, M. Salerno, B. Fabiano, Electrochemical fabrication of anodic nanoporous titania for photocatalytic degradation of pollutants, *Chem. Eng. Trans.*, 47 (2016) 301-306.
- [8] C.P. Athanasekou, V. Likodimos, P. Falaras, Recent developments of TiO₂ photocatalysis involving advanced oxidation and reduction reactions in water, *J. Environ. Chem. Eng.*, 6 (2018) 7386-7394.
- [9] I.J. Ani, U.G. Akpan, M.A. Olutoye, B.H. Hameed, Photocatalytic degradation of pollutants in petroleum refinery wastewater by TiO₂- and ZnO-based photocatalysts: recent development, *J. Clean. Prod.*, 205 (2018) 930-954.
- [10] C.A. Jaramillo-Páez, J.A. Navío, M.C. Hidalgo, M. Macías, ZnO and Pt-ZnO

photocatalysts: characterization and photocatalytic activity assessing by means of three substrates, *Catal. Today.*, 313 (2018) 12-19.

[11] H.-Q. Xu, S. Yang, X. Ma, J. Huang, H.-L. Jiang, Unveiling charge-separation dynamics in CdS/metal–organic framework composites for enhanced photocatalysis, *ACS. Catal.*, 8 (2018) 11615-11621.

[12] X. Wu, S. Xie, C. Liu, C. Zhou, J. Lin, J. Kang, Q. Zhang, Z. Wang, Y. Wang, Ligand-controlled photocatalysis of CdS quantum dots for lignin valorization under visible light, *ACS. Catal.*, 9 (2019) 8443-8451.

[13] P. Garg, S. Kumar, I. Choudhuri, A. Mahata, B. Pathak, Hexagonal planar CdS monolayer sheet for visible light photocatalysis, *J. Phys. Chem. C.*, 120 (2016) 7052-7060.

[14] M. Barroso, A.J. Cowan, S.R. Pendlebury, M. Grätzel, D.R. Klug, J.R. Durrant, The role of cobalt phosphate in enhancing the photocatalytic activity of α -Fe₂O₃ toward water oxidation, *J. Am. Chem. Soc.*, 133 (2011) 14868-14871.

[15] P. Basnet, G.K. Larsen, R.P. Jadeja, Y.-C. Hung, Y. Zhao, α -Fe₂O₃ nanocolumns and nanorods fabricated by electron beam evaporation for visible light photocatalytic and antimicrobial applications, *ACS. Appl. Mater. Inter.*, 5 (2013) 2085-2095.

[16] J.L.C. Rowsell, O.M. Yaghi, Metal–organic frameworks: a new class of porous materials, *Micropor. Mesopor. Mat.*, 73 (2004) 3-14.

[17] Z. Hasan, S.H. Jhung, Removal of hazardous organics from water using metal-organic frameworks (MOFs): plausible mechanisms for selective adsorptions, *J. Hazard. Mater.*, 283 (2015) 329-339.

[18] S.L. James, Metal-organic frameworks, *Chem. Soc. Rev.*, 32 (2003) 276-288.

[19] Y. Liu, Z. Liu, D. Huang, M. Cheng, G. Zeng, C. Lai, C. Zhang, C. Zhou, W. Wang, D. Jiang, H. Wang, B. Shao, Metal or metal-containing nanoparticle@MOF nanocomposites as a promising type of photocatalyst, *Coordin. Chem. Rev.*, 388 (2019) 63-78.

[20] H. Furukawa, N. Ko, Y.B. Go, N. Aratani, S.B. Choi, E. Choi, A.Ö. Yazaydin, R.Q. Snurr, M. O’Keeffe, J. Kim, O.M. Yaghi, Ultrahigh porosity in metal-organic frameworks, *Science.*, 329 (2010) 424-428.

[21] X. Yang, Q. Xu, Bimetallic metal–organic frameworks for gas storage and separation, *Cryst. Growth. Des.*, 17 (2017) 1450-1455.

[22] R.-B. Lin, S. Xiang, H. Xing, W. Zhou, B. Chen, Exploration of porous metal–organic frameworks for gas separation and purification, *Coordin. Chem. Rev.*, 378 (2019) 87-103.

[23] P.K. Thallapally, J. Tian, M. Radha Kishan, C.A. Fernandez, S.J. Dalgarno, P.B. McGrail, J.E. Warren, J.L. Atwood, Flexible (breathing) interpenetrated metal–organic frameworks for CO₂ separation applications, *J. Am. Chem. Soc.*, 130 (2008) 16842-16843.

[24] B. Panella, M. Hirscher, H. Pütter, U. Müller, Hydrogen adsorption in metal–organic frameworks: Cu-MOFs and Zn-MOFs compared, *Adv. Funct. Mater.*, 16 (2006) 520-524.

[25] J. Canivet, A. Fateeva, Y. Guo, B. Coasne, D. Farrusseng, Water adsorption in MOFs: fundamentals and applications, *Chem. Soc. Rev.*, 43 (2014) 5594-5617.

[26] I. Abánades Lázaro, R.S. Forgan, Application of zirconium MOFs in drug delivery and biomedicine, *Coordin. Chem. Rev.*, 380 (2019) 230-259.

[27] M. Filippousi, S. Turner, K. Leus, P.I. Sifaka, E.D. Tseligka, M. Vandichel, S.G. Nanaki, I.S. Vizirianakis, D.N. Bikiaris, P. Van Der Voort, G. Van Tendeloo, Biocompatible Zr-based nanoscale MOFs coated with modified poly(ϵ -caprolactone) as anticancer drug carriers, *Int. J.*

Pharmaceut., 509 (2016) 208-218.

[28] L.E. Kreno, K. Leong, O.K. Farha, M. Allendorf, R.P. Van Duyne, J.T. Hupp, Metal–organic framework materials as chemical sensors, *Chem. Rev.*, 112 (2012) 1105-1125.

[29] I. Stassen, N. Burtch, A. Talin, P. Falcaro, M. Allendorf, R. Ameloot, An updated roadmap for the integration of metal–organic frameworks with electronic devices and chemical sensors, *Chem. Soc. Rev.*, 46 (2017) 3185-3241.

[30] C.-C. Wang, X.-D. Du, J. Li, X.-X. Guo, P. Wang, J. Zhang, Photocatalytic Cr(VI) reduction in metal-organic frameworks: a mini-review, *Appl. Catal. B. Environ.*, 193 (2016) 198-216.

[31] C.-C. Wang, J.-R. Li, X.-L. Lv, Y.-Q. Zhang, G. Guo, Photocatalytic organic pollutants degradation in metal–organic frameworks, *Energ. Environ. Sci.*, 7 (2014) 2831-2867.

[32] Z. Zhang, L. Bai, X. Hu, Alkene hydrosilylation catalyzed by easily assembled Ni(ii)-carboxylate MOFs, *Chem. Sci.*, 10 (2019) 3791-3795.

[33] J. Qiu, X. Zhang, Y. Feng, X. Zhang, H. Wang, J. Yao, Modified metal-organic frameworks as photocatalysts, *Appl. Catal. B. Environ.*, 231 (2018) 317-342.

[34] Q. Wang, Q. Gao, A.M. Al-Enizi, A. Nafady, S. Ma, Recent advances in MOF-based photocatalysis: environmental remediation under visible light, *Inorg. Chem. Front.*, 7 (2020) 300-339.

[35] L. Shen, R. Liang, L. Wu, Strategies for engineering metal-organic frameworks as efficient photocatalysts, *Chin. J. Catal.*, 36 (2015) 2071-2088.

[36] M.A. Nasalevich, M. van der Veen, F. Kapteijn, J. Gascon, Metal–organic frameworks as heterogeneous photocatalysts: advantages and challenges, *CrystEngComm.*, 16 (2014) 4919-4926.

[37] C.-C. Wang, X.-H. Yi, P. Wang, Powerful combination of MOFs and C₃N₄ for enhanced photocatalytic performance, *Appl. Catal. B. Environ.*, 247 (2019) 24-48.

[38] S. Wang, X. Wang, Multifunctional metal–organic frameworks for photocatalysis, *Small.*, 11 (2015) 3097-3112.

[39] Y.-X. Li, X. Wang, C.-C. Wang, H. Fu, Y. Liu, P. Wang, C. Zhao, S-TiO₂/UiO-66-NH₂ composite for boosted photocatalytic Cr(VI) reduction and bisphenol a degradation under LED visible light, *J. Hazard. Mater.*, 399 (2020) 123085.

[40] H. Li, C. Zhao, X. Li, H. Fu, Z. Wang, C.-C. Wang, Boosted photocatalytic Cr(VI) reduction over Z-scheme MIL-53(Fe)/Bi₁₂O₁₇Cl₂ composites under white light, *J. Alloy. Compd.*, 844 (2020) 156147.

[41] D.-D. Chen, X.-H. Yi, L. Ling, C.-C. Wang, P. Wang, Photocatalytic Cr(VI) sequestration and photo-fenton bisphenol a decomposition over white light responsive PANI/MIL-88A(Fe), *Appl. Organomet. Chem.*, 34 (2020) e5795.

[42] X. Wei, P. Wang, H. Fu, C. Zhao, C.-C. Wang, Boosted photocatalytic elimination toward Cr(VI) and organic pollutants over BUC-21/Cd_{0.5}Zn_{0.5}S under LED visible light, *Mater. Res. Bull.*, 129 (2020) 110903.

[43] X. Wang, Y.-X. Li, X.-H. Yi, C. Zhao, P. Wang, J. Deng, C.-C. Wang, Photocatalytic Cr(VI) elimination over BUC-21/N-K₂Ti₄O₉ composites: big differences in performance resulting from small differences in composition, *Chin. J. Catal.*, 42 (2021) 259-270.

[44] C. Zhao, Z. Wang, X. Li, X. Yi, H. Chu, X. Chen, C.-C. Wang, Facile fabrication of BUC-21/Bi₂₄O₃₁Br₁₀ composites for enhanced photocatalytic Cr(VI) reduction under white light, *Chem. Eng. J.*, 389 (2020) 123431.

- [45] X. Wang, W. Liu, H. Fu, X.-H. Yi, P. Wang, C. Zhao, C.-C. Wang, W. Zheng, Simultaneous Cr(VI) reduction and Cr(III) removal of bifunctional MOF/Titanate nanotube composites, *Environ. Pollut.*, 249 (2019) 502-511.
- [46] X.-H. Yi, F.-X. Wang, X.-D. Du, P. Wang, C.-C. Wang, Facile fabrication of BUC-21/g-C₃N₄ composites and their enhanced photocatalytic Cr(VI) reduction performances under simulated sunlight, *Appl. Organomet. Chem.*, 33 (2019) e4621.
- [47] Y.-C. Zhou, P. Wang, H. Fu, C. Zhao, C.-C. Wang, Ternary Ag/Ag₃PO₄/MIL-125-NH₂ Z-scheme heterojunction for boosted photocatalytic Cr(VI) cleanup under visible light, *Chin. Chem. Lett.*, 31 (2020), 2645-2650.
- [48] D.-D. Chen, X.-H. Yi, C. Zhao, H. Fu, P. Wang, C.-C. Wang, Polyaniline modified MIL-100(Fe) for enhanced photocatalytic Cr(VI) reduction and tetracycline degradation under white light, *Chemosphere.*, 245 (2020) 125659.
- [49] Y.-C. Zhou, X.-Y. Xu, P. Wang, H. Fu, C. Zhao, C.-C. Wang, Facile fabrication and enhanced photocatalytic performance of visible light responsive UiO-66-NH₂/Ag₂CO₃ composite, *Chin. J. Catal.*, 40 (2019) 1912-1923.
- [50] X.-H. Yi, S.-Q. Ma, X.-D. Du, C. Zhao, H. Fu, P. Wang, C.-C. Wang, The facile fabrication of 2D/3D Z-scheme g-C₃N₄/UiO-66 heterojunction with enhanced photocatalytic Cr(VI) reduction performance under white light, *Chem. Eng. J.*, 375 (2019) 121944.
- [51] X. Du, X. Yi, P. Wang, J. Deng, C.-c. Wang, Enhanced photocatalytic Cr(VI) reduction and diclofenac sodium degradation under simulated sunlight irradiation over MIL-100(Fe)/g-C₃N₄ heterojunctions, *Chin. J. Catal.*, 40 (2019) 70-79.
- [52] J.-W. Wang, F.-G. Qiu, P. Wang, C. Ge, C.-C. Wang, Boosted bisphenol a and Cr(VI) cleanup over Z-scheme WO₃/MIL-100(Fe) composites under visible light, *J. Clean. Prod.*, 279 (2020) 123408.
- [53] C.-C. Wang, X. Wang, W. Liu, The synthesis strategies and photocatalytic performances of TiO₂/MOFs composites: A state-of-the-art review, *Chem. Eng. J.*, 391 (2019) 123601.
- [54] T. Wu, X. Liu, Y. Liu, M. Cheng, Z. Liu, G. Zeng, B. Shao, Q. Liang, W. Zhang, Q. He, W. Zhang, Application of QD-MOF composites for photocatalysis: energy production and environmental remediation, *Coordin. Chem. Rev.*, 403 (2020) 213097.
- [55] R. He, D. Xu, B. Cheng, J. Yu, W. Ho, Review on nanoscale Bi-based photocatalysts, *Nanoscale. Horiz.*, 3 (2018) 464-504.
- [56] X. Meng, Z. Zhang, Bismuth-based photocatalytic semiconductors: introduction, challenges and possible approaches, *J. Mol. Catal. A. Chem.*, 423 (2016) 533-549.
- [57] H. Cheng, B. Huang, Y. Dai, Engineering BiOX (X = Cl, Br, I) nanostructures for highly efficient photocatalytic applications, *Nanoscale.*, 6 (2014) 2009-2026.
- [58] L. Ye, Y. Su, X. Jin, H. Xie, C. Zhang, Recent advances in BiOX (X = Cl, Br and I) photocatalysts: synthesis, modification, facet effects and mechanisms, *Environ. Sci. Nano.*, 1 (2014) 90-112.
- [59] H. Yu, L. Jiang, H. Wang, B. Huang, X. Yuan, J. Huang, J. Zhang, G. Zeng, Modulation of Bi₂MoO₆-based materials for photocatalytic water splitting and environmental application: a critical review, *Small.*, 15 (2019) 1901008.
- [60] L. Zhou, W. Wang, H. Xu, S. Sun, M. Shang, Bi₂O₃ hierarchical nanostructures: controllable synthesis, growth mechanism, and their application in photocatalysis, *Chem. Eur. J.*, 15 (2009) 1776-1782.

- [61] A.P. Reverberi, P.S. Varbanov, M. Voccianti, B. Fabiano, Bismuth oxide-related photocatalysts in green nanotechnology: a critical analysis, *Front. Chem. Sci. Eng.*, 12 (2018) 878-892.
- [62] M. Chahkandi, M. Zargazi, Novel method of square wave voltammetry for deposition of Bi_2S_3 thin film: photocatalytic reduction of hexavalent Cr in single and binary mixtures, *J. Hazard. Mater.*, 380 (2019) 120879.
- [63] Y.P. Bhoi, B.G. Mishra, Single step combustion synthesis, characterization and photocatalytic application of $\alpha\text{-Fe}_2\text{O}_3\text{-Bi}_2\text{S}_3$ heterojunctions for efficient and selective reduction of structurally diverse nitroarenes, *Chem. Eng. J.*, 316 (2017) 70-81.
- [64] T. Saison, N. Chemin, C. Chanéac, O. Durupthy, V. Ruaux, L. Mariey, F. Maugé, P. Beaunier, J.-P. Jolivet, Bi_2O_3 , BiVO_4 , and Bi_2WO_6 : impact of surface properties on photocatalytic activity under visible light, *J. Phys. Chem. C.*, 115 (2011) 5657-5666.
- [65] A. Martínez-de la Cruz, S.O. Alfaro, E.L. Cuéllar, U.O. Méndez, Photocatalytic properties of Bi_2MoO_6 nanoparticles prepared by an amorphous complex precursor, *Catal. Today.*, 129 (2007) 194-199.
- [66] S. Obregón, A. Caballero, G. Colón, Hydrothermal synthesis of BiVO_4 : structural and morphological influence on the photocatalytic activity, *Appl. Catal. B. Environ.*, 117-118 (2012) 59-66.
- [67] J.C. Ahern, R. Fairchild, J.S. Thomas, J. Carr, H.H. Patterson, Characterization of BiOX compounds as photocatalysts for the degradation of pharmaceuticals in water, *Appl. Catal. B. Environ.*, 179 (2015) 229-238.
- [68] G. Li, F. Qin, R. Wang, S. Xiao, H. Sun, R. Chen, BiOX ($\text{X}=\text{Cl}$, Br , I) nanostructures: mannitol-mediated microwave synthesis, visible light photocatalytic performance, and Cr(VI) removal capacity, *J. Colloid. Interf. Sci.*, 409 (2013) 43-51.
- [69] X. Jin, L. Ye, H. Xie, G. Chen, Bismuth-rich bismuth oxyhalides for environmental and energy photocatalysis, *Coordin. Chem. Rev.*, 349 (2017) 84-101.
- [70] Y. Liu, Y. Zhu, J. Xu, X. Bai, R. Zong, Y. Zhu, Degradation and mineralization mechanism of phenol by BiPO_4 photocatalysis assisted with H_2O_2 , *Appl. Catal. B. Environ.*, 142-143 (2013) 561-567.
- [71] S. Obregón, Y. Zhang, G. Colón, Cascade charge separation mechanism by ternary heterostructured $\text{BiPO}_4/\text{TiO}_2/\text{g-C}_3\text{N}_4$ photocatalyst, *Appl. Catal. B. Environ.*, 184 (2016) 96-103.
- [72] Z. Ni, Y. Sun, Y. Zhang, F. Dong, Fabrication, modification and application of $(\text{BiO})_2\text{CO}_3$ -based photocatalysts: a review, *Appl. Surf. Sci.*, 365 (2016) 314-335.
- [73] F. Gao, X.Y. Chen, K.B. Yin, S. Dong, Z.F. Ren, F. Yuan, T. Yu, Z.G. Zou, J.-M. Liu, Visible-light photocatalytic properties of weak magnetic BiFeO_3 nanoparticles, *Adv. Mater.*, 19 (2007) 2889-2892.
- [74] H. Zhang, H. Zheng, Y. Wang, R. Yan, D. Luo, W. Jiang, KBiO_3 as an effective visible-light-driven photocatalyst: stability improvement by in situ constructing $\text{KBiO}_3/\text{BiOX}$ ($\text{X} = \text{Cl}$, Br , I) heterostructure, *Ind. Eng. Chem. Res.*, 58 (2019) 1875-1887.
- [75] R.A. He, S. Cao, P. Zhou, J. Yu, Recent advances in visible light Bi-based photocatalysts, *Chin. J. Catal.*, 35 (2014) 989-1007.
- [76] L. Zhang, Z.-K. Tang, W.-M. Lau, W.-J. Yin, S.-X. Hu, L.-M. Liu, Tuning band gaps and optical absorption of BiOCl through doping and strain: insight from DFT calculations, *Phys. Chem. Chem. Phys.*, 19 (2017) 20968-20973.

- [77] T. Wu, X. Li, D. Zhang, F. Dong, S. Chen, Efficient visible light photocatalytic oxidation of NO with hierarchical nanostructured 3D flower-like $\text{BiOCl}_x\text{Br}_{1-x}$ solid solutions, *J. Alloy. Compd.*, 671 (2016) 318-327.
- [78] H. Li, T. Hu, J. Liu, S. Song, N. Du, R. Zhang, W. Hou, Thickness-dependent photocatalytic activity of bismuth oxybromide nanosheets with highly exposed (010) facets, *Appl. Catal. B. Environ.*, 182 (2016) 431-438.
- [79] G.-J. Lee, Y.-C. Zheng, J.J. Wu, Fabrication of hierarchical bismuth oxyhalides (BiOX , $\text{X}=\text{Cl}$, Br , I) materials and application of photocatalytic hydrogen production from water splitting, *Catal. Today.*, 307 (2018) 197-204.
- [80] N. Zhu, C. Li, L. Bu, C. Tang, S. Wang, P. Duan, L. Yao, J. Tang, D.D. Dionysiou, Y. Wu, Bismuth impregnated biochar for efficient estrone degradation: the synergistic effect between biochar and $\text{Bi/Bi}_2\text{O}_3$ for a high photocatalytic performance, *J. Hazard. Mater.*, 384 (2020) 121258.
- [81] J. Qiu, M. Li, J. Xu, X.-F. Zhang, J. Yao, Bismuth sulfide bridged hierarchical $\text{Bi}_2\text{S}_3/\text{BiOCl}@ \text{ZnIn}_2\text{S}_4$ for efficient photocatalytic Cr(VI) reduction, *J. Hazard. Mater.*, 389 (2020) 121858.
- [82] J. Zhang, G. Zhu, S. Li, F. Rao, Q.-U. Hassan, J. Gao, Y. Huang, M. Hojamberdiev, Novel $\text{Au/La-Bi}_5\text{O}_7\text{I}$ microspheres with efficient visible-light photocatalytic activity for NO removal: synergistic effect of Au nanoparticles, la doping, and oxygen vacancy, *ACS. Appl. Mater. Inter.*, 11 (2019) 37822-37832.
- [83] X. Yan, X. Zhu, R. Li, W. Chen, Au/BiOCl heterojunction within mesoporous silica shell as stable plasmonic photocatalyst for efficient organic pollutants decomposition under visible light, *J. Hazard. Mater.*, 303 (2016) 1-9.
- [84] B. Li, L. Tan, X. Liu, Z. Li, Z. Cui, Y. Liang, S. Zhu, X. Yang, K.W. Kwok Yeung, S. Wu, Superimposed surface plasma resonance effect enhanced the near-infrared photocatalytic activity of $\text{Au@Bi}_2\text{WO}_6$ coating for rapid bacterial killing, *J. Hazard. Mater.*, 380 (2019) 120818.
- [85] J. Resasco, H. Zhang, N. Kornienko, N. Becknell, H. Lee, J. Guo, A.L. Briseno, P. Yang, $\text{TiO}_2/\text{BiVO}_4$ nanowire heterostructure photoanodes based on type II band alignment, *ACS. Central. Sci.*, 2 (2016) 80-88.
- [86] S. Obregón, G. Colón, Erbium doped $\text{TiO}_2\text{-Bi}_2\text{WO}_6$ heterostructure with improved photocatalytic activity under sun-like irradiation, *Appl. Catal. B. Environ.*, 140-141 (2013) 299-305.
- [87] Y. Liu, F. Xin, F. Wang, S. Luo, X. Yin, Synthesis, characterization, and activities of visible light-driven $\text{Bi}_2\text{O}_3\text{-TiO}_2$ composite photocatalysts, *J. Alloy. Compd.*, 498 (2010) 179-184.
- [88] H. Zhao, G. Li, F. Tian, Q. Jia, Y. Liu, R. Chen, g- C_3N_4 surface-decorated $\text{Bi}_2\text{O}_2\text{CO}_3$ for improved photocatalytic performance: theoretical calculation and photodegradation of antibiotics in actual water matrix, *Chem. Eng. J.*, 366 (2019) 468-479.
- [89] D. Ma, J. Wu, M. Gao, Y. Xin, T. Ma, Y. Sun, Fabrication of Z-scheme g- $\text{C}_3\text{N}_4/\text{RGO/Bi}_2\text{WO}_6$ photocatalyst with enhanced visible-light photocatalytic activity, *Chem. Eng. J.*, 290 (2016) 136-146.
- [90] N. Lv, Y. Li, Z. Huang, T. Li, S. Ye, D.D. Dionysiou, X. Song, Synthesis of $\text{GO/TiO}_2/\text{Bi}_2\text{WO}_6$ nanocomposites with enhanced visible light photocatalytic degradation of ethylene, *Appl. Catal. B. Environ.*, 246 (2019) 303-311.
- [91] Y. Wang, K. Ding, R. Xu, D. Yu, W. Wang, P. Gao, B. Liu, Fabrication of $\text{BiVO}_4/\text{BiPO}_4/\text{GO}$ composite photocatalytic material for the visible light-driven degradation, *J. Clean. Prod.*, 247 (2020) 119108.

- [92] L. Ye, Y. Deng, L. Wang, H. Xie, F. Su, Bismuth-based photocatalysts for solar photocatalytic carbon dioxide conversion, *ChemSusChem.*, 12 (2019) 3671-3701.
- [93] S.Y. Chai, Y.J. Kim, M.H. Jung, A.K. Chakraborty, D. Jung, W.I. Lee, Heterojunctioned BiOCl/Bi₂O₃, a new visible light photocatalyst, *J. Catal.*, 262 (2009) 144-149.
- [94] M. Miodyńska, A. Mikolajczyk, B. Bajorowicz, J. Zwara, T. Klimczuk, W. Lisowski, G. Trykowski, H.P. Pinto, A. Zaleska-Medynska, Urchin-like TiO₂ structures decorated with lanthanide-doped Bi₂S₃ quantum dots to boost hydrogen photogeneration performance, *Appl. Catal. B. Environ.*, 272 (2020) 118962.
- [95] X. Wang, W. Mao, J. Zhang, Y. Han, C. Quan, Q. Zhang, T. Yang, J. Yang, X.a. Li, W. Huang, Facile fabrication of highly efficient g-C₃N₄/BiFeO₃ nanocomposites with enhanced visible light photocatalytic activities, *J. Colloid. Interf. Sci.*, 448 (2015) 17-23.
- [96] J. Cao, B. Xu, H. Lin, S. Chen, Highly improved visible light photocatalytic activity of BiPO₄ through fabricating a novel p-n heterojunction BiOI/BiPO₄ nanocomposite, *Chem. Eng. J.*, 228 (2013) 482-488.
- [97] N. Wetchakun, S. Chaiwichain, B. Inceesungvorn, K. Pingmuang, S. Phanichphant, A.I. Minett, J. Chen, BiVO₄/CeO₂ nanocomposites with high visible-light-induced photocatalytic activity, *ACS. Appl. Mater. Inter.*, 4 (2012) 3718-3723.
- [98] D. Liu, W. Yao, J. Wang, Y. Liu, M. Zhang, Y. Zhu, Enhanced visible light photocatalytic performance of a novel heterostructured Bi₄O₅Br₂/Bi₂₄O₃₁Br₁₀/Bi₂SiO₅ photocatalyst, *Appl. Catal. B. Environ.*, 172-173 (2015) 100-107.
- [99] J. Wang, W. Zhang, X. Zhang, F. Wang, Y. Yang, G. Lv, Enhanced photocatalytic ability and easy retrievable photocatalysts of Bi₂WO₆ quantum dots decorated magnetic carbon nano-onions, *J. Alloy. Compd.*, 826 (2020) 154217.
- [100] H. Li, J. Liu, W. Hou, N. Du, R. Zhang, X. Tao, Synthesis and characterization of g-C₃N₄/Bi₂MoO₆ heterojunctions with enhanced visible light photocatalytic activity, *Appl. Catal. B. Environ.*, 160-161 (2014) 89-97.
- [101] Y. Guo, J. Li, Z. Gao, X. Zhu, Y. Liu, Z. Wei, W. Zhao, C. Sun, A simple and effective method for fabricating novel p-n heterojunction photocatalyst g-C₃N₄/Bi₄Ti₃O₁₂ and its photocatalytic performances, *Appl. Catal. B. Environ.*, 192 (2016) 57-71.
- [102] H. Sun, J. Li, G. Zhang, N. Li, Microtetrahedral Bi₁₂TiO₂₀/g-C₃N₄ composite with enhanced visible light photocatalytic activity toward gaseous formaldehyde degradation: facet coupling effect and mechanism study, *J. Mol. Catal. A. Chem.*, 424 (2016) 311-322.
- [103] M. Lv, H. Yang, Y. Xu, Q. Chen, X. Liu, F. Wei, Improving the visible light photocatalytic activities of Bi₂₅FeO₄₀/MIL-101/PTH via polythiophene wrapping, *J. Environ. Chem. Eng.*, 3 (2015) 1003-1008.
- [104] X. Yin, X. Li, H. Liu, W. Gu, W. Zou, L. Zhu, Z. Fu, Y. Lu, Realizing selective water splitting hydrogen/oxygen evolution on ferroelectric Bi₃TiNbO₉ nanosheets, *Nano. Energy.*, 49 (2018) 489-497.
- [105] P. Madhusudan, J. Ran, J. Zhang, J. Yu, G. Liu, Novel urea assisted hydrothermal synthesis of hierarchical BiVO₄/Bi₂O₂CO₃ nanocomposites with enhanced visible-light photocatalytic activity, *Appl. Catal. B. Environ.*, 110 (2011) 286-295.
- [106] M. Yang, Q. Yang, J. Zhong, S. Huang, J. Li, J. Song, C. Burda, Enhanced photocatalytic performance of Ag₂O/BiOF composite photocatalysts originating from efficient interfacial charge separation, *Appl. Surf. Sci.*, 416 (2017) 666-671.

- [107] L. Ye, J. Liu, Z. Jiang, T. Peng, L. Zan, Facets coupling of BiOBr-g-C₃N₄ composite photocatalyst for enhanced visible-light-driven photocatalytic activity, *Appl. Catal. B. Environ.*, 142-143 (2013) 1-7.
- [108] H. Zheng, T. Zhang, Y. Zhu, B. Liang, W. Jiang, KBiO₃ as an effective visible-light-driven photocatalyst: degradation mechanism for different organic pollutants, *ChemPhotoChem.*, 2 (2018) 442-449.
- [109] H. Huang, K. Xiao, Y. He, T. Zhang, F. Dong, X. Du, Y. Zhang, In situ assembly of BiOI@Bi₁₂O₁₇Cl₂ p-n junction: charge induced unique front-lateral surfaces coupling heterostructure with high exposure of BiOI {001} active facets for robust and nonselective photocatalysis, *Appl. Catal. B. Environ.*, 199 (2016) 75-86.
- [110] C. Liu, H. Huang, X. Du, T. Zhang, N. Tian, Y. Guo, Y. Zhang, In situ Co-crystallization for fabrication of g-C₃N₄/Bi₅O₇I heterojunction for enhanced visible-light photocatalysis, *J. Phys. Chem. C.*, 119 (2015) 17156-17165.
- [111] Y. Wang, D. Jung, Synthesis of novel BiOCl/LiBiO₃ p-n heterojunction photocatalysts and their enhanced photocatalytic performance, *Solid. State. Sci.*, 91 (2019) 42-48.
- [112] S. Su, Q. Han, Z. Shen, X. Wang, J. Zhu, Partial decomposition of NaBiO₃ to δ -Bi₂O₃/NaBiO₃ and α -Bi₂O₃/NaBiO₃ heterojunctions in aqueous HAc solution respectively with good adsorption ability and photocatalytic performance, *Mater. Chem. Phys.*, 229 (2019) 6-14.
- [113] F.A. Sofi, K. Majid, O. Mehraj, The visible light driven copper based metal-organic-framework heterojunction: HKUST-1@Ag-Ag₃PO₄ for plasmon enhanced visible light photocatalysis, *J. Alloy. Compd.*, 737 (2018) 798-808.
- [114] R. Liang, F. Jing, L. Shen, N. Qin, L. Wu, MIL-53(Fe) as a highly efficient bifunctional photocatalyst for the simultaneous reduction of Cr(VI) and oxidation of dyes, *J. Hazard. Mater.*, 287 (2015) 364-372.
- [115] F. Jing, R. Liang, J. Xiong, R. Chen, S. Zhang, Y. Li, L. Wu, MIL-68(Fe) as an efficient visible-light-driven photocatalyst for the treatment of a simulated waste-water contain Cr(VI) and Malachite Green, *Appl. Catal. B. Environ.*, 206 (2017) 9-15.
- [116] Y. Wang, Y. Zhang, Z. Jiang, G. Jiang, Z. Zhao, Q. Wu, Y. Liu, Q. Xu, A. Duan, C. Xu, Controlled fabrication and enhanced visible-light photocatalytic hydrogen production of Au@CdS/MIL-101 heterostructure, *Appl. Catal. B. Environ.*, 185 (2016) 307-314.
- [117] S. Miao, H. Zhang, S. Cui, J. Yang, Improved photocatalytic degradation of ketoprofen by Pt/MIL-125(Ti)/Ag with synergetic effect of Pt-MOF and MOF-Ag double interfaces: mechanism and degradation pathway, *Chemosphere.*, 257 (2020) 127123.
- [118] H. Liu, J. Zhang, D. Ao, Construction of heterostructured ZnIn₂S₄@NH₂-MIL-125(Ti) nanocomposites for visible-light-driven H₂ production, *Appl. Catal. B. Environ.*, 221 (2018) 433-442.
- [119] Q. Liang, S. Cui, J. Jin, C. Liu, S. Xu, C. Yao, Z. Li, Fabrication of BiOI@UIO-66(NH₂)@g-C₃N₄ ternary Z-scheme heterojunction with enhanced visible-light photocatalytic activity, *Appl. Surf. Sci.*, 456 (2018) 899-907.
- [120] J. Liu, R. Li, Y. Hu, T. Li, Z. Jia, Y. Wang, Y. Wang, X. Zhang, C. Fan, Harnessing Ag nanofilm as an electrons transfer mediator for enhanced visible light photocatalytic performance of Ag@AgCl/Ag nanofilm/ZIF-8 photocatalyst, *Appl. Catal. B. Environ.*, 202 (2017) 64-71.
- [121] N. Askari, M. Beheshti, D. Mowla, M. Farhadian, Fabrication of CuWO₄/Bi₂S₃/ZIF67 MOF: A novel double Z-scheme ternary heterostructure for boosting visible-light photodegradation

of antibiotics, *Chemosphere.*, 251 (2020) 126453.

[122] M. Alvaro, E. Carbonell, B. Ferrer, F.X. Llabrés i Xamena, H. Garcia, Semiconductor behavior of a metal-organic framework (MOF), *Chem. Eur. J.*, 13 (2007) 5106-5112.

[123] K. Zhao, Z. Zhang, Y. Feng, S. Lin, H. Li, X. Gao, Surface oxygen vacancy modified $\text{Bi}_2\text{MoO}_6/\text{MIL-88B}(\text{Fe})$ heterostructure with enhanced spatial charge separation at the bulk & interface, *Appl. Catal. B. Environ.*, 268 (2020) 118740.

[124] W. Huang, C. Jing, X. Zhang, M. Tang, L. Tang, M. Wu, N. Liu, Integration of plasmonic effect into spindle-shaped MIL-88A(Fe): Steering charge flow for enhanced visible-light photocatalytic degradation of ibuprofen, *Chem. Eng. J.*, 349 (2018) 603-612.

[125] J. Liu, R. Li, X. Zu, X. Zhang, Y. Wang, Y. Wang, C. Fan, Photocatalytic conversion of nitrogen to ammonia with water on triphase interfaces of hydrophilic-hydrophobic composite $\text{Bi}_4\text{O}_5\text{Br}_2/\text{ZIF-8}$, *Chem. Eng. J.*, 371 (2019) 796-803.

[126] Y.-H. Ding, X.-L. Zhang, N. Zhang, J.-Y. Zhang, R. Zhang, Y.-F. Liu, Y.-Z. Fang, A visible-light driven $\text{Bi}_2\text{S}_3/\text{ZIF-8}$ core-shell heterostructure and synergistic photocatalysis mechanism, *Dalton. T.*, 47 (2018) 684-692.

[127] Y.-H. Si, Y.-Y. Li, Y. Xia, S.-K. Shang, X.-B. Xiong, X.-R. Zeng, J. Zhou, Fabrication of novel $\text{ZIF-8}/\text{BiVO}_4$ composite with enhanced photocatalytic performance, *Crystals.*, 8 (2018) 432.

[128] Y. Xia, S.-K. Shang, X.-R. Zeng, J. Zhou, Y.-Y. Li, A novel $\text{Bi}_2\text{MoO}_6/\text{ZIF-8}$ composite for enhanced visible light photocatalytic activity, *Nanomaterials. Basel.*, 9 (2019) 545.

[129] C. Cheng, J. Fang, S. Lu, C. Cen, Y. Chen, L. Ren, W. Feng, Z. Fang, Zirconium metal-organic framework supported highly-dispersed nanosized BiVO_4 for enhanced visible-light photocatalytic applications, *J. Chem. Technol. Biot.*, 91 (2016) 2785-2792.

[130] J. Ding, Z. Yang, C. He, X. Tong, Y. Li, X. Niu, H. Zhang, $\text{UiO-66}(\text{Zr})$ coupled with Bi_2MoO_6 as photocatalyst for visible-light promoted dye degradation, *J. Colloid. Interf. Sci.*, 497 (2017) 126-133.

[131] Z. Sha, J. Sun, H.S. On Chan, S. Jaenicke, J. Wu, Bismuth tungstate incorporated zirconium metal-organic framework composite with enhanced visible-light photocatalytic performance, *RSC. Adv.*, 4 (2014) 64977-64984.

[132] Y. Xue, P. Wang, C. Wang, Y. Ao, Efficient degradation of atrazine by $\text{BiOBr}/\text{UiO-66}$ composite photocatalyst under visible light irradiation: environmental factors, mechanisms and degradation pathways, *Chemosphere.*, 203 (2018) 497-505.

[133] Z. Sha, J. Wu, Enhanced visible-light photocatalytic performance of $\text{BiOBr}/\text{UiO-66}(\text{Zr})$ composite for dye degradation with the assistance of UiO-66 , *RSC. Adv.*, 5 (2015) 39592-39600.

[134] Y. Li, X. Shang, C. Li, X. Huang, J. Zheng, Novel p-n junction $\text{UiO-66}/\text{BiOI}$ photocatalysts with efficient visible-light-induced photocatalytic activity, *Water. Sci. Technol.*, 77 (2018) 1441-1448.

[135] X. Tong, Z. Yang, J. Feng, Y. Li, H. Zhang, $\text{BiOCl}/\text{UiO-66}$ composite with enhanced performance for photo-assisted degradation of dye from water, *Appl. Organomet. Chem.*, 32 (2018) e4049.

[136] Z. Yang, X. Tong, J. Feng, S. He, M. Fu, X. Niu, T. Zhang, H. Liang, A. Ding, X. Feng, Flower-like $\text{BiOBr}/\text{UiO-66-NH}_2$ nanosphere with improved photocatalytic property for norfloxacin removal, *Chemosphere.*, 220 (2019) 98-106.

[137] Q. Hu, Y. Chen, M. Li, Y. Zhang, B. Wang, Y. Zhao, J. Xia, S. Yin, H. Li, Construction of $\text{NH}_2\text{-UiO-66}/\text{BiOBr}$ composites with boosted photocatalytic activity for the removal of

contaminants, *Colloid. Surface. A.*, 579 (2019) 123625.

[138] R. Bibi, Q. Shen, L. Wei, D. Hao, N. Li, J. Zhou, Hybrid BiOBr/Uio-66-NH₂ composite with enhanced visible-light driven photocatalytic activity toward RhB dye degradation, *RSC. Adv.*, 8 (2018) 2048-2058.

[139] Y. Liu, Y. Zhou, Q. Tang, Q. Li, S. Chen, Z. Sun, H. Wang, A direct Z-scheme Bi₂WO₆/NH₂-Uio-66 nanocomposite as an efficient visible-light-driven photocatalyst for NO removal, *RSC. Adv.*, 10 (2020) 1757-1768.

[140] X. Zhang, H. Zhou, W. Cao, C. Chen, C. Jiang, Y. Wang, Preparation and mechanism investigation of Bi₂WO₆/Uio-66-NH₂ Z-scheme heterojunction with enhanced visible light catalytic activity, *Inorg. Chem. Commun.*, 120 (2020) 108162.

[141] Z. Yang, J. Ding, J. Feng, C. He, Y. Li, X. Tong, X. Niu, H. Zhang, Preparation of BiVO₄/MIL-125(Ti) composite with enhanced visible-light photocatalytic activity for dye degradation, *Appl. Organomet. Chem.*, 32 (2018) e4285.

[142] P.V. Hlophe, L.C. Mahlalela, L.N. Dlamini, A composite of platelet-like orientated BiVO₄ fused with MIL-125(Ti): synthesis and characterization, *Sci. Rep. UK.*, 9 (2019) 10044.

[143] W. Jiang, Z. Li, C. Liu, D. Wang, G. Yan, B. Liu, G. Che, Enhanced visible-light-induced photocatalytic degradation of tetracycline using BiOI/MIL-125(Ti) composite photocatalyst, *J. Alloy. Compd.*, 854 (2021) 157166.

[144] S. Zhang, M. Du, J. Kuang, Z. Xing, Z. Li, K. Pan, Q. Zhu, W. Zhou, Surface-defect-rich mesoporous NH₂-MIL-125 (Ti)@Bi₂MoO₆ core-shell heterojunction with improved charge separation and enhanced visible-light-driven photocatalytic performance, *J. Colloid. Interf. Sci.*, 554 (2019) 324-334.

[145] S. Yin, Y. Chen, M. Li, Q. Hu, Y. Ding, Y. Shao, J. Di, J. Xia, H. Li, Construction of NH₂-MIL-125(Ti)/Bi₂WO₆ composites with accelerated charge separation for degradation of organic contaminants under visible light irradiation, *Green. Energy. Environ.*, 391 (2020) 123601.

[146] S. Yin, Y. Chen, Q. Hu, M. Li, Y. Ding, J. Di, J. Xia, H. Li, Construction of NH₂-MIL-125(Ti) nanoplates modified Bi₂WO₆ microspheres with boosted visible-light photocatalytic activity, *Res. Chem. Intermediat.*, 46 (2020) 3311–3326.

[147] M. Wang, L. Yang, J. Yuan, L. He, Y. Song, H. Zhang, Z. Zhang, S. Fang, Heterostructured Bi₂S₃@NH₂-MIL-125(Ti) nanocomposite as a bifunctional photocatalyst for Cr(VI) reduction and Rhodamine B degradation under visible light, *RSC. Adv.*, 8 (2018) 12459-12470.

[148] S.-R. Zhu, P.-F. Liu, M.-K. Wu, W.-N. Zhao, G.-C. Li, K. Tao, F.-Y. Yi, L. Han, Enhanced photocatalytic performance of BiOBr/NH₂-MIL-125(Ti) composite for dye degradation under visible light, *Dalton. T.*, 45 (2016) 17521-17529.

[149] Q. Hu, J. Di, B. Wang, M. Ji, Y. Chen, J. Xia, H. Li, Y. Zhao, In-situ preparation of NH₂-MIL-125(Ti)/BiOCl composite with accelerating charge carriers for boosting visible light photocatalytic activity, *Appl. Surf. Sci.*, 466 (2019) 525-534.

[150] L. Han, X. Zhang, D. Wu, Construction and characterization of BiOI/NH₂-MIL-125(Ti) heterostructures with excellent visible-light photocatalytic activity, *J. Mater. Sci. Mater. El.*, 30 (2019) 3773-3781.

[151] L. Tang, Z.-Q. Lv, Y.-C. Xue, L. Xu, W.-H. Qiu, C.-M. Zheng, W.-Q. Chen, M.-H. Wu, MIL-53(Fe) incorporated in the lamellar BiOBr: promoting the visible-light catalytic capability on the degradation of Rhodamine B and carbamazepine, *Chem. Eng. J.*, 374 (2019) 975-982.

- [152] S. Miao, Z. Zha, Y. Li, X. Geng, J. Yang, S. Cui, J. Yang, Visible-light-driven MIL-53(Fe)/BiOCl composite assisted by persulfate: photocatalytic performance and mechanism, *J. Photoch. Photobio. A.*, 380 (2019) 111862.
- [153] N. Zhou, J. Tan, X. Li, L. Wang, C. Jin, M. Chen, Z. Yu, Y. Liang, Z. Qiu, W. Li, Y. Dong, Z. Xie, Y. Lin, D. Qu, C. Zhang, Fabrication of Z-scheme Bi₅O₇I/MIL-53(Fe) hybrid with improved photocatalytic performance under visible light irradiation, *J. Mater. Sci. Mater. El.*, 31 (2020) 4822-4835.
- [154] Q. Zhang, J.-B. Liu, L. Chen, C.-X. Xiao, P. Chen, S. Shen, J.-K. Guo, C.-T. Au, S.-F. Yin, An etching and re-growth method for the synthesis of bismuth ferrite/MIL-53(Fe) nanocomposite as efficient photocatalyst for selective oxidation of aromatic alcohols, *Appl. Catal. B. Environ.*, 264 (2020) 118529.
- [155] Y. Tu, L. Ling, Q. Li, X. Long, N. Liu, Z. Li, Greatly enhanced photocatalytic activity over Bi₂WO₆ by MIL-53(Fe) modification, *Opt. Mater.*, 110 (2020) 110500.
- [156] Y. Cui, L.-c. Nengzi, J. Gou, Y. Huang, B. Li, X. Cheng, Fabrication of dual Z-scheme MIL-53(Fe)/ α -Bi₂O₃/g-C₃N₄ ternary composite with enhanced visible light photocatalytic performance, *Sep. Purif. Technol.*, 232 (2020) 115959.
- [157] S. Gholizadeh Khasevani, M.R. Gholami, Evaluation of the reaction mechanism for photocatalytic degradation of organic pollutants with MIL-88A/BiOI structure under visible light irradiation, *Res. Chem. Intermediat.*, 45 (2019) 1341-1356.
- [158] S. Gholizadeh Khasevani, M.R. Gholami, Engineering a highly dispersed core@shell structure for efficient photocatalysis: a case study of ternary novel BiOI@MIL-88A(Fe)@g-C₃N₄ nanocomposite, *Mater. Res. Bull.*, 106 (2018) 93-102.
- [159] M. Jahurul Islam, H.K. Kim, D. Amaranatha Reddy, Y. Kim, R. Ma, H. Baek, J. Kim, T.K. Kim, Hierarchical BiOI nanostructures supported on a metal organic framework as efficient photocatalysts for degradation of organic pollutants in water, *Dalton. T.*, 46 (2017) 6013-6023.
- [160] S.G. Khasevani, M.R. Gholami, Synthesis of BiOI/ZnFe₂O₄-Metal-Organic Framework and g-C₃N₄-based nanocomposites for applications in photocatalysis, *Ind. Eng. Chem. Res.*, 58 (2019) 9806-9818.
- [161] S. Gholizadeh Khasevani, N. Mohaghegh, M.R. Gholami, Kinetic study of navy blue photocatalytic degradation over Ag₃PO₄/BiPO₄@MIL-88B(Fe)@g-C₃N₄ core@shell nanocomposite under visible light irradiation, *New. J. Chem.*, 41 (2017) 10390-10396.
- [162] Q. Han, Y. Dong, C. Xu, Q. Hu, C. Dong, X. Liang, Y. Ding, Immobilization of metal-organic framework MIL-100(Fe) on the surface of BiVO₄: a new platform for enhanced visible-light-driven water oxidation, *ACS. Appl. Mater. Inter.*, 12 (2020) 10410-10419.
- [163] S. Abdpour, E. Kowsari, M.R. Alavi Moghaddam, L. Schmolke, C. Janiak, Mil-100(Fe) nanoparticles supported on urchin like Bi₂S₃ structure for improving photocatalytic degradation of Rhodamine-B dye under visible light irradiation, *J. Solid. State. Chem.*, 266 (2018) 54-62.
- [164] J. Zheng, Z. Jiao, Modified Bi₂WO₆ with metal-organic frameworks for enhanced photocatalytic activity under visible light, *J. Colloid. Interf. Sci.*, 488 (2017) 234-239.
- [165] J. Yang, X. Niu, S. An, W. Chen, J. Wang, W. Liu, Facile synthesis of Bi₂MoO₆-MIL-100(Fe) metal-organic framework composites with enhanced photocatalytic performance, *RSC. Adv.*, 7 (2017) 2943-2952.
- [166] C. Zhao, J. Wang, X. Chen, Z. Wang, H. Ji, L. Chen, W. Liu, C.-C. Wang, Bifunctional Bi₁₂O₁₇Cl₂/MIL-100(Fe) composites toward photocatalytic Cr(VI) sequestration and activation of

persulfate for bisphenol a degradation, *Sci. Total Environ.*, 752 (2021) 141901.

[167] W. Guo, Z. Chen, C. Yang, T. Neumann, C. Kübel, W. Wenzel, A. Welle, W. Pfleging, O. Shekhah, C. Wöll, E. Redel, Bi_2O_3 nanoparticles encapsulated in surface mounted metal–organic framework thin films, *Nanoscale.*, 8 (2016) 6468-6472.

[168] S. Mosleh, M.R. Rahimi, M. Ghaedi, K. Dashtian, HKUST-1-MOF– BiVO_4 hybrid as a new sonophotocatalyst for simultaneous degradation of disulfine blue and rose bengal dyes: optimization and statistical modelling, *RSC. Adv.*, 6 (2016) 61516-61527.

[169] S. Mosleh, M.R. Rahimi, M. Ghaedi, K. Dashtian, S. Hajati, $\text{BiPO}_4/\text{Bi}_2\text{S}_3$ -HKUST-1-MOF as a novel blue light-driven photocatalyst for simultaneous degradation of toluidine blue and auramine-O dyes in a new rotating packed bed reactor: optimization and comparison to a conventional reactor, *RSC. Adv.*, 6 (2016) 63667-63680.

[170] S. Mosleh, M.R. Rahimi, M. Ghaedi, K. Dashtian, Sonophotocatalytic degradation of trypan blue and vesuvine dyes in the presence of blue light active photocatalyst of $\text{Ag}_3\text{PO}_4/\text{Bi}_2\text{S}_3$ -HKUST-1-MOF: Central composite optimization and synergistic effect study, *Ultrason. Sonochem.*, 32 (2016) 387-397.

[171] H.-M. Yang, X. Liu, X.-L. Song, T.-L. Yang, Z.-H. Liang, C.-M. Fan, In situ electrochemical synthesis of MOF-5 and its application in improving photocatalytic activity of BiOBr , *T. Nonferr. Metal. Soc.*, 25 (2015) 3987-3994.

[172] Y. Xu, M. Lv, H. Yang, Q. Chen, X. Liu, W. Fengyu, $\text{BiVO}_4/\text{MIL}-101$ composite having the synergistically enhanced visible light photocatalytic activity, *RSC. Adv.*, 5 (2015) 43473-43479.

[173] H. Ramezanalizadeh, F. Manteghi, Immobilization of mixed cobalt/nickel metal-organic framework on a magnetic BiFeO_3 : A highly efficient separable photocatalyst for degradation of water pollutions, *J. Photoch. Photobio. A.*, 346 (2017) 89-104.

[174] Y.-Y. Zheng, C.-X. Li, X.-T. Ding, Q. Yang, Y.-M. Qi, H.-M. Zhang, L.-T. Qu, Detection of dopamine at graphene-ZIF-8 nanocomposite modified electrode, *Chin. Chem. Lett.*, 28 (2017) 1473-1478.

[175] N. Li, L. Zhou, X. Jin, G. Owens, Z. Chen, Simultaneous removal of tetracycline and oxytetracycline antibiotics from wastewater using a ZIF-8 metal organic-framework, *J. Hazard. Mater.*, 366 (2019) 563-572.

[176] K.S. Park, Z. Ni, A.P. Côté, J.Y. Choi, R. Huang, F.J. Uribe-Romo, H.K. Chae, M. O’Keeffe, O.M. Yaghi, Exceptional chemical and thermal stability of zeolitic imidazolate frameworks, *P. Natl. Acad. Sci. USA.*, 103 (2006) 10186-10191.

[177] Q. Song, S.K. Nataraj, M.V. Roussanova, J.C. Tan, D.J. Hughes, W. Li, P. Bourgoign, M.A. Alam, A.K. Cheetham, S.A. Al-Muhtaseb, E. Sivaniah, Zeolitic imidazolate framework (ZIF-8) based polymer nanocomposite membranes for gas separation, *Energ. Environ. Sci.*, 5 (2012) 8359-8369.

[178] D. Liu, X. Ma, H. Xi, Y.S. Lin, Gas transport properties and propylene/propane separation characteristics of ZIF-8 membranes, *J. Membrane. Sci.*, 451 (2014) 85-93.

[179] S. Hwang, W.S. Chi, S.J. Lee, S.H. Im, J.H. Kim, J. Kim, Hollow ZIF-8 nanoparticles improve the permeability of mixed matrix membranes for CO_2/CH_4 gas separation, *J. Membrane. Sci.*, 480 (2015) 11-19.

[180] J. Zhuang, C.-H. Kuo, L.-Y. Chou, D.-Y. Liu, E. Weerapana, C.-K. Tsung, Optimized metal–organic-framework nanospheres for drug delivery: evaluation of small-molecule encapsulation, *ACS. Nano.*, 8 (2014) 2812-2819.

- [181] C.-Y. Sun, C. Qin, X.-L. Wang, G.-S. Yang, K.-Z. Shao, Y.-Q. Lan, Z.-M. Su, P. Huang, C.-G. Wang, E.-B. Wang, Zeolitic imidazolate framework-8 as efficient pH-sensitive drug delivery vehicle, *Dalton. T.*, 41 (2012) 6906-6909.
- [182] D.-Z. Shen, T.-T. Cai, X.-L. Zhu, X.-L. Ma, L.-Q. Kong, Q. Kang, Monitoring iodine adsorption onto zeolitic-imidazolate framework-8 film using a separated-electrode piezoelectric sensor, *Chin. Chem. Lett.*, 26 (2015) 1022-1025.
- [183] G. Lu, J.T. Hupp, Metal-organic frameworks as sensors: a ZIF-8 based fabry-pérot device as a selective sensor for chemical vapors and gases, *J. Am. Chem. Soc.*, 132 (2010) 7832-7833.
- [184] H.-P. Jing, C.-C. Wang, Y.-W. Zhang, P. Wang, R. Li, Photocatalytic degradation of methylene blue in ZIF-8, *RSC. Adv.*, 4 (2014) 54454-54462.
- [185] Y.-H. Si, Y.-Y. Li, Y. Xia, S.-K. Shang, X.-B. Xiong, X.-R. Zeng, J. Zhou, Fabrication of novel ZIF-8@BiVO₄ composite with enhanced photocatalytic performance, *Crystals.*, 8 (2018) 432-441.
- [186] N. Zhang, A. Jalil, D. Wu, S. Chen, Y. Liu, C. Gao, W. Ye, Z. Qi, H. Ju, C. Wang, X. Wu, L. Song, J. Zhu, Y. Xiong, Refining defect states in W₁₈O₄₉ by Mo doping: a strategy for tuning N₂ activation towards solar-driven nitrogen fixation, *J. Am. Chem. Soc.*, 140 (2018) 9434-9443.
- [187] X. Chen, N. Li, Z. Kong, W.-J. Ong, X. Zhao, Photocatalytic fixation of nitrogen to ammonia: state-of-the-art advancements and future prospects, *Mater. Horiz.*, 5 (2018) 9-27.
- [188] X. Lv, W. Wei, F. Li, B. Huang, Y. Dai, Metal-free B@g-CN: visible/infrared light-driven single atom photocatalyst enables spontaneous dinitrogen reduction to ammonia, *Nano. Lett.*, 19 (2019) 6391-6399.
- [189] H. Huang, X.-S. Wang, D. Philo, F. Ichihara, H. Song, Y. Li, D. Li, T. Qiu, S. Wang, J. Ye, Toward visible-light-assisted photocatalytic nitrogen fixation: a titanium metal organic framework with functionalized ligands, *Appl. Catal. B. Environ.*, 267 (2020) 118686.
- [190] G. Li, F. Li, J. Liu, C. Fan, Fe-based MOFs for photocatalytic N₂ reduction: key role of transition metal iron in nitrogen activation, *J. Solid. State. Chem.*, 285 (2020) 121245.
- [191] S. Wang, X. Hai, X. Ding, K. Chang, Y. Xiang, X. Meng, Z. Yang, H. Chen, J. Ye, Light-switchable oxygen vacancies in ultrafine Bi₅O₇Br nanotubes for boosting solar-driven nitrogen fixation in pure water, *Adv. Mater.*, 29 (2017) 1701774.
- [192] Y. Bai, L. Ye, T. Chen, L. Wang, X. Shi, X. Zhang, D. Chen, Facet-dependent photocatalytic N₂ fixation of Bismuth-rich Bi₅O₇I Nanosheets, *ACS. Appl. Mater. Inter.*, 8 (2016) 27661-27668.
- [193] H. Li, J. Shang, Z. Ai, L. Zhang, Efficient visible light nitrogen fixation with BiOBr nanosheets of oxygen vacancies on the exposed {001} facets, *J. Am. Chem. Soc.*, 137 (2015) 6393-6399.
- [194] H. Li, J. Shang, J. Shi, K. Zhao, L. Zhang, Facet-dependent solar ammonia synthesis of BiOCl nanosheets via a proton-assisted electron transfer pathway, *Nanoscale.*, 8 (2016) 1986-1993.
- [195] J. Li, G. Chen, Y. Zhu, Z. Liang, A. Pei, C.-L. Wu, H. Wang, H.R. Lee, K. Liu, S. Chu, Y. Cui, Efficient electrocatalytic CO₂ reduction on a three-phase interface, *Nat. Catal.*, 1 (2018) 592-600.
- [196] X. Sheng, Z. Liu, R. Zeng, L. Chen, X. Feng, L. Jiang, Enhanced photocatalytic reaction at air-liquid-solid joint interfaces, *J. Am. Chem. Soc.*, 139 (2017) 12402-12405.
- [197] S. Sun, X. Li, W. Wang, L. Zhang, X. Sun, Photocatalytic robust solar energy reduction

- of dinitrogen to ammonia on ultrathin MoS₂, *Appl. Catal. B. Environ.*, 200 (2017) 323-329.
- [198] G.N. Schrauzer, T.D. Guth, Photolysis of water and photoreduction of nitrogen on titanium dioxide, *J. Am. Chem. Soc.*, 99 (1977) 7189-7193.
- [199] K.T. Ranjit, T.K. Varadarajan, B. Viswanathan, Photocatalytic reduction of dinitrogen to ammonia over noble-metal-loaded TiO₂, *J. Photoch. Photobio. A.*, 96 (1996) 181-185.
- [200] L. Ye, C. Han, Z. Ma, Y. Leng, J. Li, X. Ji, D. Bi, H. Xie, Z. Huang, Ni₂P loading on Cd_{0.5}Zn_{0.5}S solid solution for exceptional photocatalytic nitrogen fixation under visible light, *Chem. Eng. J.*, 307 (2017) 311-318.
- [201] H. Li, J. Shang, Z. Ai, L. Zhang, Correction to “efficient visible light nitrogen fixation with BiOBr nanosheets of oxygen vacancies on the exposed {001} facets”, *J. Am. Chem. Soc.*, 140 (2018) 526-526.
- [202] X. Li, W. Wang, D. Jiang, S. Sun, L. Zhang, X. Sun, Efficient solar-driven nitrogen fixation over carbon–tungstic-acid hybrids, *Chem. Eur. J.*, 22 (2016) 13819-13822.
- [203] L. Li, Y. Wang, S. Vanka, X. Mu, Z. Mi, C.-J. Li, Nitrogen photofixation over III-Nitride nanowires assisted by ruthenium clusters of low atomicity, *Angew. Chem. Int. Edit.*, 56 (2017) 8701-8705.
- [204] B. Shao, X. Liu, Z. Liu, G. Zeng, Q. Liang, C. Liang, Y. Cheng, W. Zhang, Y. Liu, S. Gong, A novel double Z-scheme photocatalyst Ag₃PO₄/Bi₂S₃/Bi₂O₃ with enhanced visible-light photocatalytic performance for antibiotic degradation, *Chem. Eng. J.*, 368 (2019) 730-745.
- [205] J. Liu, X. Zheng, L. Yan, L. Zhou, G. Tian, W. Yin, L. Wang, Y. Liu, Z. Hu, Z. Gu, C. Chen, Y. Zhao, Bismuth sulfide nanorods as a precision nanomedicine for in vivo multimodal imaging-guided photothermal therapy of tumor, *ACS. Nano.*, 9 (2015) 696-707.
- [206] A. Helal, F.A. Harraz, A.A. Ismail, T.M. Sami, I.A. Ibrahim, Hydrothermal synthesis of novel heterostructured Fe₂O₃/Bi₂S₃ nanorods with enhanced photocatalytic activity under visible light, *Appl. Catal. B. Environ.*, 213 (2017) 18-27.
- [207] A.J. MacLachlan, F.T.F. O'Mahony, A.L. Sudlow, M.S. Hill, K.C. Molloy, J. Nelson, S.A. Haque, Solution-processed mesoscopic Bi₂S₃:polymer photoactive layers, *ChemPhysChem.*, 15 (2014) 1019-1023.
- [208] H. Jia, W. He, W.G. Wamer, X. Han, B. Zhang, S. Zhang, Z. Zheng, Y. Xiang, J.-J. Yin, Generation of reactive oxygen species, electrons/holes, and photocatalytic degradation of Rhodamine B by photoexcited CdS and Ag₂S micro-nano structures, *J. Phys. Chem. C.*, 118 (2014) 21447-21456.
- [209] J.H. Cavka, S. Jakobsen, U. Olsbye, N. Guillou, C. Lamberti, S. Bordiga, K.P. Lillerud, A new Zirconium inorganic building brick forming metal organic frameworks with exceptional stability, *J. Am. Chem. Soc.*, 130 (2008) 13850-13851.
- [210] Y. Bai, Y. Dou, L.-H. Xie, W. Rutledge, J.-R. Li, H.-C. Zhou, Zr-based metal–organic frameworks: design, synthesis, structure, and applications, *Chem. Soc. Rev.*, 45 (2016) 2327-2367.
- [211] Z. Hasan, N.A. Khan, S.H. Jhung, Adsorptive removal of diclofenac sodium from water with Zr-based metal–organic frameworks, *Chem. Eng. J.*, 284 (2016) 1406-1413.
- [212] Y. Feng, Q. Chen, M. Jiang, J. Yao, Tailoring the properties of UiO-66 through defect engineering: a review, *Ind. Eng. Chem. Res.*, 58 (2019) 17646-17659.
- [213] Y.-P. Yuan, L.-S. Yin, S.-W. Cao, G.-S. Xu, C.-H. Li, C. Xue, Improving photocatalytic hydrogen production of metal–organic framework UiO-66 octahedrons by dye-sensitization, *Appl. Catal. B. Environ.*, 168-169 (2015) 572-576.

- [214] S. Pu, L. Xu, L. Sun, H. Du, Tuning the optical properties of the Zirconium–UiO-66 metal–organic framework for photocatalytic degradation of methyl orange, *Inorg. Chem. Commun.*, 52 (2015) 50-52.
- [215] X. Mu, J. Jiang, F. Chao, Y. Lou, J. Chen, Ligand modification of UiO-66 with an unusual visible light photocatalytic behavior for RhB degradation, *Dalton. T.*, 47 (2018) 1895-1902.
- [216] H. Wu, Y.S. Chua, V. Krungleviciute, M. Tyagi, P. Chen, T. Yildirim, W. Zhou, Unusual and highly tunable missing-linker defects in Zirconium metal–organic framework UiO-66 and their important effects on gas adsorption, *J. Am. Chem. Soc.*, 135 (2013) 10525-10532.
- [217] M.W. Anjum, F. Vermoortele, A.L. Khan, B. Bueken, D.E. De Vos, I.F.J. Vankelecom, Modulated UiO-66-based mixed-matrix membranes for CO₂ separation, *ACS. Appl. Mater. Inter.*, 7 (2015) 25193-25201.
- [218] Y. Lee, S. Kim, J.K. Kang, S.M. Cohen, Photocatalytic CO₂ reduction by a mixed metal (Zr/Ti), mixed ligand metal–organic framework under visible light irradiation, *Chem. Commun.*, 51 (2015) 5735-5738.
- [219] K. Hendrickx, D.E.P. Vanpoucke, K. Leus, K. Lejaeghere, A. Van Yperen-De Deyne, V. Van Speybroeck, P. Van Der Voort, K. Hemelsoet, Understanding intrinsic light absorption properties of UiO-66 frameworks: a combined theoretical and experimental study, *Inorg. Chem.*, 54 (2015) 10701-10710.
- [220] C. Gomes Silva, I. Luz, F.X. Llabrés i Xamena, A. Corma, H. García, Water stable Zr–Benzenedicarboxylate metal–organic frameworks as photocatalysts for Hydrogen generation, *Chem. Eur. J.*, 16 (2010) 11133-11138.
- [221] L. Shen, R. Liang, M. Luo, F. Jing, L. Wu, Electronic effects of ligand substitution on metal–organic framework photocatalysts: the case study of UiO-66, *Phys. Chem. Chem. Phys.*, 17 (2015) 117-121.
- [222] Y.-X. Li, Y.-C. Han, C.-C Wang, Fabrication strategies and Cr(VI) elimination activities of the MOF-derivatives and their composites, *Chem. Eng. J.*, 405 (2021) 126648.
- [223] D. Sun, Y. Fu, W. Liu, L. Ye, D. Wang, L. Yang, X. Fu, Z. Li, Studies on photocatalytic CO₂ reduction over NH₂-UiO-66(Zr) and its derivatives: towards a better understanding of photocatalysis on metal–organic frameworks, *Chem. Eur. J.*, 19 (2013) 14279-14285.
- [224] Y.C. Zhou, C.-C. Wang, P. Wang, H.F. Fu, C. Zhao, In-situ photochemical reduction of Ag-UiO-66-NH₂ composite for enhanced photocatalytic performance, *Chin. J. Inorgan. Chem.*, 36 (2020) 2100-2112.
- [225] J. Xu, L. Li, C. Guo, Y. Zhang, S. Wang, Removal of benzotriazole from solution by BiOBr photocatalysis under simulated solar irradiation, *Chem. Eng. J.*, 221 (2013) 230-237.
- [226] J. Xu, W. Meng, Y. Zhang, L. Li, C. Guo, Photocatalytic degradation of tetrabromobisphenol A by mesoporous BiOBr: Efficacy, products and pathway, *Appl. Catal. B. Environ.*, 107 (2011) 355-362.
- [227] Y. Huo, J. Zhang, M. Miao, Y. Jin, Solvothermal synthesis of flower-like BiOBr microspheres with highly visible-light photocatalytic performances, *Appl. Catal. B. Environ.*, 111-112 (2012) 334-341.
- [228] X.-J. Wang, W.-Y. Yang, F.-T. Li, J. Zhao, R.-H. Liu, S.-J. Liu, B. Li, Construction of amorphous TiO₂/BiOBr heterojunctions via facets coupling for enhanced photocatalytic activity, *J. Hazard. Mater.*, 292 (2015) 126-136.
- [229] W. Zhang, Y. Li, Y. Su, K. Mao, Q. Wang, Effect of water composition on TiO₂

photocatalytic removal of endocrine disrupting compounds (EDCs) and estrogenic activity from secondary effluent, *J. Hazard. Mater.*, 215-216 (2012) 252-258.

[230] N.S. Alkayal, M.A. Hussein, Photocatalytic degradation of atrazine under visible light using novel Ag@Mg₄Ta₂O₉ nanocomposites, *Sci. Rep. UK.*, 9 (2019) 7470.

[231] Y. Zheng, F. Duan, M. Chen, Y. Xie, Synthetic Bi₂O₂CO₃ nanostructures: novel photocatalyst with controlled special surface exposed, *J. Mol. Catal. A. Chem.*, 317 (2010) 34-40.

[232] H. Li, G. Liu, X. Duan, Monoclinic BiVO₄ with regular morphologies: hydrothermal synthesis, characterization and photocatalytic properties, *Mater. Chem. Phys.*, 115 (2009) 9-13.

[233] Y. Guo, H. Huang, Y. He, N. Tian, T. Zhang, P.K. Chu, Q. An, Y. Zhang, In situ crystallization for fabrication of a core-satellite structured BiOBr-CdS heterostructure with excellent visible-light-responsive photoreactivity, *Nanoscale.*, 7 (2015) 11702-11711.

[234] Z. Liu, B. Wu, D. Xiang, Y. Zhu, Effect of solvents on morphology and photocatalytic activity of BiOBr synthesized by solvothermal method, *Mater. Res. Bull.*, 47 (2012) 3753-3757.

[235] J. Tang, R. Wang, M. Liu, Z. Zhang, Y. Song, S. Xue, Z. Zhao, D.D. Dionysiou, Construction of novel Z-scheme Ag/FeTiO₃/Ag/BiFeO₃ photocatalyst with enhanced visible-light-driven photocatalytic performance for degradation of norfloxacin, *Chem. Eng. J.*, 351 (2018) 1056-1066.

[236] S. Subudhi, L. Paramanik, S. Sultana, S. Mansingh, P. Mohapatra, K. Parida, A type-II interband alignment heterojunction architecture of cobalt titanate integrated UiO-66-NH₂: a visible light mediated photocatalytic approach directed towards norfloxacin degradation and green energy (hydrogen) evolution, *J. Colloid. Interf. Sci.*, 568 (2020) 89-105.

[237] X. Zhang, X. Wang, J. Chai, S. Xue, R. Wang, L. Jiang, J. Wang, Z. Zhang, D.D. Dionysiou, Construction of novel symmetric double Z-scheme BiFeO₃/CuBi₂O₄/BaTiO₃ photocatalyst with enhanced solar-light-driven photocatalytic performance for degradation of norfloxacin, *Appl. Catal. B. Environ.*, 272 (2020) 119017.

[238] J. Tian, Z. Chen, X. Deng, Q. Sun, Z. Sun, W. Li, Improving visible light driving degradation of norfloxacin over core-shell hierarchical BiOCl microspherical photocatalyst by synergistic effect of oxygen vacancy and nanostructure, *Appl. Surf. Sci.*, 453 (2018) 373-382.

[239] M. Xu, M. Ye, X. Zhou, J. Cheng, C. Huang, W. Wong, Z. Wang, Y. Wang, C. Li, One-pot controllable synthesis of BiOBr/ β -Bi₂O₃ nanocomposites with enhanced photocatalytic degradation of norfloxacin under simulated solar irradiation, *J. Alloy. Compd.*, 816 (2020) 152664.

[240] X. Ma, Z. Ma, T. Liao, X. Liu, Y. Zhang, L. Li, W. Li, B. Hou, Preparation of BiVO₄/BiOCl heterojunction photocatalyst by in-situ transformation method for norfloxacin photocatalytic degradation, *J. Alloy. Compd.*, 702 (2017) 68-74.

[241] J. Bai, Y. Li, P. Jin, J. Wang, L. Liu, Facile preparation 3D ZnS nanospheres-reduced graphene oxide composites for enhanced photodegradation of norfloxacin, *J. Alloy. Compd.*, 729 (2017) 809-815.

[242] W. Liu, J. Zhou, J. Yao, Shuttle-like CeO₂/g-C₃N₄ composite combined with persulfate for the enhanced photocatalytic degradation of norfloxacin under visible light, *Ecotox. Environ. Safe.*, 190 (2020) 110062.

[243] X.-J. Wen, C.-G. Niu, D.-W. Huang, L. Zhang, C. Liang, G.-M. Zeng, Study of the photocatalytic degradation pathway of norfloxacin and mineralization activity using a novel ternary Ag/AgCl-CeO₂ photocatalyst, *J. Catal.*, 355 (2017) 73-86.

[244] C. Liang, H. Guo, L. Zhang, M. Ruan, C.-G. Niu, H.-P. Feng, X.-J. Wen, N. Tang, H.-Y.

Liu, G.-M. Zeng, Boosting molecular oxygen activation ability in self-assembled plasmonic p-n semiconductor photocatalytic heterojunction of $\text{WO}_3/\text{Ag}@\text{Ag}_2\text{O}$, *Chem. Eng. J.*, 372 (2019) 12-25.

[245] H. Liu, W. Cao, Y. Su, Y. Wang, X. Wang, Synthesis, characterization and photocatalytic performance of novel visible-light-induced Ag/BiOI , *Appl. Catal. B. Environ.*, 111-112 (2012) 271-279.

[246] W. Fan, H. Li, F. Zhao, X. Xiao, Y. Huang, H. Ji, Y. Tong, Boosting the photocatalytic performance of (001) BiOI : enhancing donor density and separation efficiency of photogenerated electrons and holes, *Chem. Commun.*, 52 (2016) 5316-5319.

[247] X. Zhang, L. Zhang, T. Xie, D. Wang, Low-temperature synthesis and high visible-light-induced photocatalytic activity of BiOI/TiO_2 heterostructures, *J. Phys. Chem. C.*, 113 (2009) 7371-7378.

[248] J. Jiang, X. Zhang, P. Sun, L. Zhang, ZnO/BiOI heterostructures: photoinduced charge-transfer property and enhanced visible-light photocatalytic activity, *J. Phys. Chem. C.*, 115 (2011) 20555-20564.

[249] X. Xiao, R. Hao, M. Liang, X. Zuo, J. Nan, L. Li, W. Zhang, One-pot solvothermal synthesis of three-dimensional (3D) BiOI/BiOCl composites with enhanced visible-light photocatalytic activities for the degradation of bisphenol-A, *J. Hazard. Mater.*, 233-234 (2012) 122-130.

[250] M. Yan, Y. Hua, F. Zhu, W. Gu, J. Jiang, H. Shen, W. Shi, Fabrication of nitrogen doped graphene quantum dots- $\text{BiOI}/\text{MnNb}_2\text{O}_6$ p-n junction photocatalysts with enhanced visible light efficiency in photocatalytic degradation of antibiotics, *Appl. Catal. B. Environ.*, 202 (2017) 518-527.

[251] J.-C. Wang, H.-C. Yao, Z.-Y. Fan, L. Zhang, J.-S. Wang, S.-Q. Zang, Z.-J. Li, Indirect Z-scheme $\text{BiOI}/\text{g-C}_3\text{N}_4$ photocatalysts with enhanced photoreduction CO_2 activity under visible light irradiation, *ACS. Appl. Mater. Inter.*, 8 (2016) 3765-3775.

[252] D. Jiang, L. Chen, J. Zhu, M. Chen, W. Shi, J. Xie, Novel p-n heterojunction photocatalyst constructed by porous graphite-like C_3N_4 and nanostructured BiOI : facile synthesis and enhanced photocatalytic activity, *Dalton. T.*, 42 (2013) 15726-15734.

[253] Z. Gu, L. Chen, B. Duan, Q. Luo, J. Liu, C. Duan, Synthesis of $\text{Au}@\text{UiO-66}(\text{NH}_2)$ structures by small molecule-assisted nucleation for plasmon-enhanced photocatalytic activity, *Chem. Commun.*, 52 (2016) 116-119.

[254] Q. Liang, J. Jin, C. Liu, S. Xu, C. Yao, Z. Li, Fabrication of the ternary heterojunction $\text{Cd}_{0.5}\text{Zn}_{0.5}\text{S}@\text{UiO-66}@\text{g-C}_3\text{N}_4$ for enhanced visible-light photocatalytic hydrogen evolution and degradation of organic pollutants, *Inorg. Chem. Front.*, 5 (2018) 335-343.

[255] L. Jiang, X. Yuan, G. Zeng, Z. Wu, J. Liang, X. Chen, L. Leng, H. Wang, H. Wang, Metal-free efficient photocatalyst for stable visible-light photocatalytic degradation of refractory pollutant, *Appl. Catal. B. Environ.*, 221 (2018) 715-725.

[256] J. Xie, N. Guo, A. Liu, Y. Cao, J. Hu, D. Jia, Simple solid-state synthesis of $\text{BiOCl}/\text{Bi}_2\text{O}_2\text{CO}_3$ heterojunction and its excellent photocatalytic degradation of RhB , *J. Alloy. Compd.*, 784 (2019) 377-385.

[257] Y. Ma, Y. Jia, Z. Jiao, M. Yang, Y. Qi, Y. Bi, Hierarchical Bi_2MoO_6 nanosheet-built frameworks with excellent photocatalytic properties, *Chem. Commun.*, 51 (2015) 6655-6658.

[258] S. Luo, J. Ke, M. Yuan, Q. Zhang, P. Xie, L. Deng, S. Wang, CuInS_2 quantum dots embedded in Bi_2WO_6 nanoflowers for enhanced visible light photocatalytic removal of

contaminants, *Appl. Catal. B. Environ.*, 221 (2018) 215-222.

[259] M. Dan-Hardi, C. Serre, T. Frot, L. Rozes, G. Maurin, C. Sanchez, G. Férey, A new photoactive crystalline highly porous Titanium(IV) dicarboxylate, *J. Am. Chem. Soc.*, 131 (2009) 10857-10859.

[260] C.H. Hendon, D. Tiana, M. Fontecave, C. Sanchez, L. D'arras, C. Sassoys, L. Rozes, C. Mellot-Draznieks, A. walsh, engineering the optical response of the Titanium-MIL-125 metal-organic framework through ligand functionalization, *J. Am. Chem. Soc.*, 135 (2013) 10942-10945.

[261] S.-N. Kim, J. Kim, H.-Y. Kim, H.-Y. Cho, W.-S. Ahn, Adsorption/catalytic properties of MIL-125 and NH₂-MIL-125, *Catal. Today.*, 204 (2013) 85-93.

[262] D. Jiang, P. Xu, H. Wang, G. Zeng, D. Huang, M. Chen, C. Lai, C. Zhang, J. Wan, W. Xue, Strategies to improve metal organic frameworks photocatalyst's performance for degradation of organic pollutants, *Coordin. Chem. Rev.*, 376 (2018) 449-466.

[263] L.-W. Zhang, Y.-J. Wang, H.-Y. Cheng, W.-Q. Yao, Y.-F. Zhu, Synthesis of porous Bi₂WO₆ thin films as efficient visible-light-active photocatalysts, *Adv. Mater.*, 21 (2009) 1286-1290.

[264] L. Zhang, H. Wang, Z. Chen, P.K. Wong, J. Liu, Bi₂WO₆ micro/nano-structures: synthesis, modifications and visible-light-driven photocatalytic applications, *Appl. Catal. B. Environ.*, 106 (2011) 1-13.

[265] J. Di, J. Xia, M. Ji, B. Wang, S. Yin, Q. Zhang, Z. Chen, H. Li, Carbon quantum dots modified BiOCl ultrathin nanosheets with enhanced molecular oxygen activation ability for broad spectrum photocatalytic properties and mechanism insight, *ACS. Appl. Mater. Inter.*, 7 (2015) 20111-20123.

[266] H. Fan, T. Jiang, H. Li, D. Wang, L. Wang, J. Zhai, D. He, P. Wang, T. Xie, Effect of BiVO₄ crystalline phases on the photoinduced carriers behavior and photocatalytic activity, *J. Phys. Chem. C.*, 116 (2012) 2425-2430.

[267] L. Zhang, D. Chen, X. Jiao, Monoclinic structured BiVO₄ nanosheets: hydrothermal preparation, formation mechanism, and coloristic and photocatalytic properties, *J. Phys. Chem. B.*, 110 (2006) 2668-2673.

[268] M. Shang, W. Wang, J. Ren, S. Sun, L. Zhang, A novel BiVO₄ hierarchical nanostructure: controllable synthesis, growth mechanism, and application in photocatalysis, *CrystEngComm.*, 12 (2010) 1754-1758.

[269] X.-H. Yi, C.-C. Wang, Elimination of emerging organic contaminants in wastewater by advanced oxidation process over iron-based MOFs and their composites, *Prog. Chem.*, 2020, DOI: 10.7536/PC200562.

[270] F. Mu, B. Dai, W. Zhao, L. Zhang, J. Xu, X. Guo, A review on metal-organic frameworks for photoelectrocatalytic applications, *Chin. Chem. Lett.*, 31 (2020) 1773-1781.

[271] K.G.M. Laurier, F. Vermoortele, R. Ameloot, D.E. De Vos, J. Hofkens, M.B.J. Roeffaers, Iron(III)-based metal-organic frameworks as visible light photocatalysts, *J. Am. Chem. Soc.*, 135 (2013) 14488-14491.

[272] Y. Gao, G. Yu, K. Liu, S. Deng, B. Wang, J. Huang, Y. Wang, Integrated adsorption and visible-light photodegradation of aqueous clofibric acid and carbamazepine by a Fe-based metal-organic framework, *Chem. Eng. J.*, 330 (2017) 157-165.

[273] Y. Gao, S. Li, Y. Li, L. Yao, H. Zhang, Accelerated photocatalytic degradation of organic pollutant over metal-organic framework MIL-53(Fe) under visible LED light mediated by persulfate, *Appl. Catal. B. Environ.*, 202 (2017) 165-174.

- [274] L. Chen, H.D. Ji, J.J. Qi, T.B. Huang, C.-C. Wang, Degradation of acetaminophen by activated peroxymonosulfate using $\text{Co}(\text{OH})_2$ hollow microsphere supported titanate nanotubes: Insights into sulfate radical production pathway through CoOH^+ activation, *Chem. Eng. J.*, 406 (2021) 126877.
- [275] N. Liu, W. Huang, X. Zhang, L. Tang, L. Wang, Y. Wang, M. Wu, Ultrathin graphene oxide encapsulated in uniform MIL-88A(Fe) for enhanced visible light-driven photodegradation of RhB, *Appl. Catal. B. Environ.*, 221 (2018) 119-128.
- [276] P. Zhou, J. Yu, M. Jaroniec, All-solid-state Z-Scheme photocatalytic systems, *Adv. Mater.*, 26 (2014) 4920-4935.
- [277] Q. Xu, L. Zhang, J. Yu, S. Wageh, A.A. Al-Ghamdi, M. Jaroniec, Direct Z-scheme photocatalysts: principles, synthesis, and applications, *Mater. Today.*, 21 (2018) 1042-1063.
- [278] J. Low, C. Jiang, B. Cheng, S. Wageh, A.A. Al-Ghamdi, J. Yu, A review of direct Z-Scheme photocatalysts, *Small. Methods.*, 1 (2017) 1700080.
- [279] J. Fu, J. Yu, C. Jiang, B. Cheng, g- C_3N_4 -based heterostructured photocatalysts, *Adv. Energy. Mater.*, 8 (2018) 1701503.
- [280] Y. Qiu, J. Zhou, J. Cai, W. Xu, Z. You, C. Yin, Highly efficient microwave catalytic oxidation degradation of p-nitrophenol over microwave catalyst of pristine $\alpha\text{-Bi}_2\text{O}_3$, *Chem. Eng. J.*, 306 (2016) 667-675.
- [281] F. Chen, H.W. Huang, L. Guo, Y.H. Zhang, T.Y. Ma, The role of polarization in photocatalysis, *Angew. Chem. Int. Edit.*, 58 (2019) 10061-10073.
- [282] M. Han, J. Jia, 3D $\text{Bi}_2\text{S}_3/\text{TiO}_2$ cross-linked heterostructure: an efficient strategy to improve charge transport and separation for high photoelectrochemical performance, *J. Power. Sources.*, 329 (2016) 23-30.
- [283] Y. Huang, X. Zhang, G. Zhu, Y. Gao, Q. Cheng, X. Cheng, Synthesis of silver phosphate/sillenite bismuth ferrite/graphene oxide nanocomposite and its enhanced visible light photocatalytic mechanism, *Sep. Purif. Technol.*, 215 (2019) 490-499.
- [284] Z. Yang, X. Xu, X. Liang, C. Lei, Y. Wei, P. He, B. Lv, H. Ma, Z. Lei, MIL-53(Fe)-graphene nanocomposites: efficient visible-light photocatalysts for the selective oxidation of alcohols, *Appl. Catal. B. Environ.*, 198 (2016) 112-123.
- [285] S. Surblé, C. Serre, C. Mellot-Draznieks, F. Millange, G. Férey, A new isorecticular class of metal-organic-frameworks with the MIL-88 topology, *Chem. Commun.*, 3 (2006) 284-286.
- [286] N.A. Ramsahye, T.K. Trung, L. Scott, F. Nouar, T. Devic, P. Horcajada, E. Magnier, O. David, C. Serre, P. Trens, Impact of the flexible character of MIL-88 Iron(III) dicarboxylates on the adsorption of n-alkanes, *Chem. Mater.*, 25 (2013) 479-488.
- [287] B. Xu, H. Yang, Y. Cai, H. Yang, C. Li, Preparation and photocatalytic property of spindle-like MIL-88B(Fe) nanoparticles, *Inorg. Chem. Commun.*, 67 (2016) 29-31.
- [288] D. Yu, L. Li, M. Wu, J.C. Crittenden, Enhanced photocatalytic ozonation of organic pollutants using an iron-based metal-organic framework, *Appl. Catal. B. Environ.*, 251 (2019) 66-75.
- [289] A. Dhakshinamoorthy, A.M. Asiri, H. García, Metal-organic framework (MOF) compounds: photocatalysts for redox reactions and solar fuel production, *Angew. Chem. Int. Edit.*, 55 (2016) 5414-5445.
- [290] Z. Shao, D. Zhang, H. Li, C. Su, X. Pu, Y. Geng, Fabrication of MIL-88A/g- C_3N_4 direct Z-scheme heterojunction with enhanced visible-light photocatalytic activity, *Sep. Purif. Technol.*,

220 (2019) 16-24.

[291] Q. Chen, J. Li, L. Cheng, H. Liu, Construction of CdLa₂S₄/MIL-88A(Fe) heterojunctions for enhanced photocatalytic H₂-evolution activity via a direct Z-scheme electron transfer, *Chem. Eng. J.*, 379 (2020) 122389.

[292] Z. Jin, W. Dong, M. Yang, J. Wang, H. Gao, G. Wang, One-pot preparation of hierarchical nanosheet-constructed Fe₃O₄/MIL-88B(Fe) magnetic microspheres with high efficiency photocatalytic degradation of dye, *ChemCatChem.*, 8 (2016) 3510-3517.

[293] M. Ahmad, X. Quan, S. Chen, H. Yu, Tuning lewis acidity of MIL-88B-Fe with mix-valence coordinatively unsaturated iron centers on ultrathin Ti₃C₂ nanosheets for efficient photo-fenton reaction, *Appl. Catal. B. Environ.*, 264 (2020) 118534.

[294] X. Xu, X. Ding, X. Yang, P. Wang, S. Li, Z. Lu, H. Chen, Oxygen vacancy boosted photocatalytic decomposition of ciprofloxacin over Bi₂MoO₆: oxygen vacancy engineering, biotoxicity evaluation and mechanism study, *J. Hazard. Mater.*, 364 (2019) 691-699.

[295] K. Jing, W. Ma, Y. Ren, J. Xiong, B. Guo, Y. Song, S. Liang, L. Wu, Hierarchical Bi₂MoO₆ spheres in situ assembled by monolayer nanosheets toward photocatalytic selective oxidation of benzyl alcohol, *Appl. Catal. B. Environ.*, 243 (2019) 10-18.

[296] J. Di, X. Zhao, C. Lian, M. Ji, J. Xia, J. Xiong, W. Zhou, X. Cao, Y. She, H. Liu, K.P. Loh, S.J. Pennycook, H. Li, Z. Liu, Atomically-thin Bi₂MoO₆ nanosheets with vacancy pairs for improved photocatalytic CO₂ reduction, *Nano. Energy.*, 61 (2019) 54-59.

[297] P. Horcajada, F. Salles, S. Wuttke, T. Devic, D. Heurtaux, G. Maurin, A. Vimont, M. Daturi, O. David, E. Magnier, N. Stock, Y. Filinchuk, D. Popov, C. Riekkel, G. Férey, C. Serre, How linker's modification controls swelling properties of highly flexible Iron(III) dicarboxylates MIL-88, *J. Am. Chem. Soc.*, 133 (2011) 17839-17847.

[298] Q. Wang, W. Wang, L. Zhong, D. Liu, X. Cao, F. Cui, Oxygen vacancy-rich 2D/2D BiOCl-g-C₃N₄ ultrathin heterostructure nanosheets for enhanced visible-light-driven photocatalytic activity in environmental remediation, *Appl. Catal. B. Environ.*, 220 (2018) 290-302.

[299] C. Zhao, Z. Wang, X. Chen, H. Chu, H. Fu, C.-C. Wang, Robust photocatalytic benzene degradation using mesoporous disk-like N-TiO₂ derived from MIL-125(Ti), *Chin. J. Catal.*, 41 (2020) 1186-1197.

[300] P. Horcajada, S. Surblé, C. Serre, D.-Y. Hong, Y.-K. Seo, J.-S. Chang, J.-M. Grenèche, I. Margiolaki, G. Férey, Synthesis and catalytic properties of MIL-100(Fe), an Iron(III) carboxylate with large pores, *Chem. Commun.*, 27 (2007) 2820-2822.

[301] J.W. Yoon, Y.-K. Seo, Y.K. Hwang, J.-S. Chang, H. Leclerc, S. Wuttke, P. Bazin, A. Vimont, M. Daturi, E. Bloch, P.L. Llewellyn, C. Serre, P. Horcajada, J.-M. Grenèche, A.E. Rodrigues, G. Férey, Controlled reducibility of a metal-organic framework with coordinatively unsaturated sites for preferential gas sorption, *Angew. Chem. Int. Edit.*, 49 (2010) 5949-5952.

[302] F. Zhang, J. Shi, Y. Jin, Y. Fu, Y. Zhong, W. Zhu, Facile synthesis of MIL-100(Fe) under HF-free conditions and its application in the acetalization of aldehydes with diols, *Chem. Eng. J.*, 259 (2015) 183-190.

[303] Y.-K. Seo, J.W. Yoon, J.S. Lee, U.H. Lee, Y.K. Hwang, C.-H. Jun, P. Horcajada, C. Serre, J.-S. Chang, Large scale fluorine-free synthesis of hierarchically porous Iron(III) trimesate MIL-100(Fe) with a zeolite MTN topology, *Micropor. Mesopor. Mat.*, 157 (2012) 137-145.

[304] X. Liu, R. Dang, W. Dong, X. Huang, J. Tang, H. Gao, G. Wang, A sandwich-like heterostructure of TiO₂ nanosheets with MIL-100(Fe): A platform for efficient visible-light-driven

photocatalysis, *Appl. Catal. B. Environ.*, 209 (2017) 506-513.

[305] M. Ahmad, S. Chen, F. Ye, X. Quan, S. Afzal, H. Yu, X. Zhao, Efficient photo-fenton activity in mesoporous MIL-100(Fe) decorated with ZnO nanosphere for pollutants degradation, *Appl. Catal. B. Environ.*, 245 (2019) 428-438.

[306] S. Li, J. Cui, X. Wu, X. Zhang, Q. Hu, X. Hou, Rapid in situ microwave synthesis of Fe₃O₄@MIL-100(Fe) for aqueous diclofenac sodium removal through integrated adsorption and photodegradation, *J. Hazard. Mater.*, 373 (2019) 408-416.

[307] I. Bezverkhyy, E. Popova, N. Geoffroy, F. Herbst, J.P. Bellat, Preparation of magnetic composites of MIL-53(Fe) or MIL-100(Fe) via partial transformation of their framework into γ -Fe₂O₃, *J. Mater. Chem. A.*, 4 (2016) 8141-8148.

[308] R. Liang, F. Jing, L. Shen, N. Qin, L. Wu, M@MIL-100(Fe) (M = Au, Pd, Pt) nanocomposites fabricated by a facile photodeposition process: efficient visible-light photocatalysts for redox reactions in water, *Nano. Res.*, 8 (2015) 3237-3249.

[309] S.S.-Y. Chui, S.M.-F. Lo, J.P.H. Charmant, A.G. Orpen, I.D. Williams, A chemically functionalizable nanoporous material [Cu₃(TMA)₂(H₂O)₃]_n, *Science.*, 283 (1999) 1148-1150.

[310] N. Al-Janabi, P. Hill, L. Torrente-Murciano, A. Garforth, P. Gorgojo, F. Siperstein, X. Fan, Mapping the Cu-BTC metal-organic framework (HKUST-1) stability envelope in the presence of water vapour for CO₂ adsorption from flue gases, *Chem. Eng. J.*, 281 (2015) 669-677.

[311] N. Nijem, H. Bluhm, M.L. Ng, M. Kunz, S.R. Leone, M.K. Gilles, Cu¹⁺ in HKUST-1: selective gas adsorption in the presence of water, *Chem. Commun.*, 50 (2014) 10144-10147.

[312] F. Raganati, V. Gargiulo, P. Ammendola, M. Alfe, R. Chirone, CO₂ capture performance of HKUST-1 in a sound assisted fluidized bed, *Chem. Eng. J.*, 239 (2014) 75-86.

[313] J. Moellmer, A. Moeller, F. Dreisbach, R. Glaeser, R. Staudt, High pressure adsorption of hydrogen, nitrogen, carbon dioxide and methane on the metal-organic framework HKUST-1, *Micropor. Mesopor. Mat.*, 138 (2011) 140-148.

[314] Z. Zhao, S. Wang, Y. Yang, X. Li, J. Li, Z. Li, Competitive adsorption and selectivity of benzene and water vapor on the microporous metal organic frameworks (HKUST-1), *Chem. Eng. J.*, 259 (2015) 79-89.

[315] Q. Chen, Q.-W. Chen, C. Zhuang, P.-P. Tang, N. Lin, L.-Q. Wei, Controlled release of drug molecules in metal-organic framework material HKUST-1, *Inorg. Chem. Commun.*, 79 (2017) 78-81.

[316] F. Ke, Y.-P. Yuan, L.-G. Qiu, Y.-H. Shen, A.-J. Xie, J.-F. Zhu, X.-Y. Tian, L.-D. Zhang, Facile fabrication of magnetic metal-organic framework nanocomposites for potential targeted drug delivery, *J. Mater. Chem.*, 21 (2011) 3843-3848.

[317] C. Fan, H. Dong, Y. Liang, J. Yang, G. Tang, W. Zhang, Y. Cao, Sustainable synthesis of HKUST-1 and its composite by biocompatible ionic liquid for enhancing visible-light photocatalytic performance, *J. Clean. Prod.*, 208 (2019) 353-362.

[318] A. Sachse, R. Ameloot, B. Coq, F. Fajula, B. Coasne, D. De Vos, A. Galarneau, In situ synthesis of Cu-BTC (HKUST-1) in macro-/mesoporous silica monoliths for continuous flow catalysis, *Chem. Commun.*, 48 (2012) 4749-4751.

[319] Y. Li, J. Wang, H. Yao, L. Dang, Z. Li, Chemical etching preparation of BiOI/Bi₂O₃ heterostructures with enhanced photocatalytic activities, *Catal. Commun.*, 12 (2011) 660-664.

[320] J. Hou, C. Yang, Z. Wang, W. Zhou, S. Jiao, H. Zhu, In situ synthesis of α - β phase heterojunction on Bi₂O₃ nanowires with exceptional visible-light photocatalytic performance, *Appl.*

Catal. B. Environ., 142-143 (2013) 504-511.

[321] B. Li, L. Nengzi, R. Guo, Y. Cui, Y. Zhang, X. Cheng, Novel synthesis of Z-scheme α - $\text{Bi}_2\text{O}_3/\text{g-C}_3\text{N}_4$ composite photocatalyst and its enhanced visible light photocatalytic performance: influence of calcination temperature, *Chin. Chem. Lett.*, 2020, DOI: 10.1016/j.cclet.2020.04.026 .

[322] J. Chen, J. Zhan, Y. Zhang, Y. Tang, Construction of a novel $\text{ZnCo}_2\text{O}_4/\text{Bi}_2\text{O}_3$ heterojunction photocatalyst with enhanced visible light photocatalytic activity, *Chin. Chem. Lett.*, 30 (2019) 735-738.

[323] D. Ravelli, D. Dondi, M. Fagnoni, A. Albini, Photocatalysis. a multi-faceted concept for green chemistry, *Chem. Soc. Rev.*, 38 (2009) 1999-2011.

[324] C. Wang, K.E. deKrafft, W. Lin, Pt Nanoparticles@photoactive metal-organic frameworks: efficient hydrogen evolution via synergistic photoexcitation and electron injection, *J. Am. Chem. Soc.*, 134 (2012) 7211-7214.

[325] R. Liang, S. Luo, F. Jing, L. Shen, N. Qin, L. Wu, A simple strategy for fabrication of $\text{Pd@MIL-100}(\text{Fe})$ nanocomposite as a visible-light-driven photocatalyst for the treatment of pharmaceuticals and personal care products (PPCPs), *Appl. Catal. B. Environ.*, 176-177 (2015) 240-248.

[326] H.-L. Jiang, B. Liu, T. Akita, M. Haruta, H. Sakurai, Q. Xu, Au@ZIF-8 : CO Oxidation over gold nanoparticles deposited to metal-organic framework, *J. Am. Chem. Soc.*, 131 (2009) 11302-11303.

[327] L.E. Kreno, J.T. Hupp, R.P. Van Duyne, Metal-organic framework thin film for enhanced localized surface plasmon resonance gas sensing, *Anal. Chem.*, 82 (2010) 8042-8046.

[328] O. Shekhah, J. Liu, R.A. Fischer, C. Wöll, MOF thin films: existing and future applications, *Chem. Soc. Rev.*, 40 (2011) 1081-1106.

[329] H.K. Arslan, O. Shekhah, D.C.F. Wieland, M. Paulus, C. Sternemann, M.A. Schroer, S. Tiemeyer, M. Tolan, R.A. Fischer, C. Wöll, Intercalation in layered metal-organic frameworks: reversible inclusion of an extended π -system, *J. Am. Chem. Soc.*, 133 (2011) 8158-8161.

[330] R.J.F. Berger, D. Rettenwander, S. Spirk, C. Wolf, M. Patzschke, M. Ertl, U. Monkowius, N.W. Mitzel, Relativistic effects in triphenylbismuth and their influence on molecular structure and spectroscopic properties, *Phys. Chem. Chem. Phys.*, 14 (2012) 15520-15524.

[331] Y. Zhang, J. Zhou, J. Chen, X. Feng, W. Cai, Rapid degradation of tetracycline hydrochloride by heterogeneous photocatalysis coupling persulfate oxidation with $\text{MIL-53}(\text{Fe})$ under visible light irradiation, *J. Hazard. Mater.*, 392 (2020) 122315.

[332] B. Garza-Campos, E. Brillas, A. Hernández-Ramírez, A. El-Ghenymy, J.L. Guzmán-Mar, E.J. Ruiz-Ruiz, Salicylic acid degradation by advanced oxidation processes. Coupling of solar photoelectro-fenton and solar heterogeneous photocatalysis, *J. Hazard. Mater.*, 319 (2016) 34-42.

[333] F. Ali, J.A. Khan, N.S. Shah, M. Sayed, H.M. Khan, Carbamazepine degradation by UV and UV-assisted AOPs: kinetics, mechanism and toxicity investigations, *Process. Saf. Environ.*, 117 (2018) 307-314.

[334] M. Ahmad, E. Ahmed, Z.L. Hong, W. Ahmed, A. Elhissi, N.R. Khalid, Photocatalytic, sonocatalytic and sonophotocatalytic degradation of Rhodamine B using ZnO/CNTs composites photocatalysts, *Ultrason. Sonochem.*, 21 (2014) 761-773.

[335] F.-X. Wang, X.-H. Yi, C.-C. Wang, J.-G. Deng, Photocatalytic Cr(VI) reduction and organic-pollutant degradation in a stable 2D coordination polymer, *Chin. J. Catal.*, 38 (2017) 2141-2149.

- [336] J. Shang, W. Hao, X. Lv, T. Wang, X. Wang, Y. Du, S. Dou, T. Xie, D. Wang, J. Wang, Bismuth oxybromide with reasonable photocatalytic reduction activity under visible light, *ACS. Catal.*, 4 (2014) 954-961.
- [337] S. Heidari, M. Haghighi, M. Shabani, Sunlight-activated BiOCl/BiOBr–Bi₂₄O₃₁Br₁₀ photocatalyst for the removal of pharmaceutical compounds, *J. Clean. Prod.*, 259 (2020) 120679.
- [338] X. Xiao, C. Zheng, M. Lu, L. Zhang, F. Liu, X. Zuo, J. Nan, Deficient Bi₂₄O₃₁Br₁₀ as a highly efficient photocatalyst for selective oxidation of benzyl alcohol into benzaldehyde under blue LED irradiation, *Appl. Catal. B. Environ.*, 228 (2018) 142-151.
- [339] X. Xiao, R. Hu, C. Liu, C. Xing, X. Zuo, J. Nan, L. Wang, Facile microwave synthesis of novel hierarchical Bi₂₄O₃₁Br₁₀ nanoflakes with excellent visible light photocatalytic performance for the degradation of tetracycline hydrochloride, *Chem. Eng. J.*, 225 (2013) 790-797.
- [340] R. Liang, L. Shen, F. Jing, W. Wu, N. Qin, R. Lin, L. Wu, NH₂-mediated indium metal–organic framework as a novel visible-light-driven photocatalyst for reduction of the aqueous Cr(VI), *Appl. Catal. B. Environ.*, 162 (2015) 245-251.
- [341] D. Yang, Y. Sun, Z. Tong, Y. Nan, Z. Jiang, Fabrication of bimodal-pore SrTiO₃ microspheres with excellent photocatalytic performance for Cr(VI) reduction under simulated sunlight, *J. Hazard. Mater.*, 312 (2016) 45-54.
- [342] S. Luo, F. Qin, Y.a. Ming, H. Zhao, Y. Liu, R. Chen, Fabrication uniform hollow Bi₂S₃ nanospheres via kirkendall effect for photocatalytic reduction of Cr(VI) in electroplating industry wastewater, *J. Hazard. Mater.*, 340 (2017) 253-262.
- [343] J. Qiu, M. Li, L. Yang, J. Yao, Facile construction of three-dimensional netted ZnIn₂S₄ by cellulose nanofibrils for efficiently photocatalytic reduction of Cr(VI), *Chem. Eng. J.*, 375 (2019) 121990.
- [344] W. Huang, N. Liu, X. Zhang, M. Wu, L. Tang, Metal organic framework g-C₃N₄/MIL-53(Fe) heterojunctions with enhanced photocatalytic activity for Cr(VI) reduction under visible light, *Appl. Surf. Sci.*, 425 (2017) 107-116.
- [345] Z. Chen, Y.-J. Xu, Ultrathin TiO₂ layer coated-CdS spheres core–shell nanocomposite with enhanced visible-light photoactivity, *ACS. Appl. Mater. Inter.*, 5 (2013) 13353-13363.
- [346] G. Zhang, D. Chen, N. Li, Q. Xu, H. Li, J. He, J. Lu, SnS₂/SnO₂ heterostructured nanosheet arrays grown on carbon cloth for efficient photocatalytic reduction of Cr(VI), *J. Colloid. Interf. Sci.*, 514 (2018) 306-315.
- [347] W. Zhao, Y. Liu, Z. Wei, S. Yang, H. He, C. Sun, Fabrication of a novel p–n heterojunction photocatalyst n-BiVO₄@p-MoS₂ with core–shell structure and its excellent visible-light photocatalytic reduction and oxidation activities, *Appl. Catal. B. Environ.*, 185 (2016) 242-252.
- [348] H. Xu, Z. Wu, M. Ding, X. Gao, Microwave-assisted synthesis of flower-like BN/BiOCl composites for photocatalytic Cr(VI) reduction upon visible-light irradiation, *Mater. Design.*, 114 (2017) 129-138.
- [349] J. Wan, P. Xue, R. Wang, L. Liu, E. Liu, X. Bai, J. Fan, X. Hu, Synergistic effects in simultaneous photocatalytic removal of Cr(VI) and tetracycline hydrochloride by Z-scheme Co₃O₄/Ag/Bi₂WO₆ heterojunction, *Appl. Surf. Sci.*, 483 (2019) 677-687.
- [350] X. Liu, L. Pan, T. Lv, T. Lu, G. Zhu, Z. Sun, C. Sun, Microwave-assisted synthesis of ZnO–graphene composite for photocatalytic reduction of Cr(VI), *Catal. Sci. Technol.*, 1 (2011) 1189-1193.

- [351] P. Hu, X. Liu, B. Liu, L. Li, W. Qin, H. Yu, S. Zhong, Y. Li, Z. Ren, M. Wang, Hierarchical layered Ni_3S_2 -graphene hybrid composites for efficient photocatalytic reduction of Cr(VI), *J. Colloid. Interf. Sci.*, 496 (2017) 254-260.
- [352] X. Liu, L. Pan, T. Lv, G. Zhu, Z. Sun, C. Sun, Microwave-assisted synthesis of CdS-reduced graphene oxide composites for photocatalytic reduction of Cr(VI), *Chem. Commun.*, 47 (2011) 11984-11986.
- [353] K. Li, Y. Liang, J. Yang, G. Yang, H. Zhang, K. Wang, R. Xu, X. Xie, Glucose-induced fabrication of Bi/ α - $\text{FeC}_2\text{O}_4 \cdot 2\text{H}_2\text{O}$ heterojunctions: a bifunctional catalyst with enhanced photocatalytic and Fenton oxidation efficiency, *Catal. Sci. Technol.*, 9 (2019) 2543-2552.
- [354] L. Wang, X. Li, W. Teng, Q. Zhao, Y. Shi, R. Yue, Y. Chen, Efficient photocatalytic reduction of aqueous Cr(VI) over flower-like SnIn_4S_8 microspheres under visible light illumination, *J. Hazard. Mater.*, 244-245 (2013) 681-688.
- [355] A.P. Reverberi, P.S. Varbanov, S. Lauciello, M. Salerno, B. Fabiano, An eco-friendly process for zerovalent bismuth nanoparticles synthesis, *J. Clean. Prod.*, 198 (2018) 37-45.
- [356] A.P. Reverberi, M. Vocciante, M. Salerno, V. Caratto, B. Fabiano, Bi nanoparticles synthesis by a bottom-up wet chemical process, *Chem. Eng. Trans.*, 73 (2019) 283-288.
- [357] D-D. Chen, X-H. Yi, C-C. Wang, Preparation of metal-organic frameworks and their composites using mechanochemical methods, *Chin. J. Inorg. Chem.*, 36(2020)1805-1821.
- [358] A.P. Reverberi, M. Vocciante, M. Salerno, M. Ferretti, B. Fabiano, Green synthesis of Silver nanoparticles by low-energy wet bead milling of metal spheres, *Materials.*, 13 (2020) 63.
- [359] J. Qin, S. Wang, X. Wang, Visible-light reduction CO_2 with dodecahedral zeolitic imidazolate framework ZIF-67 as an efficient co-catalyst, *Appl. Catal. B. Environ.*, 209 (2017) 476-482.
- [360] G. Zhong, D. Liu, J. Zhang, The application of ZIF-67 and its derivatives: adsorption, separation, electrochemistry and catalysts, *J. Mater. Chem. A.*, 6 (2018) 1887-1899.
- [361] G. Qu, X. Zhang, G. Xiang, Y. Wei, J. Yin, Z. Wang, X. Zhang, X. Xu, ZIF-67 derived hollow Ni-Co-Se nano-polyhedrons for flexible hybrid supercapacitors with remarkable electrochemical performances, *Chin. Chem. Lett.*, 31 (2020) 2007-2012.
- [362] G. Jia, L. Liu, L. Zhang, D. Zhang, Y. Wang, X. Cui, W. Zheng, 1D alignment of ZnO@ZIF-8/67 nanorod arrays for visible-light-driven photoelectrochemical water splitting, *Appl. Surf. Sci.*, 448 (2018) 254-260.

Figure Captions

Figure 1. Band positions of some common (a) MOFs and (b) bismuth-based photocatalysts and the relevant reaction potentials at pH = 7 [44, 50, 51, 93-124].

Figure 2. (a) Number of publications of MBC photocatalysts during the past six years and (b) doughnut chart of photocatalytic applications of MBCs (source: web of science, date: 6th November 2020, key words: MOFs, bismuth and photocatalysis).

Figure 3. TEM micrographs of (a) ZIF-8, (b) and (d) $\text{Bi}_4\text{O}_5\text{Br}_2/\text{ZIF-8}$ (30%), (c) $\text{Bi}_4\text{O}_5\text{Br}_2$ nanoparticles, (e) photocatalytic N_2 fixation activities of as-prepared materials, (f) band potentials of ZIF-8 and $\text{Bi}_4\text{O}_5\text{Br}_2$, (g)-(h) contact angles of ZIF-8 and $\text{Bi}_4\text{O}_5\text{Br}_2/\text{ZIF-8}$ (30%), (i) photocatalytic efficiencies of $\text{Bi}_4\text{O}_5\text{Br}_2$ and $\text{Bi}_4\text{O}_5\text{Br}_2/\text{ZIF-8}$ (30%) versus light intensities and (j) photocatalytic mechanism of $\text{Bi}_4\text{O}_5\text{Br}_2/\text{ZIF-8}$ (30%) [125], copyright (2019) Elsevier.

Figure 4. (a) The fabrication of the $\text{Bi}_2\text{S}_3/\text{ZIF-8}$ core-shell composites, (b)-(e) SEM micrographs of pure Bi_2S_3 , ZIF-8, B@Z-7, and B@Z-10, (f)-(g) TEM micrographs of B@Z-10 and the material after treatment with ultrasonication for 1 h, and (h) the photocatalytic mechanism for the RhB decomposition over B@Z-10 [126], copyright (2018) Royal Society of Chemistry.

Figure 5. (a)-(b) SEM images of pure BiOBr and BU-3 composite, (c)-(d) PXRD patterns and UV-vis DRS spectra of BiOBr, UiO-66 and BU-3 composite, (e) the degradation of atrazine in visible light radiation by different photocatalysts, insert: adsorption curves of atrazine by the samples, (f) a possible reaction mechanism of atrazine degradation over UiO-66/BiOBr composite [132], copyright (2019) Elsevier.

Figure 6. (a) The procedure for the preparation of $\text{NH}_2\text{-UiO-66/BiOBr}$ in Hu and co-workers' study, (b)-(c) SEM and TEM images of the NU/BOB-15 composite, (d)-(e) SEM images of the BUN-20 composite in Yang and co-workers' study, (f) removal performances of NOR in the existence of diverse samples (pH = 7), (g) TOC removal efficiency of BUN-20 and Mix-20, (h) the possible reaction mechanism of NOR over the BUN-20 in simulated sunlight [136, 137], copyright (2019)

Elsevier.

Figure 7. (a) Schematic representation for BiOI@UNCN composites fabrication, (b)-(c) SEM and TEM images of BiOI@UNCN-40, (d)-(e) the degradation of TC and RhB over as-prepared materials in visible light, (f) the cyclic degradation of RhB over BiOI and BiOI@UNCN-40, (g) the proposed photocatalytic mechanism over the BiOI@UNCN-40 under visible light [119], copyright (2019) Elsevier.

Figure 8. (a) The procedure for the preparation of $\text{NH}_2\text{-MIL-125/Bi}_2\text{MoO}_6$ composites, (b)-(e) SEM images of 0.32-TiM@BiMO, 0.65-TiM@BiMO, 0.97-TiM@BiMO, 1.3-TiM@BiMO, (f) UV-vis DRS spectra of the as-prepared materials, (g) SKP maps of TiM, BiMO, and TiM@BiMO, (h)-(j) the photocatalytic activities for dichlorophen and trichlorophenol degradation and O_2 production over the different samples in visible light, (k) illustration of the photocatalytic mechanism of $\text{NH}_2\text{-MIL-125/Bi}_2\text{MoO}_6$ core-shell composites [144], copyright (2019) Elsevier.

Figure 9. (a) Schematic representation of the synthesis of $\text{NH}_2\text{-MIL-125/BiOCl}$ composites, (b)-(c) TEM and HRTEM images of NM/BOC-10, (d) UV-vis DRS spectra of the as-prepared materials, (e)-(f) transient photocurrent responses and EIS Nyquist plots of NM/BOC-10, BiOCl, and $\text{NH}_2\text{-MIL-125}$, (g) the reduction in TOC during the photodegradation of TC over NM/BOC-10, (h) $\text{DMPO}\cdot\text{O}_2^-$ ESR signals recorded with NM/BOC-10 and BiOCl and, (i) the possible mechanism for the transport of charges in $\text{NH}_2\text{-MIL-125/BiOCl}$ composite [149], copyright (2018) Elsevier.

Figure 10. SEM and TEM images of (a) MIL-53(Fe), (b) BiOBr, (c) HRTEM images of the BM-20, (d) UV-vis DRS spectra of MIL-53(Fe), BiOBr and BM- x composites, (e)-(g) Nyquist impedance plots, transient photocurrent responses, PL spectra of the as-prepared materials and (h) schematic representation of the CBZ degradation over the BM-20 [151], copyright (2019) Elsevier.

Figure 11. (a) TEM image of 32%-MBC, (b) N_2 adsorption-desorption isotherms of MIL-53(Fe), $\alpha\text{-Bi}_2\text{O}_3/\text{g-C}_3\text{N}_4$ and $x\text{-MBC}$ composites, (c) UV-vis DRS spectra of $\text{g-C}_3\text{N}_4$, $\alpha\text{-Bi}_2\text{O}_3$, MIL-53(Fe)

and *x*-MBC composites, (d)-(e) transient photocurrent curves and EIS plots of g-C₃N₄, α -Bi₂O₃, MIL-53(Fe), α -Bi₂O₃/g-C₃N₄ and 32%-MBC, (f) Mott-Schottky plots of MIL-53(Fe), α -Bi₂O₃/g-C₃N₄, 32%-MBC composite, (g) degradation of amido black 10B over different materials and (h) photocatalytic activity of MIL-53(Fe)/ α -Bi₂O₃/g-C₃N₄ in visible light [156], copyright (2020) Elsevier.

Figure 12. SEM images of (a) BM and (b) BMO, TEM images (c)-(d) of the sample of as-prepared 3-BMO/M88, (e) XPS O 1s spectra and (f) ESR spectra of BMO and BM samples, (g) diffuse reflectance UV-vis spectra and (h) time-resolved fluorescence decay curves of M88, BM, 3-BMO/M88 and BMO samples and (i) the mechanism of 3-BMO/M88 for photocatalytic degradation in visible light [123], copyright (2020) Elsevier.

Figure 13. (a) PXRD patterns of BiVO₄ nanoparticles and composite based on MIL-100(Fe)/BiVO₄, (b) UV-vis DRS of MIL-100(Cr), MIL-100(Fe), MIL-100(Cr)/BiVO₄, BiVO₄ and MIL-100(Fe)/BiVO₄ composites, (c)-(d) SEM images for the morphological analysis of MIL-100(Fe)/BiVO₄ and BiVO₄, (e) PL spectra, (f) EIS measurements and (g)-(h) transient photocurrent response of BiVO₄, MIL-100(Fe)/BiVO₄ and MIL-100(Cr)/BiVO₄ composites, (i)-(j) the proposed mechanism for photocatalytic production of O₂ over MIL-100(Fe)/BiVO₄ and MIL-100(Cr)/BiVO₄ composites when irradiated with visible light [162], copyright (2020) American Chemical Society.

Figure 14. (a) Synthesis scheme of the HKUST-1/Bi₂O₃ composite thin films, (b) schematic diagram for the automatic growth of thin films of HKUST-1 on Au substrates by LPE method, (c) experimental XRD patterns of the HKUST-1 thin film (black line), BiPh₃ loaded (red line) and after UV light irradiation (blue line), (d) simulation XRD patterns of HKUST-1 and 3 BiPh₃ loaded sample, (e)-(f) HAADF-STEM and SAED micrographs of the HKUST-1/Bi₂O₃ materials, (g) photocatalytic processes under different experimental conditions, (h) four repeated experiments of using the HKUST-1/Bi₂O₃ photocatalyst for degradation of NFR under UV light irradiation [167, 329], copyright (2016) Royal Society of Chemistry and (2011) American Chemical Society.

Figure 15. (a) Schematic diagram of sonophotocatalytic reactor set-up, (b)-(c) SEM micrographs of HKUST-1 and HKUST-1/Ag₃PO₄/Bi₂S₃ composite, (d) PL spectra of HKUST-1 and HKUST-1/Ag₃PO₄/Bi₂S₃ composite, (e)-(g) 3D plots of response surface graphs of dye concentration, flow rate, pH and reaction time on the catalytic efficiency (h) profiles for desirability function and predicated values for sonophotocatalytic degradation, lines shown with red dashes represent optimal values [170], copyright (2016) Elsevier.

Figure 16. (a) The procedure for the preparation of BUC-21/Bi₂₄O₃₁Br₁₀ composites, (b) UV-vis DRS spectra of BUC-21, Bi₂₄O₃₁Br₁₀ and the corresponding composites, (c)-(e) SEM, TEM and HRTEM images of BB-100, (f) Cr(VI) photoreduction at pH = 2 via numerous photocatalysts, (g) recycling experiments for the photoreduction of Cr(VI) over BB-100 and Bi₂₄O₃₁Br₁₀, (h) time-resolved PL decay spectra of BUC-21, Bi₂₄O₃₁Br₁₀, and BB-x composites, (i) representation of the possible mechanism of photoreduction of Cr(VI) over BB-100 under white light and (j) difference of electron density on the surface of BUC-21 and Bi₂₄O₃₁Br₁₀ fragment [44], copyright (2020) Elsevier.

Figure 17. (a) Schematic representation of the continuous flow reactor, (b)-(c) TEM images of CuWO₄/Bi₂S₃ and CuWO₄/Bi₂S₃/ZIF-67 composite, (d)-(e) the effect of adsorption, photolysis and photocatalysis processes on MTZ and CFX degradation at optimum conditions (pH = 7, photocatalyst dosage = 0.3 g·L⁻¹, antibiotic concentration = 20 mg·L⁻¹), (f) TOC removal of MTZ and CFX by the binary and ternary composites under LED irradiation at pH = 7 and photocatalyst dosage = 0.3 g·L⁻¹, proposed photocatalytic mechanism for CuWO₄/Bi₂S₃/ZIF-67 composite under light irradiation: (g) conventional path and (h) double Z-scheme structure [121], copyright (2020) Elsevier.

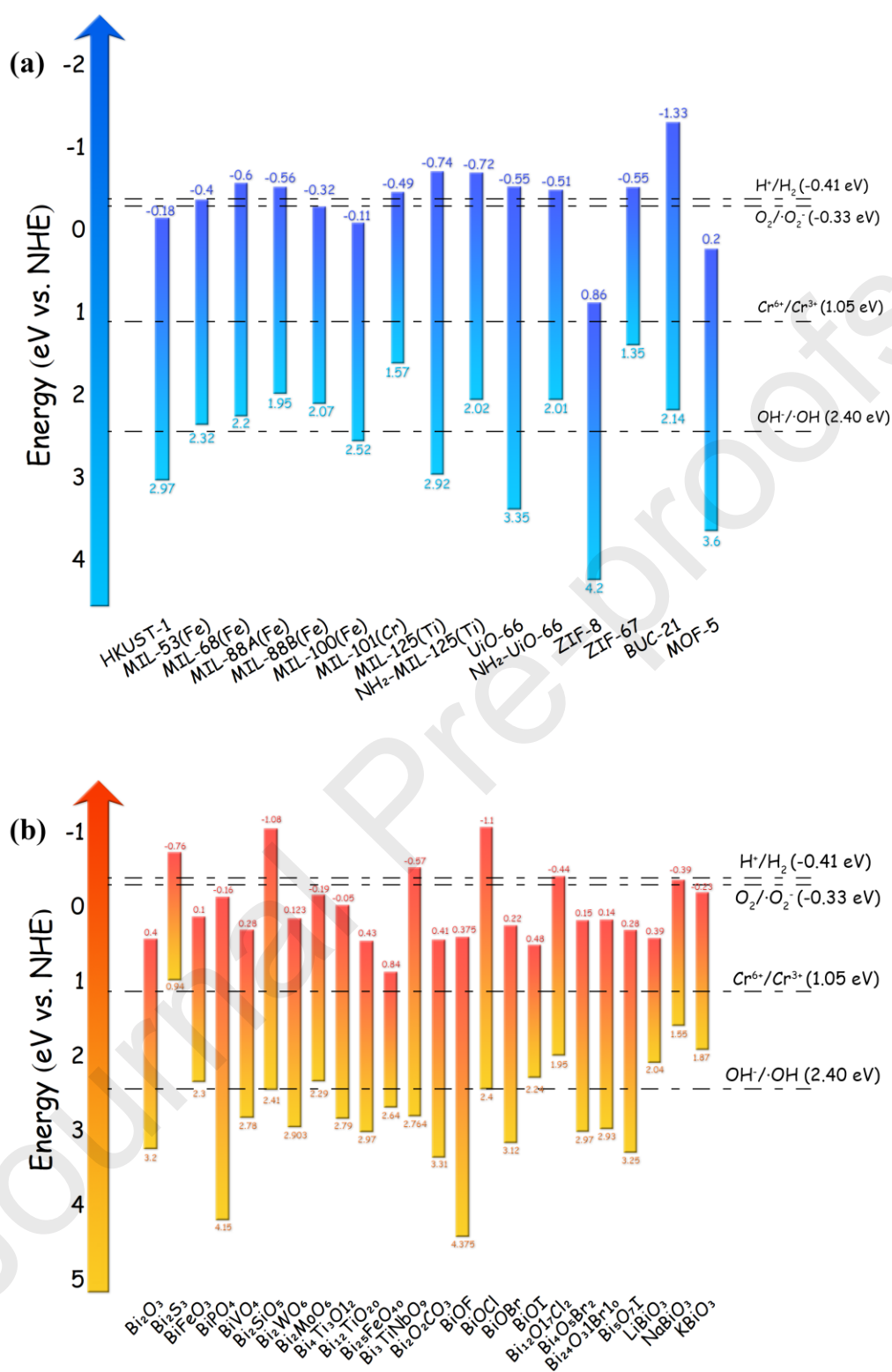


Figure 1

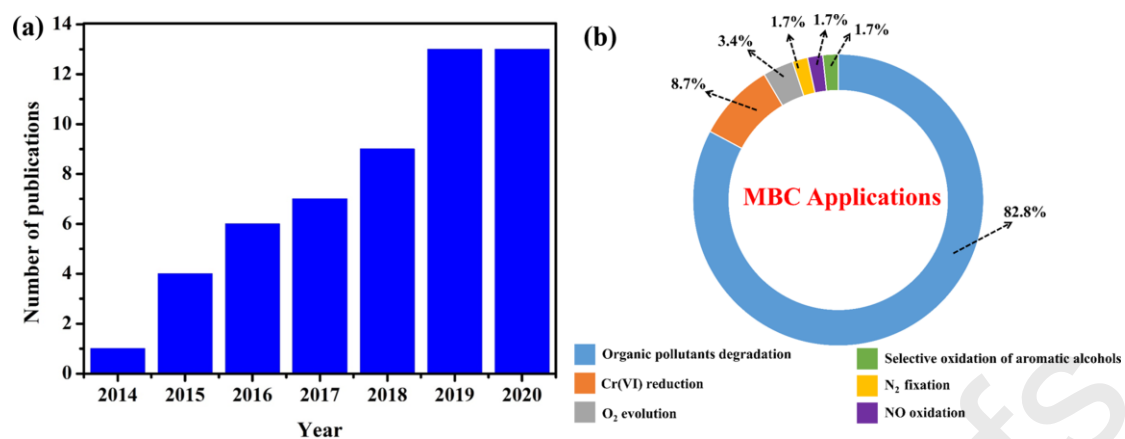


Figure 2

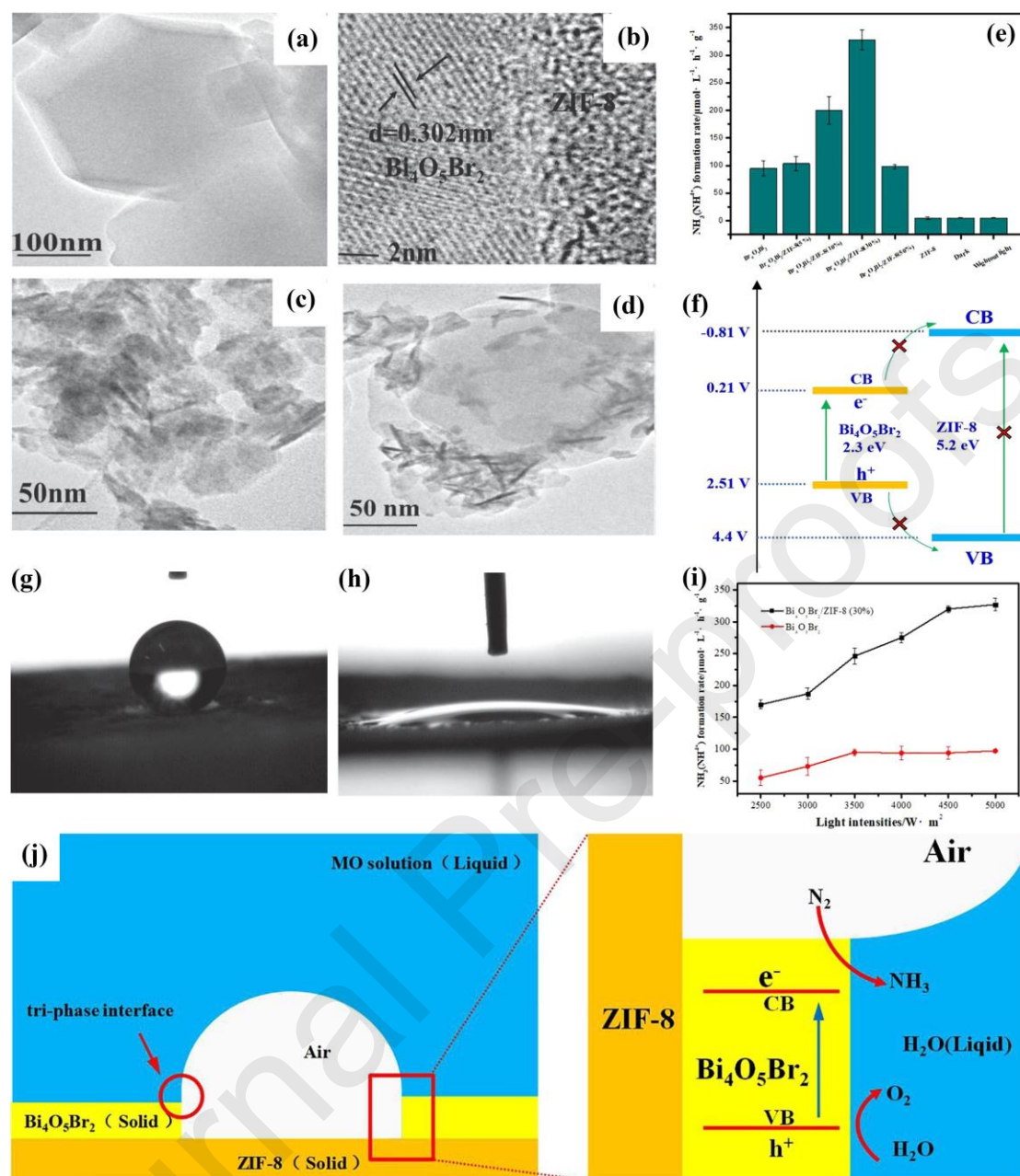


Figure 3

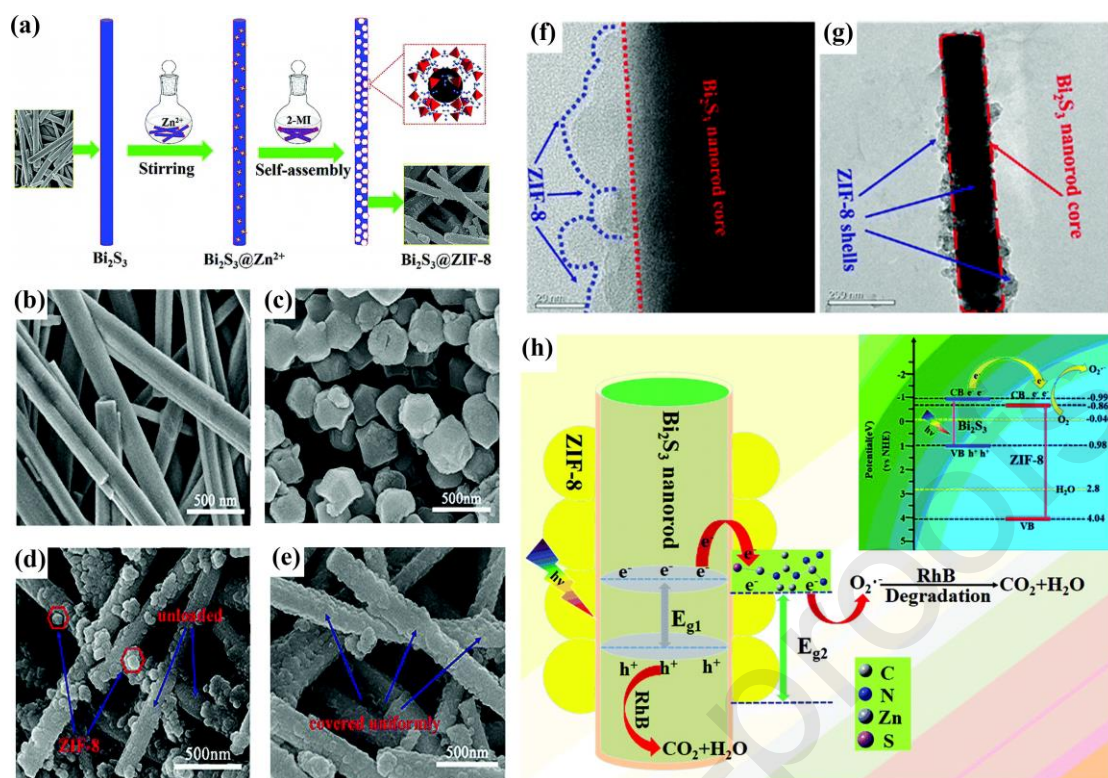


Figure 4

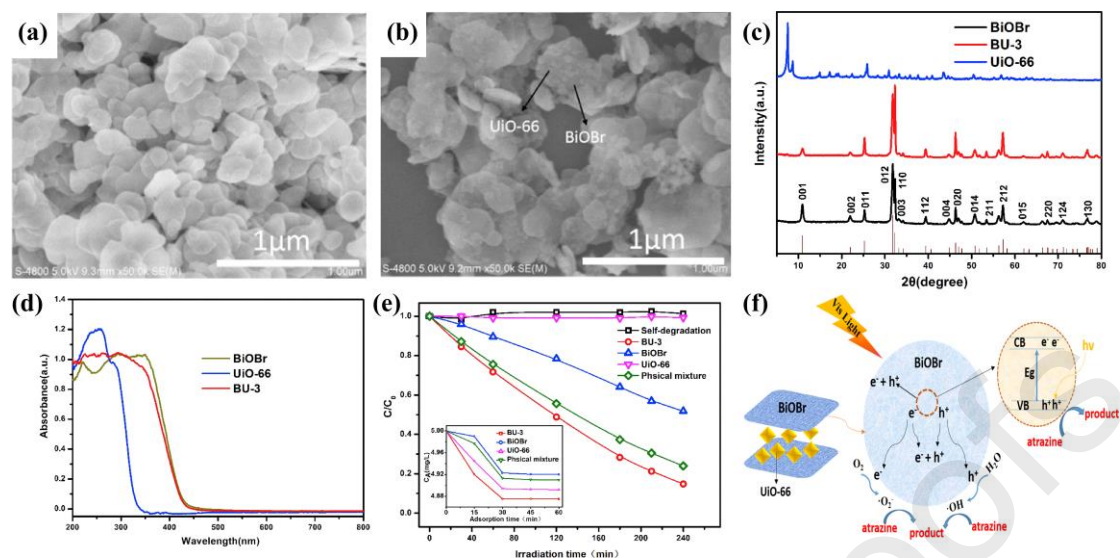


Figure 5

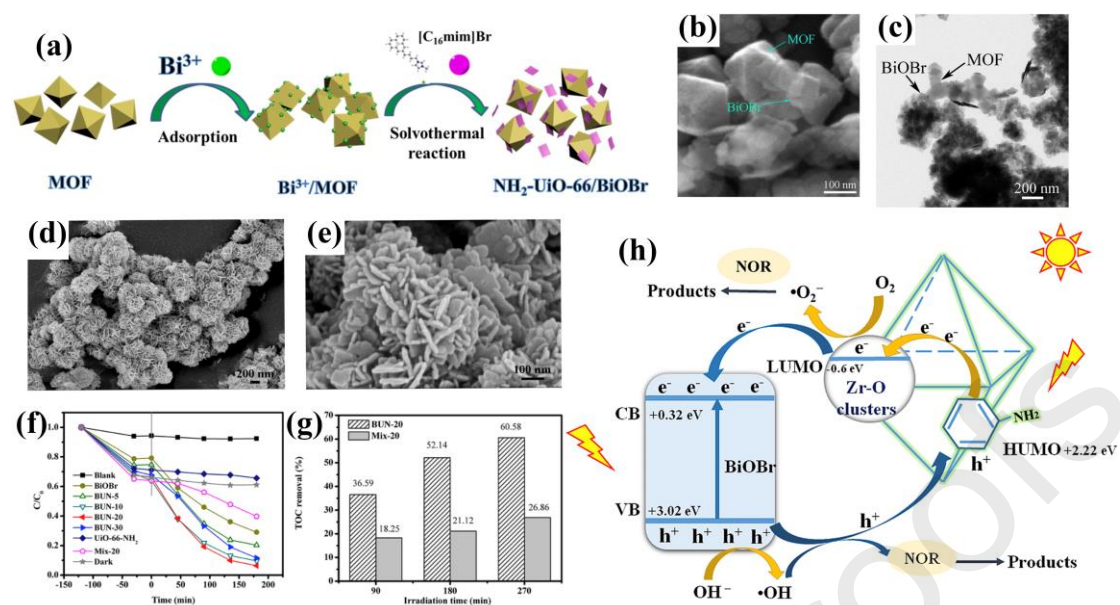


Figure 6

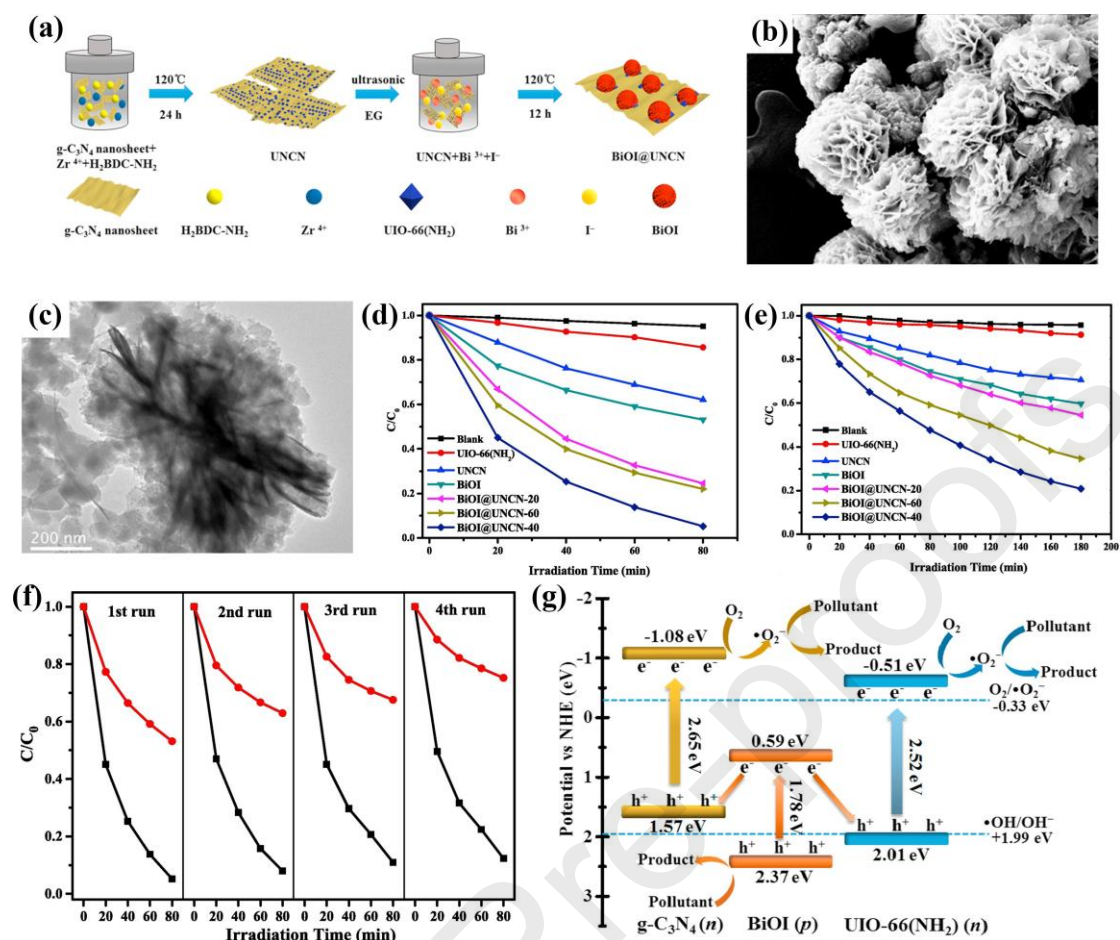


Figure 7

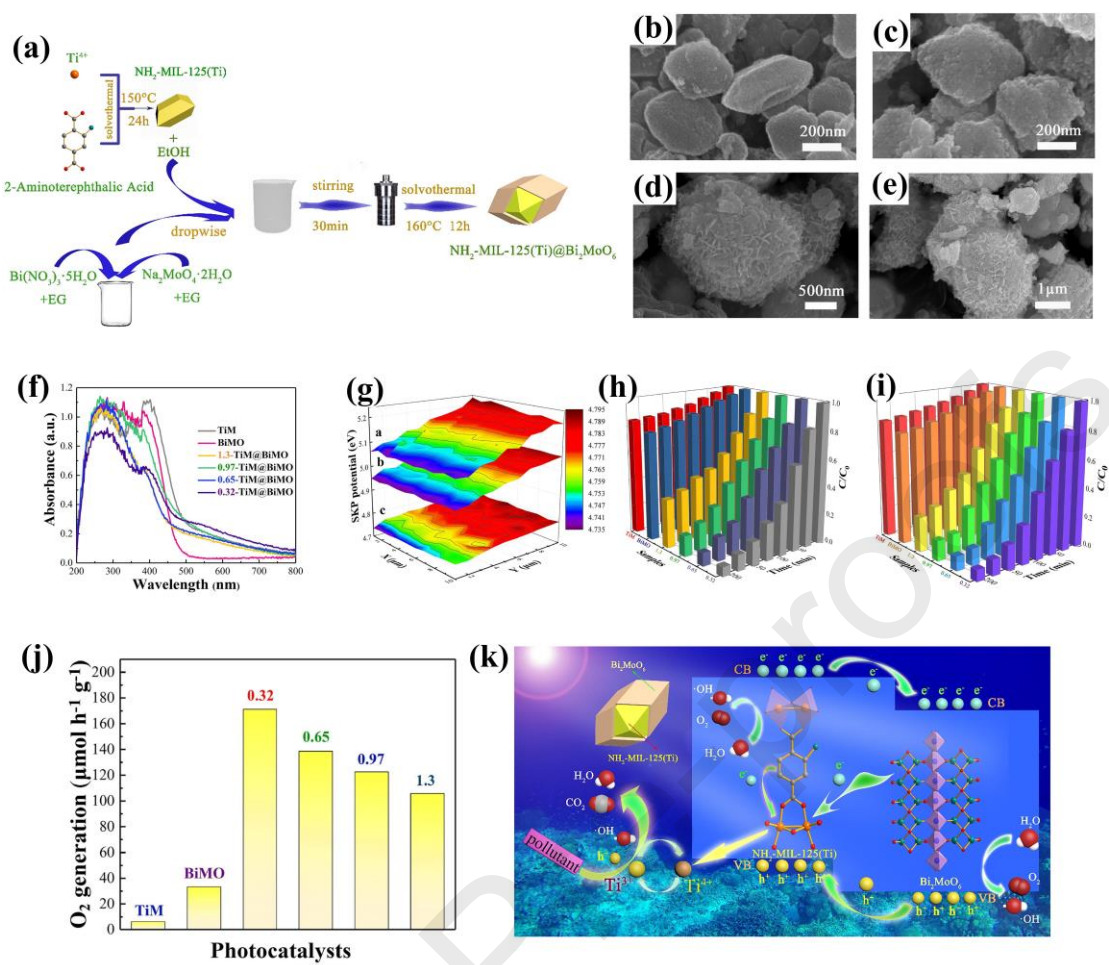


Figure 8

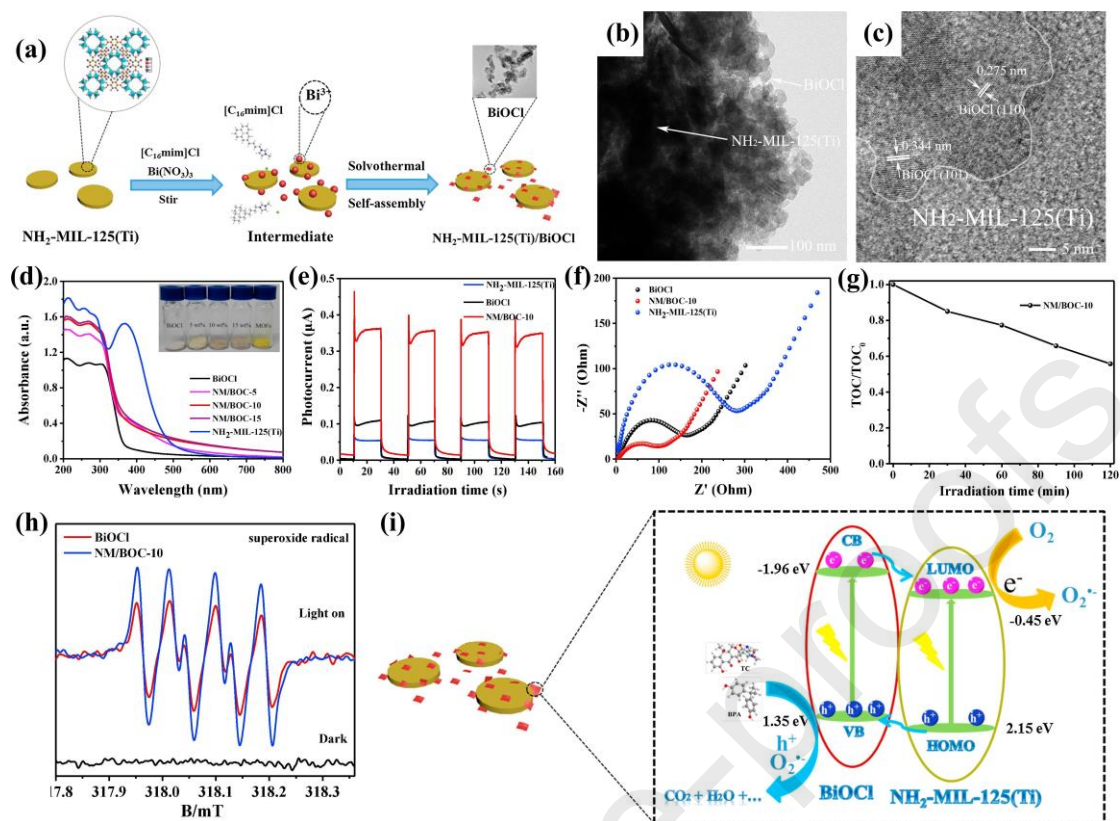


Figure 9

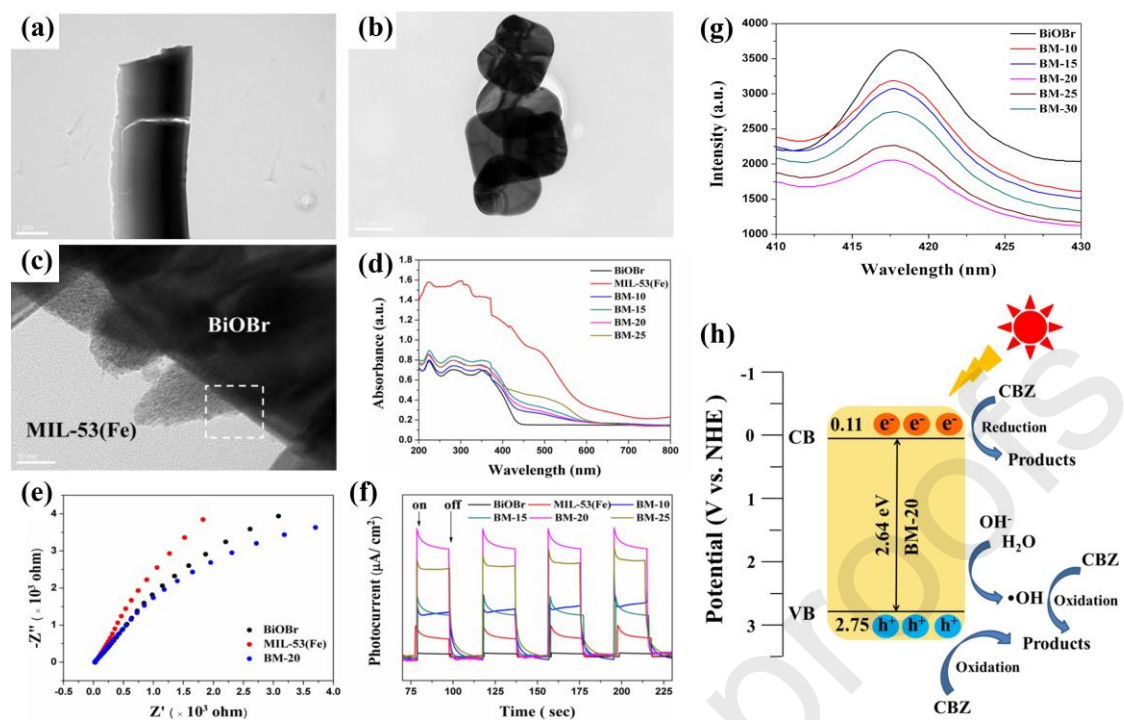


Figure 10

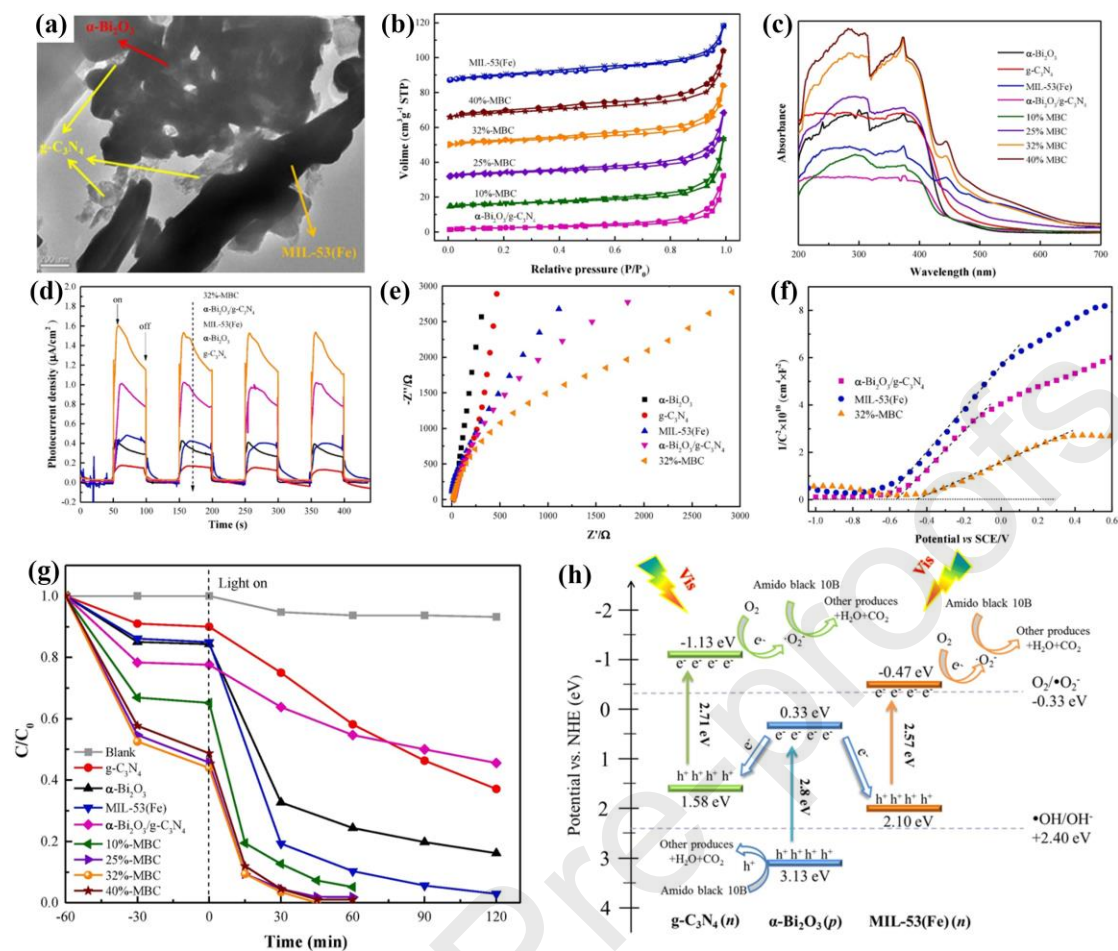


Figure 11

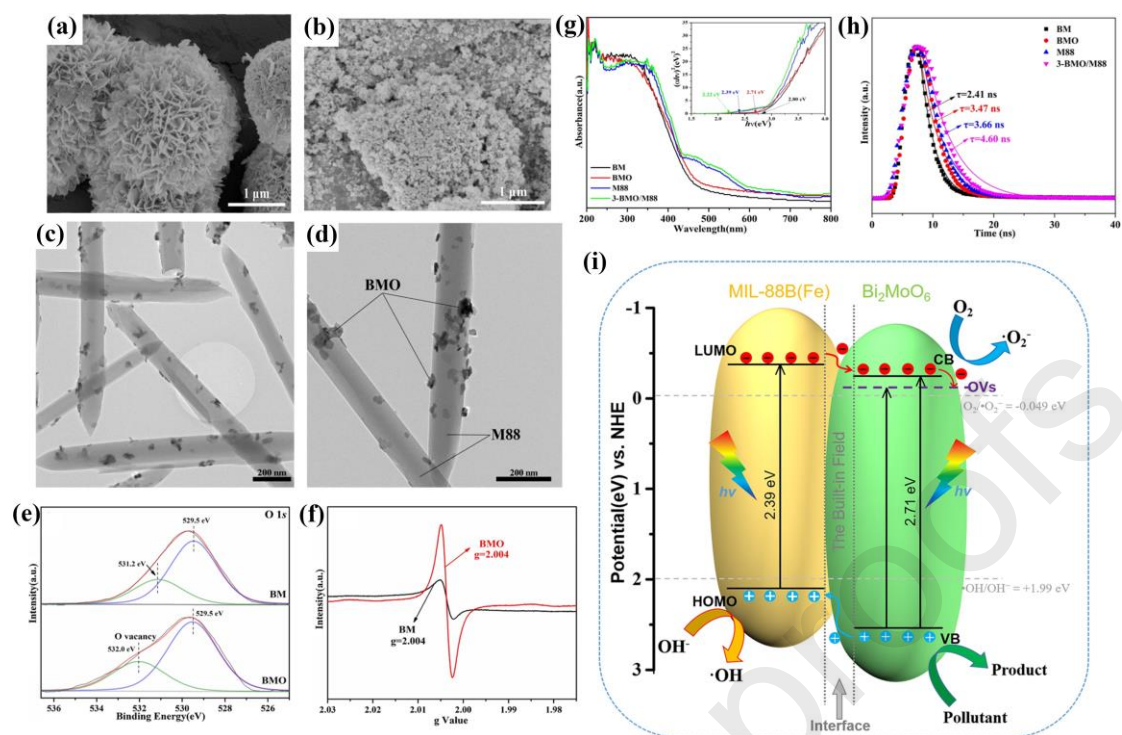


Figure 12

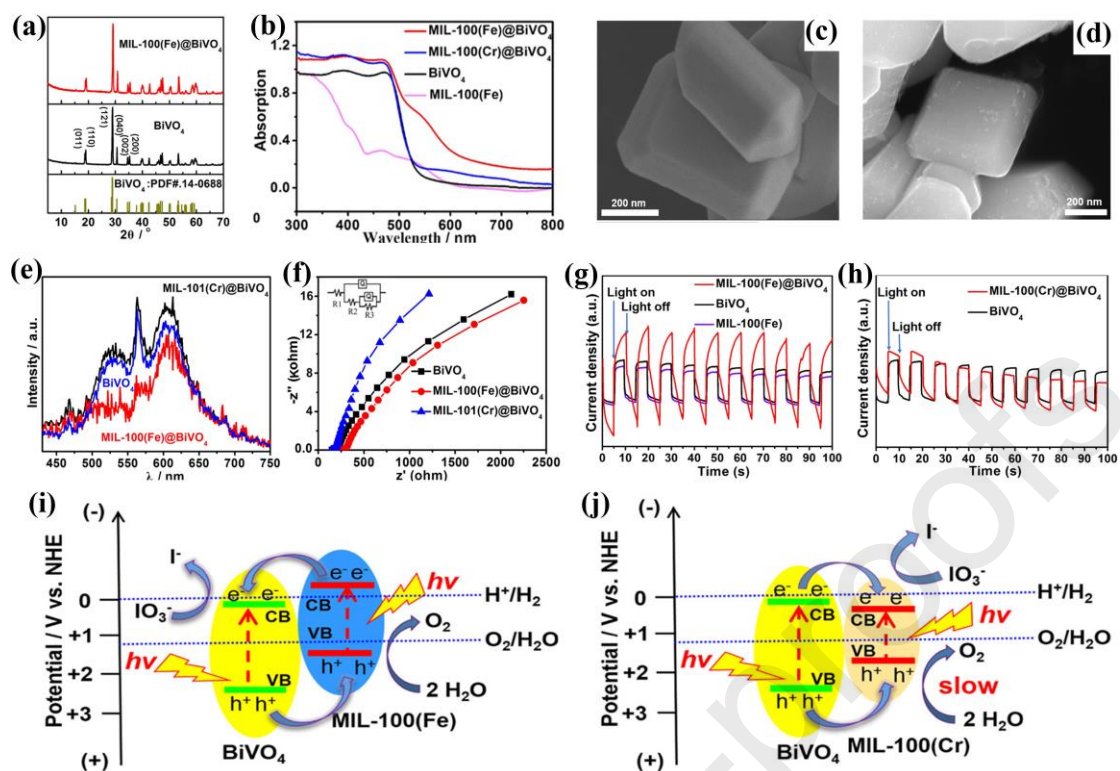


Figure 13

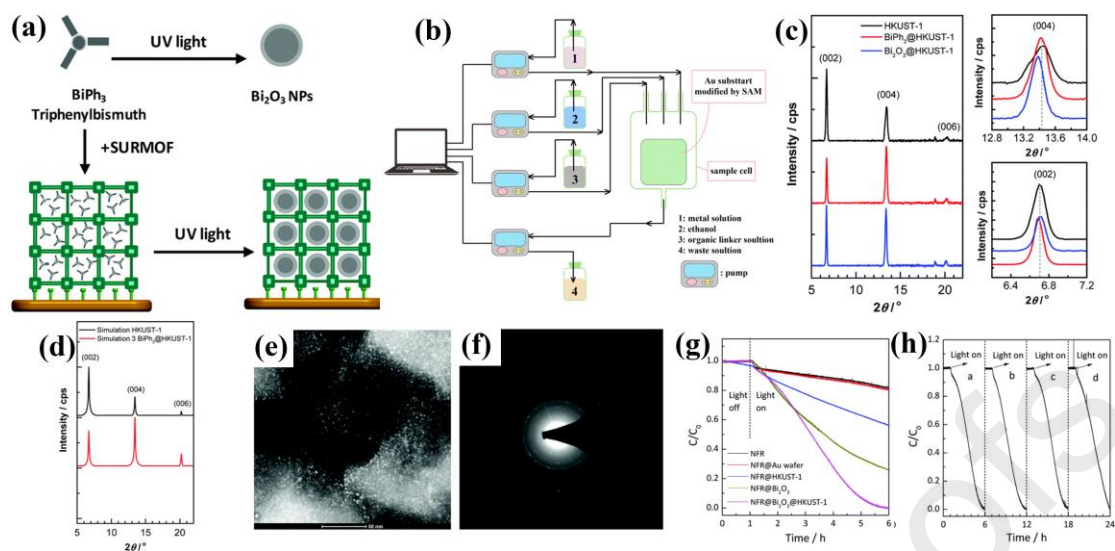


Figure 14

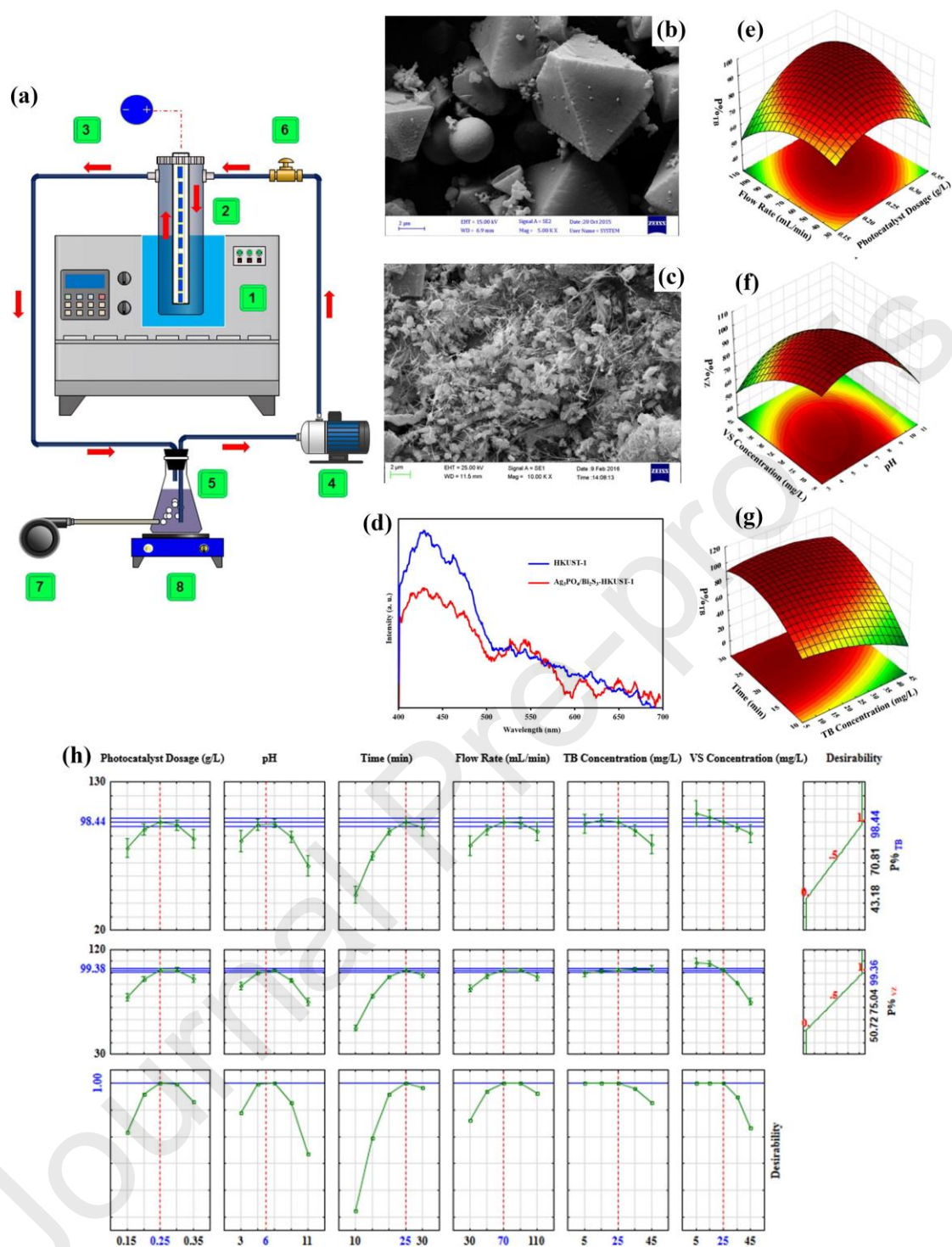


Figure 15

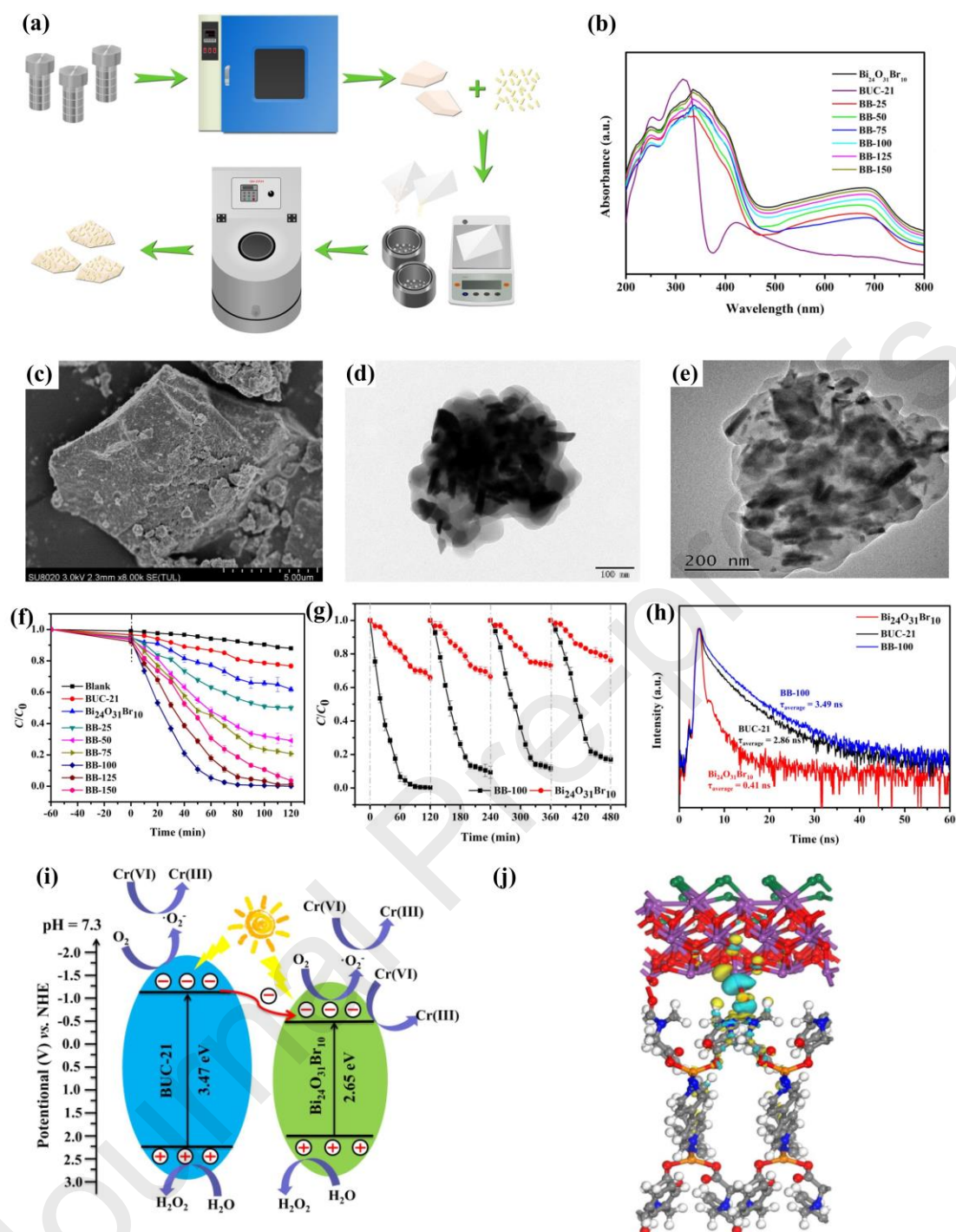


Figure 16

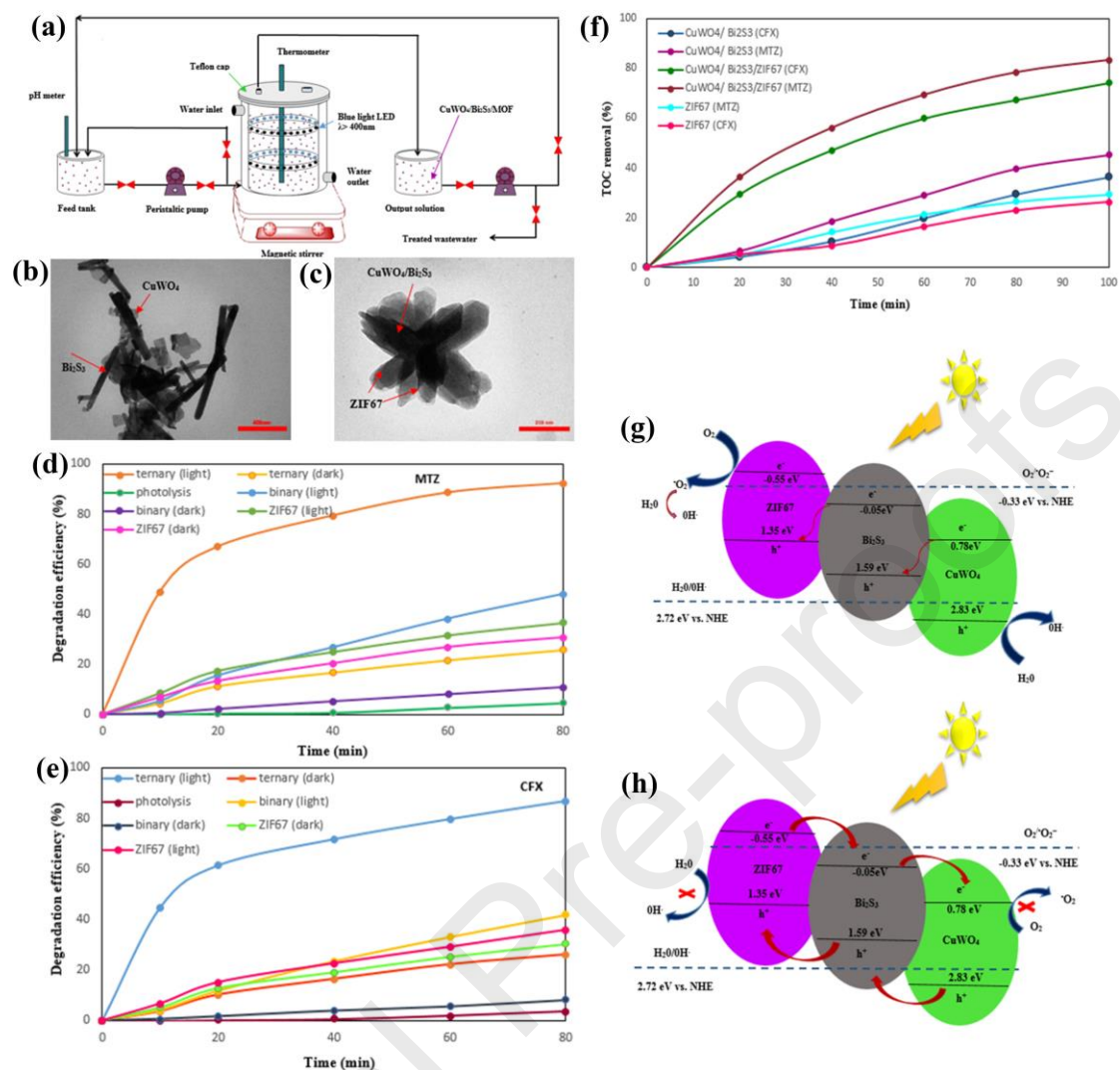
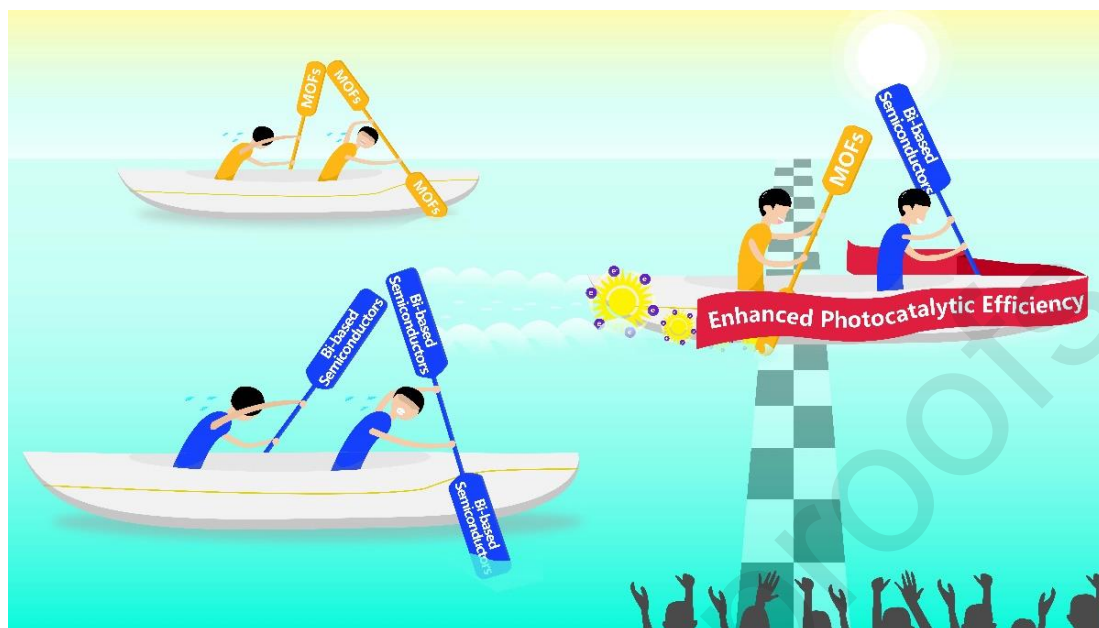


Figure 17

Graphical Abstract



Highlights

- MOF/Bi-based semiconductor composites for boosted photocatalysis was reviewed.
- The synthesis strategies of MOF/Bi-based semiconductor composites were summed up.
- Photocatalytic mechanisms of MOF/Bi-based semiconductor composites were described.
- The MOF/Bi-based semiconductor composites as photocatalysts were prospected.